

# Analyzing the Response of the Pelvis During Vertical Loading

---

A Thesis

Presented to  
the faculty of the School of Engineering and Applied Science  
University of Virginia

---

In partial fulfillment  
of the requirements for the degree

Master of Science

by

Preston Clark Greenhalgh

May 2019

## Approval Sheet

This Thesis  
is submitted in partial fulfillment of the requirements  
for the degree of

Master of Science

Author Signature:



This Thesis has been read and approved by the examining committee:

Advisor: Robert Salzar

Committee Member: Matthew Panzer

Committee Member: Thomas Hartka

Accepted for the School of Engineering and Applied Science:



Craig H. Benson, School of Engineering and Applied Science

May 2019

## Abstract

Underbody blasts (UBB) have become the most prevalent threats to soldiers in theater. These events typically occur from a bomb, mine, or improvised explosive device (IED), and are characterized by very high accelerations and short durations. During UBBs, life threatening injuries can occur when the pelvis is loaded from blast energy that is transmitted through the floor and into the seat of the vehicle. To better protect soldiers, a better understanding of how the pelvis is injured during UBBs is needed. Finite element models are commonly used to study injuries and can be used to test countermeasures to injury; however, modern pelvis finite element models lack high-rate material properties and are not suitable for simulating UBBs. The goal of this research is to find high-rate material properties of gluteal tissue and investigate the load path through the pelvis during vertical loading. To achieve this, the load response of eleven gluteal tissue specimens at high rates were captured through indentation of gluteal tissue specimens. A material model was created using an inverse finite element technique in which the tissue indentation of each specimen was simulated using specimen specific finite element models. The material properties were optimized through subsequent simulations until the error between the force response of the finite element models and the experimental tests was minimized. Then, a component pelvis finite element model was created to simulate previous pelvis UBB experimental tests. Boundary and input conditions were recreated, and the new tissue model was used for the gluteal tissue. Tools were then created to analyze the load path through the pelvis while being loaded vertically. It was found that in the loading rates tested, the rate of the impact did not affect the amount of load carried by the tissue or the load path through the pelvis. However, it was found that tissue thickness, tissue stiffness, and sacroiliac joint material properties all had significant effects on the effective load path through the pelvis. The insight from this thesis will assist ongoing research in understanding how the pelvis is injured during UBBs so that effective countermeasures can be created to protect soldiers in the battlefield.

# Contents

1	Introduction .....	6
1.1	Motivation .....	6
1.2	Hypothesis and Objectives.....	8
1.3	Expected Contributions.....	9
2	Background .....	11
2.1	Underbody Blasts .....	11
2.2	Anatomy of Pelvis in Sitting Posture.....	13
2.3	Pelvis Injuries .....	19
2.4	Soft Tissue Testing .....	22
2.5	Finite Element Pelvis Models.....	24
2.6	UBB Experimental Pelvis Tests.....	30
3	Material Testing .....	33
3.1	Introduction .....	33
3.2	Design of Experiment.....	33
3.3	Specimen Preparation .....	46
3.4	Drop Tower Testing .....	53
3.5	Results .....	58
3.6	Conclusion .....	64
4	Material Modeling .....	66
4.1	Introduction .....	66
4.2	Finite Element Model .....	67

4.3	Inverse Finite Element Method .....	77
4.4	Results .....	82
4.5	Conclusion .....	90
5	Application to Component Pelvis Finite Element Model .....	92
5.1	Introduction .....	92
5.2	Vertical Impact Pelvis Model .....	93
5.3	Results .....	110
5.4	Discussion .....	136
5.5	Conclusion .....	143
6	Conclusion .....	145
6.1	Summary .....	145
6.2	Contributions .....	146
6.3	Limitations and Future Work .....	150
7	References .....	153
8	Permissions .....	161
9	Appendix .....	162

# I Introduction

## I.1 Motivation

Since the onset of Operation Enduring Freedom in 2001 and of Operation Iraqi Freedom in 2003, there have been over 50,000 U.S. soldiers wounded and over 6,700 U.S. soldiers killed according to the Defense Casualty Analysis System (DCAS) [1], not including over 300,000 traumatic brain injuries reported by the Congressional Research [2]. Casualties from blasts, such as improvised explosive devices (IED), have steadily increased and have become the most prevalent threats to soldiers in theater [3–5]. Despite the use of mine-resistant ambush protected (MRAP) vehicles, numerous injuries still occur within these vehicles. The injury mechanisms for the complex injuries that occur during underbody blasts must be better understood in order to provide soldiers with more effective personal protective equipment, more protective MRAP vehicles, and other injury mitigation techniques [6].

Field medical data of mounted soldiers report that 8% of soldiers wounded in action and 51% of soldiers killed in action reported pelvis injuries [7]. The pelvis is a complex body region due to its irregular bony structure, and various types of pelvic injuries can occur during UBBs and other blunt trauma. Tissue is viscoelastic, and the rates at which it is impacted can play a large role on how the pelvis sustains injuries. This was seen in lateral testing of the pelvis by Salzar et al. [8]. When the pelvis was loaded quasi-statically, the pelvis tended to be injured at the pubic symphysis and when loaded at a higher rate, the sacroiliac joint or pubic ramus were generally injured.

For UBBs and other blunt trauma, the mechanism of injuries to the pelvis are not always understood. Understanding the load path through the pelvis may make the mechanisms of injury more clear. However, finding the load path through the pelvis is not straightforward, as most physical sensors are unable to fully capture load as it is transmitted through the pelvis. In the instance of Salzar et al., the load path was grossly

captured from two load cells (see Figure 1). If the load path through the pelvis is better understood, measures can be taken to prevent mechanisms of serious and deadly injuries to the pelvis.

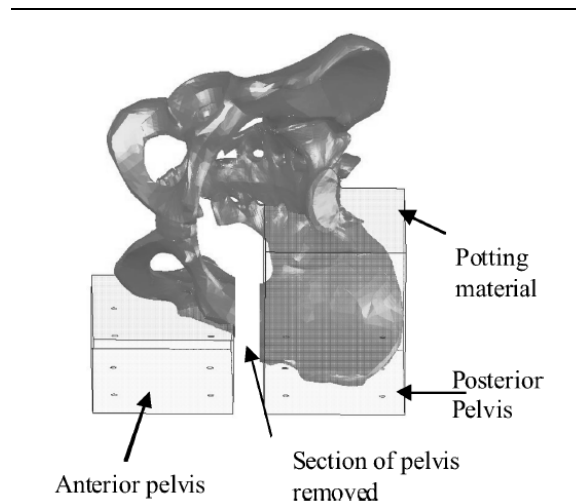


Figure 1. PMHS pelvis preparation from Salzar et al. [8]. Figure used with permission (see Chapter 8 for full permission).

---

There are many tools used to study injuries from UBBs, such as post mortem human subject (PMHS) testing, multibody modeling, and finite element (FE) modeling. PMHS testing is often the validation for multibody and FE models. Experiments based on PMHS testing will typically show types of injuries that occur from UBB loading scenarios as well as the probability that they will happen. However, cadaveric testing is expensive, lengthy, and has trouble measuring certain phenomena such as the load path through the pelvis. Once validated from experimental testing, human body FE models (HBM) are cheap, run relatively quickly, and can capture details such as the load path through the pelvis that the experimental tests cannot.

Current HBMs have become very complex and can be quite biofidelic in many scenarios. Many HBMs are used for automotive impacts and are therefore validated for those scenarios using human volunteer and cadaveric experiments. Like anthropometric test devices (ATD), HBMs do not always act biofidelically outside their intended use, and caution must be used when doing this. Often, parts of HBMs, such as pelvis

soft tissue properties, are not based on experimental data found in literature, but instead a surrogate is used that reasonably reflects the behavior of that part needed for its specific use. While not having precise material properties of pelvis tissue may not impact the desired results for certain uses, correct material properties for the analysis of UBBs and other high rate applications will likely play a much more critical role. There is a need for validated HBMs to analyze injuries that occur during UBBs. High-rate material properties of soft tissue in the pelvis is one area lacking in the literature that will help improve these models. Once HBMs are validated for analysis of UBBs, injury countermeasure experiments can be applied to these models to find techniques that will prevent injuries to soldiers that are subjected to underbody blasts.

## **1.2 Hypothesis and Objectives**

From previous observations, it was thought that at higher loading rates, soft tissue in the pelvis would stiffen up and could create different load paths through the pelvis and that these different load paths through the pelvis could create different injuries. It is hypothesized in this thesis that the load path through the pelvis is dependent on the loading rate.

The objective of this thesis was to test this hypothesis by creating tools to analyze the load path through the pelvis while being axially loaded at high rates. First, bulk gluteal tissue was dynamically tested in axial compression to obtain force-displacement data. Second, an inverse finite element method was used to form a constitutive model of the bulk gluteal tissue based on the experimental data. Third, a component pelvis finite element model—named the Vertical Impact Pelvis (VIP) model—was created by modifying the GHBMC whole-body automotive finite element model with updated geometry and tissue properties that simulates the UBB experimental pelvis cadaveric tests. Fourth, the load path of the pelvis was analyzed using the component pelvis FE model.



### 1.3 Expected Contributions

In accomplishing the objectives of this thesis to answer the hypothesis, there are several expected contributions to the field of injury biomechanics. First, there is a paucity in the literature for dynamic material properties for bulk gluteal tissue in compression. Dynamic material properties for other various muscles, skin, and fat exist; however, the literature has shown that material properties of different types of tissue vary. In addition, combining different models into a single bulk model would be complex. This research will provide experimental data for post-mortem human subject gluteal tissue as well as a material model that can be easily integrated into other models found in common commercial finite element software.

While testing gluteal tissue, this thesis will also provide a simple and inexpensive method that is effective in performing dynamic compression experiments on soft tissue. This method will be capable of creating a variable constant velocity input into the tissue, while also capable of capturing relaxation of the tissue through a quasi-step-hold of the tissue with little to no rebound of the indenter off the tissue. The simplicity of the design will allow for adaptation to similar lab equipment and similar tissue specimens.

During vertical loading, how load travels from the point of loading through the pelvis is not well understood. In answering the hypothesis of this thesis, a better understanding of this load path will be established. It is possible that different injuries to the pelvis when vertically loaded can be influenced by this load path through the pelvis. Understanding how the pelvis is injured is crucial to creating effective countermeasures to prevent injury. This thesis aims to increase the understanding of this load path through the pelvis.

To study the load path through the pelvis, a component pelvis finite element model will be created. There is a lack of validated finite element models for use in vertical, high-rate loading. Using existing finite elements outside of their intended use does not usually produce accurate results. This thesis will provide

the start of a pelvis model capable of being evaluated against post-mortem human subjects tested in high-rate vertical impacts. The future of this model beyond this thesis is expected to be capable of predicting injuries seen in soldiers subjected to underbody blasts, and be used to test countermeasures with the goal to prevent injuries to soldiers.

## 2 Background

### 2.1 Underbody Blasts

Underbody blasts (UBB) are high energy events characterized by very high accelerations and short duration loads on a vehicle. These events typically occur from a bomb, mine, or improvised explosive device (IED) [3]. The occupants receive a primarily vertical load by way of the explosion transmitting energy from the outside of the vehicle to the seated occupants (see Figure 2). Injuries from the vertical loading are considered tertiary, as WRAPs are specifically designed to shield occupants against the blast shock wave and ejected fragments—the source of primary and secondary injuries, respectively. The load an occupant would experience varies in each event, since the mechanism of blast, the type of vehicle, the seat type, and the restraint system vary.

Because much of the U.S. military vehicle data on UBBs are classified, there is no standard for UBB events, and studies are left to define the accelerations and time durations [9]. A report by the North Atlantic Treaty Organization (NATO) suggested that the pelvis is loaded around 10 ms after detonation, while a seat mounted to the roof or side of the vehicle will tend to reach peak accelerations around 15–20 ms after denotation and is less severe than a seat mounted to the floor [10]. Ramasamy et al. reported that the floors of these vehicles reach 7–30 m/s in 6–10 ms, indicating accelerations in excess of 500 g with durations of 2–3 ms [3].



Figure 2. ATD shown experiencing an underbody blast inside an MRAP [11].

A seated soldier will have two primary load paths during an UBB event: into the feet and up the legs and into the pelvis and up the spine. Axial, blast level loading of the leg [12–20] and the heel pad [21] have been studied, but there is less in the literature on high-rate, axial loading of the seated pelvis.

Bailey et al. replicated UBB loading conditions in a controlled laboratory setting using whole post mortem human surrogates (PMHS) [22]. The pelvis was instrumented with strain gauges and a six degree-of-freedom accelerometer array rigidly mounted to the sacrum, but no load cells were used to analyze the transferring of load to the pelvis. Danelson et al. similarly tested 18 whole PMHS in vertical UBB loading with rigorous instrumentation, but lacked load cells on the seat pan [23]. Yoganandan et al. also tested whole PMHS in vertical loading in order to analyze the loading conditions and how they relate to injuries [24]. The pelvis response was measured using a tri-axial accelerometer block rigidly mounted to the mid-sacral plate and load cells attached the seat pan; but this data alone is insufficient to capture how load is distributed through the pelvis.

While axial, blast level loading conditions are scarce in the literature, there is a wealth of literature on loading of the pelvis in automotive frontal [25–27] and side impacts [8,28–34]. In addition, Salzar et al.

reported injuries from axial loading simulating military ejection seats, but all injuries reported were superior to the pelvis, and the rate of loading was very low relative to UBB conditions [35].

Despite all this existing knowledge, it is clear from the literature that a significant correlation exists between injuries and the direction and rate of loading. Therefore, axial, high-rate loading of the pelvis must be employed in testing to better understand the loading of the pelvis in UBB settings.

## **2.2 Anatomy of Pelvis in Sitting Posture**

The pelvis constitutes the part of the body between the abdomen and the thighs. Its irregular bone structure protects and supports gastrointestinal and reproductive organs, supports the weight of the upper body, and allows motion by serving as the anchor for dozens of muscles and tendons. The pelvis is made up of three bones: two coxal bones (hip bone) and the sacrum (see Figure 52). The coxal bone itself is composed of three main parts: the ilium, ischium, and pubis. The ilium is a large wing-like bone that connects to the sacrum through the sacroiliac joint, a synovial joint reinforced by strong ligaments that helps absorb shock and transfer weight between the upper and lower body. The ilium joins the ischium at the acetabulum, the surface that meets with the femoral head. On the posterior side of the ischium is the ischial tuberosity, which supports weight of the body while sitting. Also joining at the acetabulum is the pubic bone, which also connects to the ischium through the inferior ramus. The left and right pubic bones are connected together by the pubic symphysis, a cartilaginous joint that is supported by encapsulating ligaments. While the pubic symphysis resists tensile, shearing, and compressive forces, it also allows a small amount of movement, more notably in the female pelvis during pregnancy.

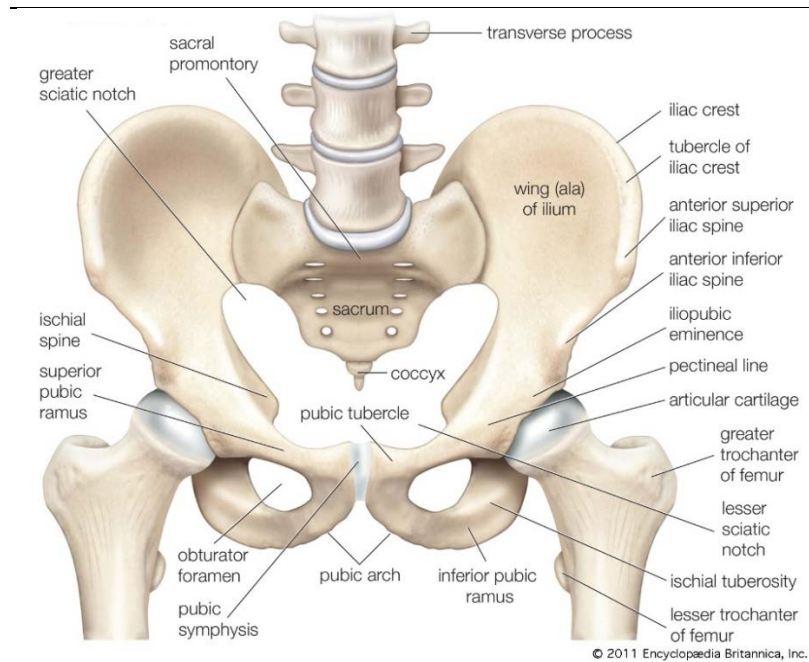


Figure 3. Anatomy of the bony pelvis [36].

The pelvis serves as attachment points for several groups of muscles, serving as an anchor to allow all sorts of motion to the upper and lower parts of the body (see Figure 52). While not anchored at the pelvis, the psoas major runs from L1 of the lumbar spine down the anterior surface of the ilium and joins with the iliacus on the femur to provide flexion between the upper body and legs. The piriformis, pectineus, gracilis, adductor longus, and adductor magnus originate at the pubic bone and insert either at the femur or tibia and provide adduction (moving together) of the thighs. Extension, external and internal rotation, and abduction of the hip joint are possible through the gluteal muscles. The gluteal muscles—gluteal maximus, medius, and minimus—are stacked on top of each other with the minimus being stacked closest to the posterior surface of the ilium. The piriformis, superior and inferior gemelli, externus and internus obturators, and quadratus femoris originate around the acetabulum and insert on the femur and allow external, lateral rotation of the femur about the hip joint. Other muscles such as the hamstring muscles, the sartorius, and the rectus femoris, are typically not considered in the pelvic muscle group, but still attach at the pelvis and provide various motion of the thigh and knee joint.

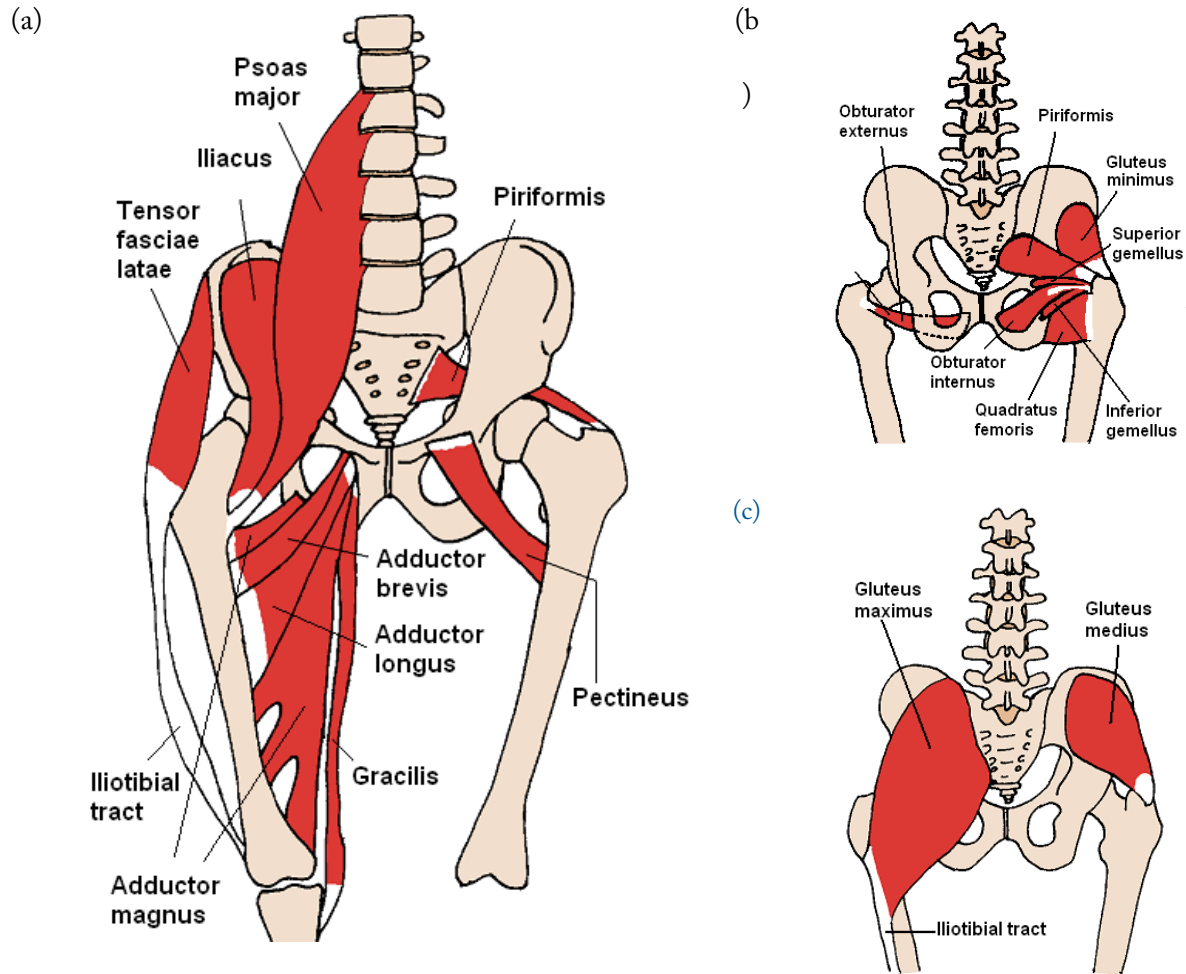


Figure 4. Muscles of the pelvis seen from the anterior (a) and posterior (b, c) [37].

Shape, length, and moment arm of muscles change with hip extension/flexion, hip adduction/abduction, and hip internal/external rotation (see Figure 52). The paths of muscles are complex since they are constrained by interactions with boundaries of other muscles, bone, and ligaments [38]. Hence, the soft tissue distribution of the musculoskeletal pelvis significantly changes in different postures (e.g. sitting, supine, etc.).

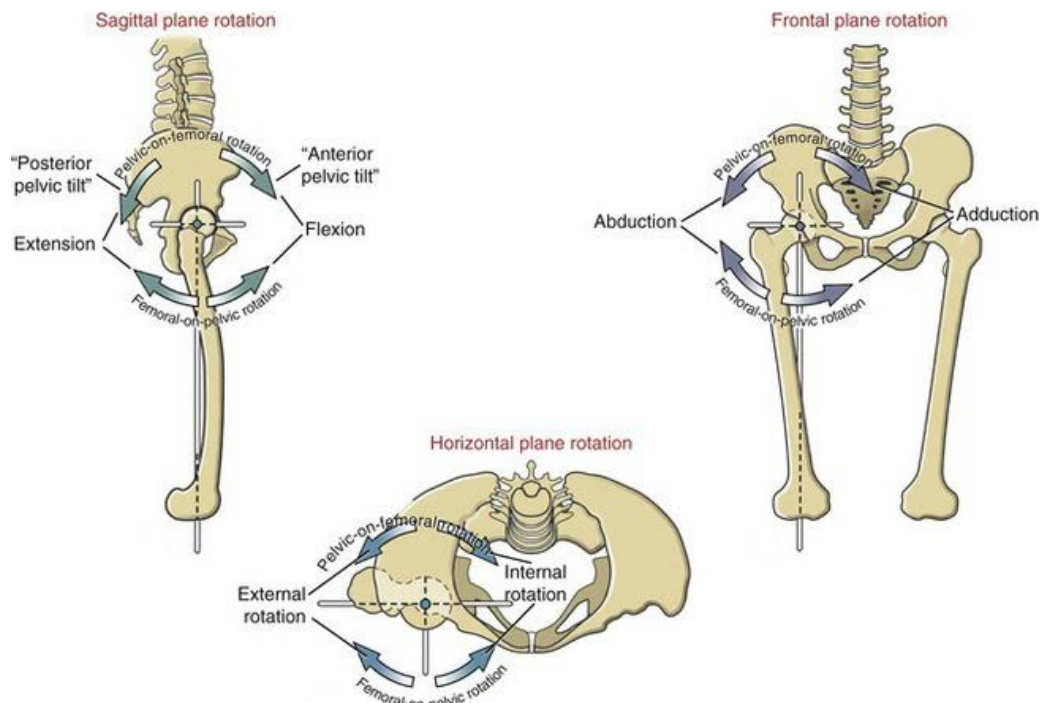


Figure 5. Motions of the pelvis in the sagittal, horizontal, and frontal planes. [39]

While sitting, large deformations of soft tissue occurs and muscles change position around the bony pelvis. In an upright sitting position, the ischial tuberosities support most of the weight of the pelvis. When more reclined, the coccyx supports more of the weight distribution. Physiological differences, posture, leg positioning, and the type of chair/cushion all influence the weight distribution through the body. There is no widely accepted standard for sitting posture, so body weight distributions vary considerably in the literature. Using an array of 64 special strain gauge resistive transducer plates, Drummond et al. reported that when sitting with free-hanging feet, the right and left ischia support an average of 17% and 18% body weight, respectively, with the sacrum supporting 5% [40] based on 15 healthy patients. Chow and Odell assumed that each buttock supported 38.5% body weight [41], and Wagnac et al. reported through an experimental weighing device that 69% of body weight was supported by the buttock with the feet supported [42].



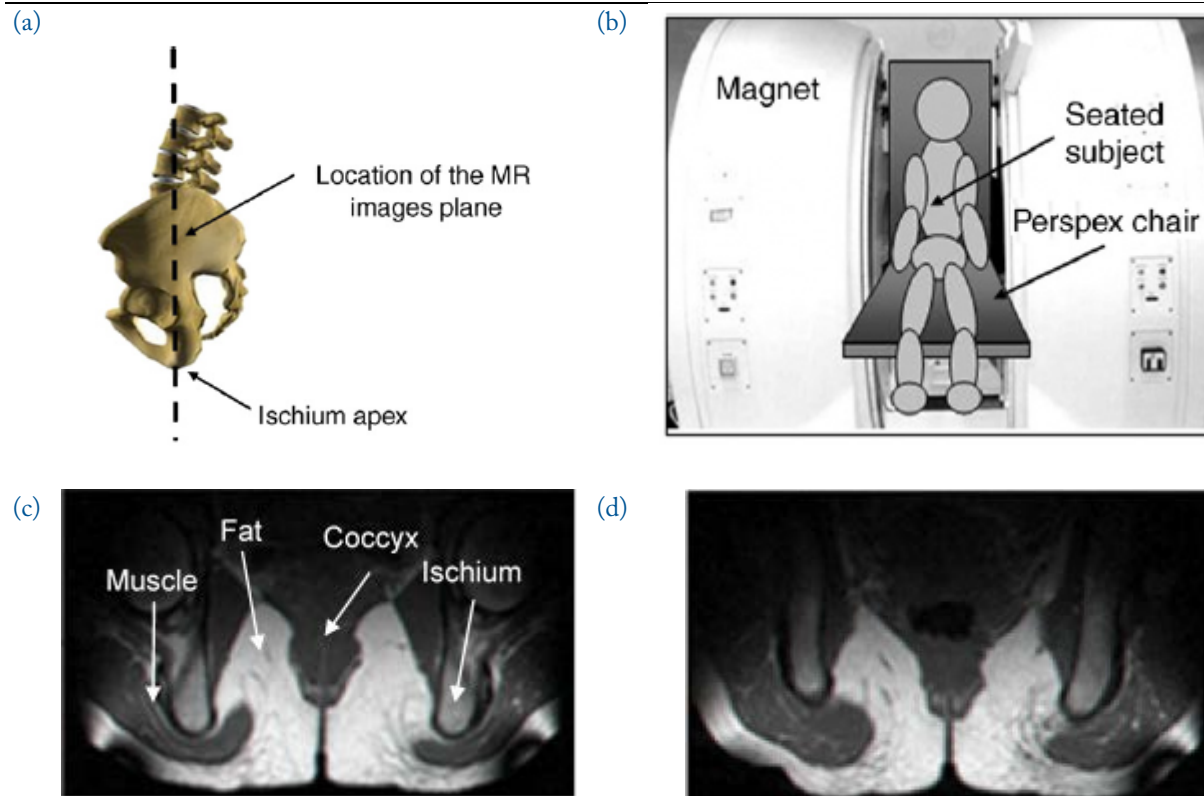


Figure 6. Cross-sectional images from a sagittal plane centered on the ischium apex (a) of a live subject sitting in a “double donut” open-MR system (b). The gluteus maximus envelops the ischial apex during both weight-bearing (c) and non-weight-bearing (d) sitting postures [43]. Figures used with permission (see Chapter 8 for full permission).

Underneath the ischia are layers of adipose tissue and muscle, specifically the gluteus maximus. The gluteus maximus has a broad attachment at the posterior gluteal line of the ilium, the posterior and lateral surface of the sacral crest, and the side of the coccyx. Its thick, tendinous lamina envelops the ischial tuberosity and passes across the greater trochanter, then inserts into the iliotibial band of the fascia lata. While standing or in a supine/prone position, the gluteus maximus envelops the ischial tuberosity [43–45] followed by fat and then skin (see Figure 6). However, while sitting, due to hip-flexion and compression of soft tissue from body weight, the composition and thickness of soft tissue underneath the ischial tuberosity changes.

Through the use of magnetic resonance (MR) imaging, many have confirmed that the gluteus maximus still envelops the ischial tuberosity in a 90° hip-flexion unloaded state [43–49]. When in a loaded sitting

posture, all reported compression of both the gluteus maximus and adipose tissue, but many simplified their pelvis models from the MR images into 2-D slices which obscured the 3-D deformation of the soft tissues. Sonenblum et al., Makhsous et al., and Al-Dirini et al. all found that the gluteus maximus under deformation slides away from the ischium in the anterior-posterior direction and laterally, in addition to vertical deformation, showing that the deformation of the gluteus maximus is a combination of deformation and distortion [45–47,49]. Cadaver and MR recordings have shown that when flexed, muscle (mostly the gluteal muscle) moves away from bony prominences laterally. Sonenblum et al. adds that there is also an anterior displacement of the hamstrings during sitting. Al-Dirini suggests that this increases both muscle and fat tissue thicknesses in other locations further from the ischium, such as below the lesser trochanter or the femoral head.

When compared to supine and 45° hip-flexion, 90° hip-flexion had a significantly thinner covering of soft tissue underneath the ischial tuberosities [45]. Sonenblum and Al-Dirini both emphasized that there is population variability, showing that some patients showed little to no gluteal compression, and others having their gluteus maximus completely slide off the ischium during compressive sitting. This aforementioned variability includes ischial tuberosity radius of curvature, gluteus maximus thickness, adipose tissue, ischium geometry, and connective tissue [47,50,51]. Much of this variability can affect the stresses and strains seen by gluteal soft tissue. For example, Linder-Ganz et al. found that the patients with the sharpest (smallest radii) ischial tuberosities also had the highest stresses and strains [43], and Sopher et al. found that internal loading was greater in higher and lower BMI groups [50].

Different population subgroups tend to emphasize variability. Paraplegics confined to wheelchairs tend to have significantly less gluteal muscle, with one study finding that healthy individuals can have about two times thicker gluteus muscle than paraplegics [52]. Linder-Ganz also found that fat tissue thicknesses were

statistically indistinguishable between the two groups. Right and left ischial tuberosity radii of curvature were 1.7- and 1.6-fold higher in the healthy group, suggesting major bone structure due to chronic sitting. Obese patients were shown to have the highest deformation [49] and low and high BMI groups have been shown to have higher internal loading [50]. Dunk and Callaghan reported that males and females may be exposed to different loading patterns during prolonged sitting [53].

Because of the movement of muscles in different postures, postures have an effect on the loading of soft tissues [54]. During loaded sitting, the muscles underneath the ischial tuberosities strain more than the adipose tissue, with fat strains reported between 11.8 and 34.8% and gluteus maximus between 38.1 and 75.3% [43,45–49]. The variability in strains can be explained through different experimental setups (e.g. seat cushions, strain calculation methods, data collection methods) and different populations employed (e.g. age, sex, BMI). Leaning to one side (lateral tilt) has also shown to significantly increase stress and strain underneath the ischial tuberosity [48].

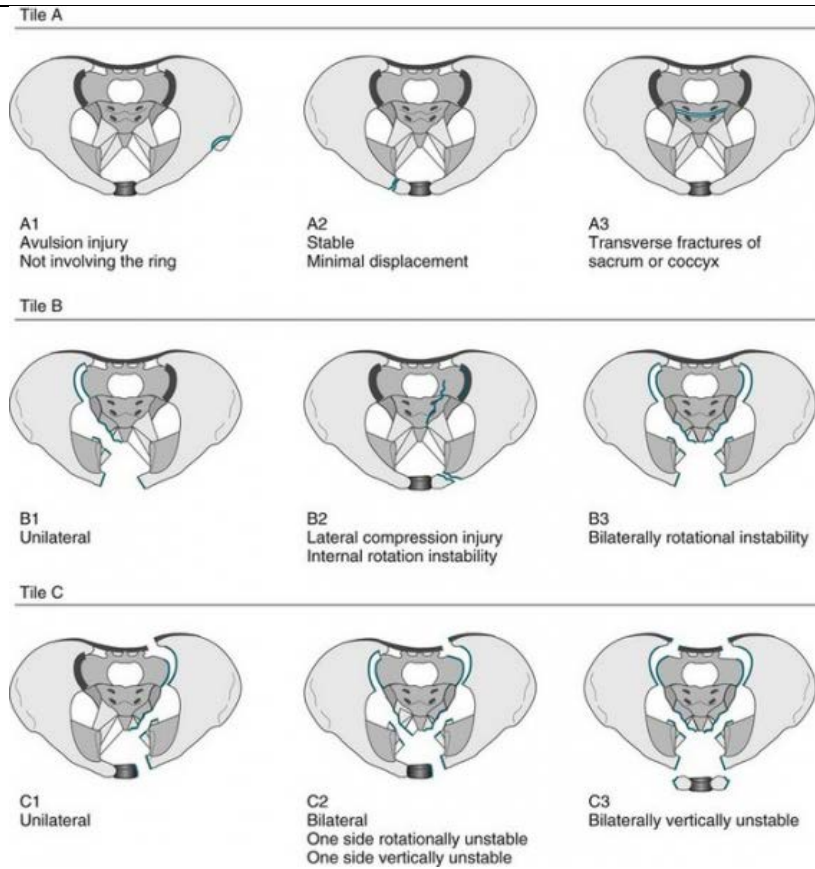
## **2.3 Pelvis Injuries**

While IED incidents cause numerous types of injuries from every body region, open blast fractures of the pelvis are considered to be the most severe [55,56]. While MRAP vehicles are designed to prevent open blast events, field medical data of mounted soldiers report that 8% of soldiers wounded in action and 51% of soldiers killed in action reported pelvis injuries [7]. Injuries to the pelvis have immediate as well as long term complications. Due to high concentration of large arteries, including the femoral arteries, pelvic injuries risk causing hemorrhaging and hypovolemic shock. Severe pelvic injuries can also limit mobility, which in turn can jeopardize a soldier's ability to escape the vehicle following an UBB event. Infection, septic shock, and all the complications mentioned previously can increase morbidity and increase recovery time for soldiers.

Bailey et al. reported a myriad of direct pelvis injuries due to blunt trauma, mostly from blasts [56]. These include Tile A (stable fracture pattern), Tile B (partially stable, rotationally unstable), and Tile C (rotationally and vertically unstable). In the Young and Burgess injury classification, Bailey reported injuries as anterior posterior compression, lateral compression, vertical shear, and combined mechanisms.

Being one of the two major load paths during UBB events, the pelvis also transmits load axially up the spine and body. It was found that of soldiers who were wounded in action (WIA) with a pelvis injury, 57% also sustained a lumbar spine injury, and 57% also sustained a torso injury [7]. Further, of those soldiers who sustained pelvis injuries and were killed in action (KIA), 51% of them also sustained a lumbar spine injury, and 98% of them also sustained a torso injury. J. Bailey et al. also found head injuries, cardiopulmonary injuries, and solid organ injury to be associated with blunt pelvis injuries [56].

(a)



(b)

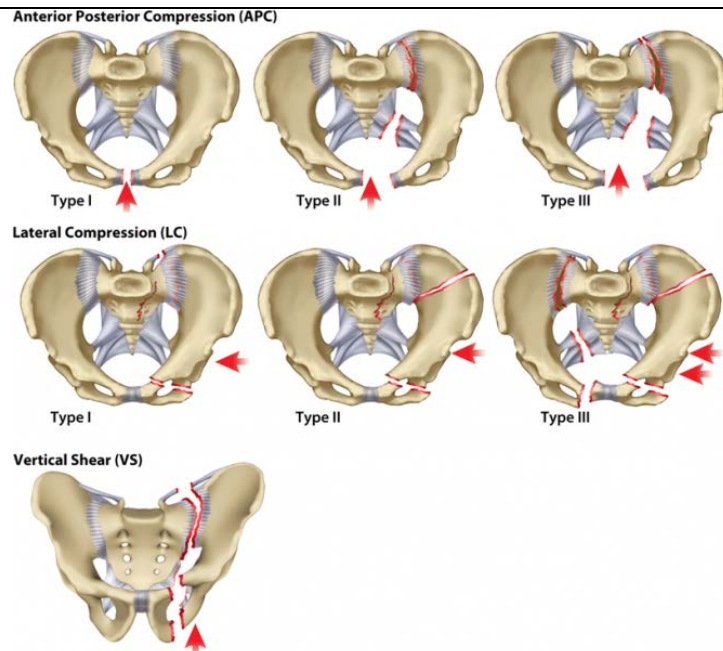


Figure 7. Depictions of the (a) Tile pelvic injury classification system [57], and the (b) Young and Burgess injury classification system [58]. Figures used with permission (see Chapter 8 for full permission).

## 2.4 Soft Tissue Testing

While material testing of soft tissue in general is common in the literature, dynamic testing and characterization of human bulk gluteal tissue in compression is rarely found. Soft tissues are more commonly tested individually rather than in bulk, are tested more often in animals than human, and are more commonly tested at low rates, especially if in vivo. Varying muscles are known to have significantly different mechanical properties, and different sections of adipose tissue have also shown to be different [59–61]. Therefore, material properties of human gluteal muscle and corresponding adipose tissue and skin should be used for highest accuracy in finite element modeling and other modeling techniques. In addition, soft tissue are well characterized to be viscoelastic [62,63] and the use of a specific soft tissue model should match the rates for which they were tested.

Much of the literature on gluteal soft tissue originates from the study of deep tissue injury (DTI). Finite element methods are commonly utilized in these studies (more on DTI and FE models in Section 2.5) as the authors seek out locations of peak stresses and strains and how it relates to DTI; however, these studies are mostly qualitative rather than quantitative, and lack constitutive models of the tissue itself. Some have sought out material properties of gluteal tissue through physical material testing, albeit at low rates. Since DTI develops in a time frame of minutes to hours [64,65], this is suitable for the authors of DTI research, but it is less useful for use in dynamic loading environments.



Figure 8. Example of in vivo testing of gluteal tissue through indentation [66]. Figure used with permission (see Chapter 8 for full permission).

---

Todd and Thacker used magnetic resonance (MR) imaging to create a bilateral symmetric 3-D model of the body in a supine position. They found soft tissue material properties of their two subjects (one male and one female) through indentation tests. The tissue was modeled as linear, isotropic, and time independent [67]. In addition, Then et al. created Ogden models of skin/fat and muscle based on in vivo indentation tests at a rate of 10 mm/s on a single patient [66]. The patient was positioned in an open MRI setup, and the indenter and buttock region was captured. An inverse finite element (iFE) approach was used to create the constitutive equation by varying the material constants in the Ogden model until it matched the experimental results, using an optimization routine to minimize error. Others have tested gluteal tissue properties in animals for use in human FE models [43,44,64,65].

Methods such as ultrasound [68], MR elastography [69], and pressure mat analysis coupled with FE modeling [51] have also been used to obtain material properties of various soft tissues. Compression testing for other tissues such as breast tissue [70] and heel pad [21,71] have also been performed to create constitutive models.

## 2.5 Finite Element Pelvis Models

Finite element models of the pelvis—either part of a full body model or component—have been extremely valuable in various medical and engineering fields. In the field of DTI, FE models are used frequently to calculate stresses and strains in the pelvic region. A deep tissue injury is a form of pressure ulcer that usually forms in subcutaneous tissue before spreading to external tissues. DTI is especially dangerous because it usually occurs in wheelchair-ridden individuals who often have less feeling in the buttock region and do not always feel early stages of DTI until it has already started to spread to external tissues. Sores typically happen at bony interfaces, with internal tissues near bony structures often experiencing higher stress than at surface [41,43,72]. Because of this, non-invasive test procedures cannot determine internal stresses and strains, but the use of FE models has overcome this. The use of FE models for DTI has spurred a lot of research on the buttock-seat interaction as well as a better anatomical knowledge of the buttock region (see Section 1.3).

Early pelvis FE models for DTI research have been around since the 1970s, utilizing simplified geometry and material properties [41,72]. More sophisticated models started using MR imaging to gain more accurate geometry [43,67], and pressure plates to get boundary conditions with a seat [73]. Material properties used in these models progressed from simple approximations based on gels to using animal tissue properties [44,74]. These FE models were often used to analyze stress and strain levels of loaded tissue. Linder-Ganz et al. found that compression strains in deep muscle under the ischial tuberosity were large (~74%) and almost three-fold larger than the body-seat interaction (~25% in fat/skin) [43]. Stresses were also found to be ~1.7 times greater under the IT than the interface pressure. The subject with the sharpest IT (smallest radii) had highest strains and stresses. Linder-Ganz et al. also later expounded on this research to study variation in muscle stresses and strains in paraplegics [52] and also to create a real-time FE model for individuals with spinal cord injury [75]. Outside of DTI, other models of the pelvis have been created



for clinical research, such as the work done by Anderson et al. which developed as a subject-specific pelvis model with emphasis on bone properties to assess strain predictions in the bone [76].

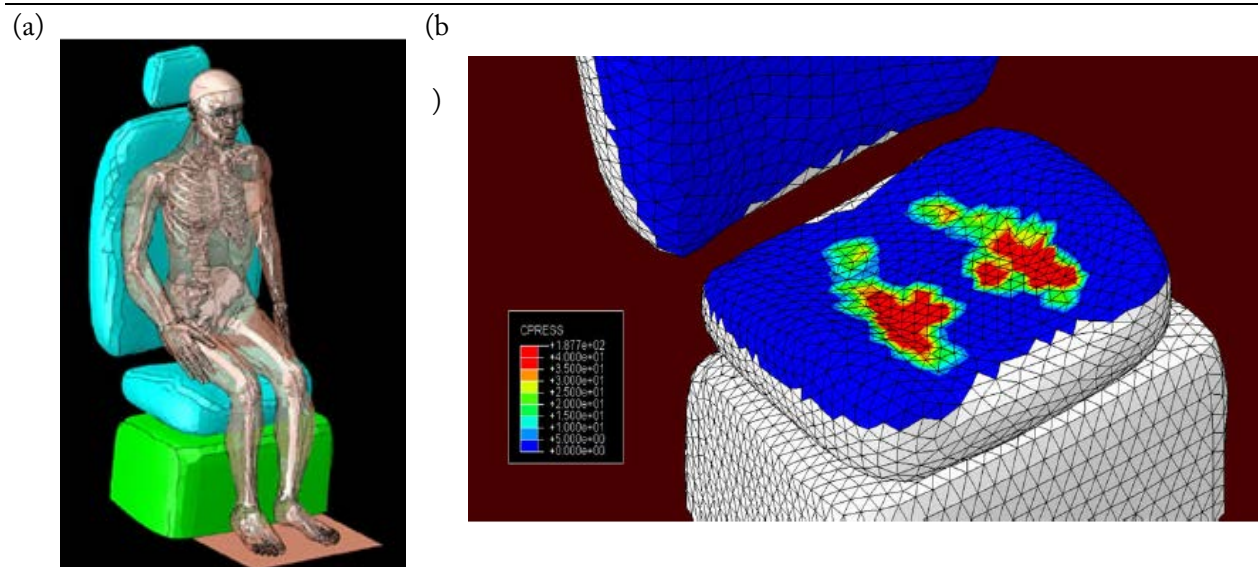


Figure 9. Grujicic et al. used an FE model to model the interaction between the pelvis and an automotive seat [77].

Figures used with permission (see Chapter 8 for full permission).

---

FE models of the pelvis have also been developed for the purpose of automobile seating ergonomics. The process of creating comfortable automobile seats are typically based on empiricism, past knowledge, and prototyping [77]. Many FE models have been created in an attempt to bypass the expensive and time-consuming process of current seat prototyping by associating customer comfort to stresses and strains found in the FE models, with the notion that lower stresses and strains found in the buttocks will yield more comfortable seats. These models are often very similar to those for DTI research since they are both interested in stresses and strains in the buttocks, but with an emphasis on comfort in automobile seats.

Finite element models are frequently used in the automobile safety industry in lieu of cadaveric or ATD testing. For pelvis injuries in automotive impacts, side impacts are typically of the most interest, and most FE models are geared towards these impacts. Many component pelvis FE models have been developed to

isolate the pelvis for automotive side impacts. Besnault et al. created a bony pelvis model using geometry from morphometric studies and assumed elastic isotropic material properties [78]. Dawson et al. created a similar model, but instead gained geometry and material properties from CT images and validated tests from a suite of strain gauges from cadaveric experiments [79]. Later, Ko et al. created a hybrid model of the bony pelvis, combining material properties from CT, the coxal bone from the H-Model, and the sacrum from the THUMS model [80].

The pelvis has also been modeled as part of many whole body models. One of the earliest full body models was created by Huang et al., studying thoracic injury [81]. Lizée et al. also created an early model in which the pelvis was validated using data from lateral loading of denuded cadaveric pelvises [82]. More advanced models, such as one presented by Ruan et al. [83], used the Visible Human Project [84] and other methods to create more realistic geometry. More modern models now exist such as the H-Model [85,86], Global Human Body Models Consortium (GHBMC) [27,87], PIPER [88], Human Models for Safety (HUMOS) [89], HUMOS2 [90], Total Human Model for Safety (THUMS) [91], and the CHARM model [92]. These models have varying levels of sophistication, applications, and validation. Some of these models are specifically for certain population subgroups. For example, the CHARM-70F models 70-year-old females, and the CHARM-10 models 10-year-old children.



---

Figure 10. GHBM v4.4 50th percentile male detailed model.

---

The GHBM is funded and developed by a number of commercial automotive companies, government agencies, and academic institutions to create biofidelic human body models for automotive crash simulations. The GHBM has a number of models including male and female seated occupants, pedestrians, and a child model. The pelvis portion of the GHBM has several data sets that were used in validation of its biofidelity. The cortical bone in the pelvis was taken from the work done by Anderson et al., briefly mentioned previously [76]. Pubic symphysis material properties were taken from Dakin et al. who compared pubic symphysis stiffness in side-impacted and un-impacted cadavers measured by tension, compression, and bending material tests of the pubic symphysis [93]. Lateral compression tests from Beason et al., who studied the effects of BMD on fracture load of the pelvis in side impacts [94]. Lastly, two sets of pelvic lateral impact tests performed by Guillemot et al., in early research studying the behavior and

tolerance of the pelvis in lateral loading. While advanced, the GHBMC model was designed as an automotive impact model and lacks any axial-loading validation and high-rate material properties.

Table 1. List of pelvis FE models

Reference	Purpose	Model Name
Chow, Odell, 1978 [41]	Deep tissue injury	
Dabnichki, et al., 1994 [72]	Deep tissue injury	
Todd, Thacker, 1994 [67]	Deep tissue injury	
Brosh, Arcan, 2000 [73]	Deep tissue injury	
Gefen et al., 2005 [44]	Deep tissue injury	
Oomens, et al., 2003 [74]	Deep tissue injury	
Linder-Ganz et al., 2007 [43]	Deep tissue injury	
Linder-Ganz et al., 2008 [52]	Deep tissue injury	
Linder-Ganz et al., 2009 [75]	Deep tissue injury	
Anderson et al., 2005 [76]	Bone strain, general use	
Grujicic et al., 2009 [77]	Seat ergonomics	
Besnault et al., 1998 [78]	Automotive	
Dawson et al., 1999 [79]	Automotive	
Ko et al., 2006 [86]	Automotive	JK-Coxal
Huang et al., 1994 [81]	Automotive	
Lizee et al., 1998 [82]	Automotive	
Ruan et al., 2005 [83]	Automotive	
ESI Group, [85] Konosu, 2003 [86]	Automotive	H-Model
Untaroiu et al., 2012 [27], GHBMCM [87]	Automotive	GHBMCM
PIPER [88]	Automotive	PIPER
Robin, 2001 [89]	Automotive	HUMOS
Vezin, Verriest 2005, [90]	Automotive	HUMOS2
THUMS [91]	Automotive	THUMS
Wayne State University [92]	Automotive	CHARM

## 2.6 UBB Experimental Pelvis Tests

To capture the response of the pelvis during UBB events requires experimental and material testing, and validation. Previously at the University of Virginia (UVA) Center for Applied Biomechanics (CAB), thirteen post-mortem human subjects (PMHS) were tested simulating UBB conditions [95]. The pelvises were dissected superiorly at the L3-L4 intervertebral disc, and the femurs were removed from the acetabulum. The contents of the pelvic bowl were also removed to allow adequate room for instrumentation. A rigid pot (Fast Cast #891, Goldenwest Manufacturing, Grass Valley, CA) was used to create a rigid boundary condition, completely enveloping the remaining spine and attached rigidly at the sacral alae, leaving the sacroiliac joints unperturbed.

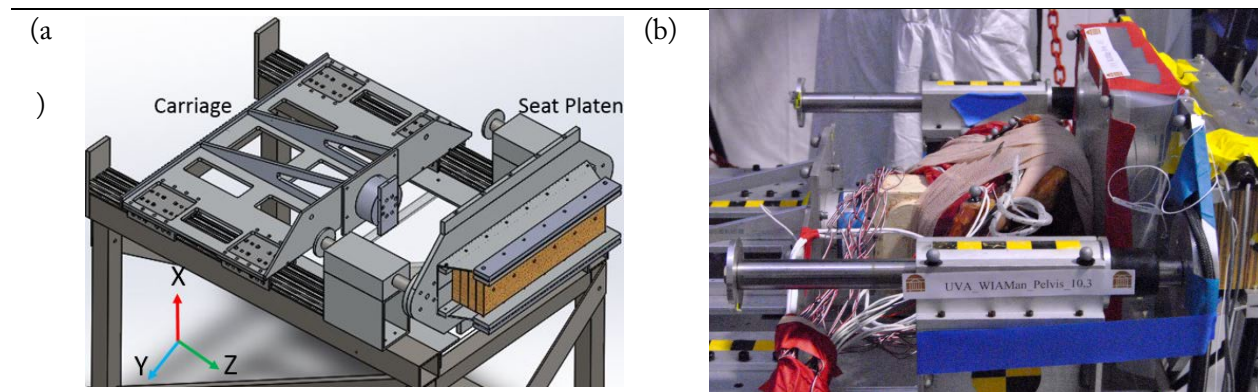


Figure 11. Experimental test rig for PMHS pelvis [95].

Three six-degree-of-freedom accelerometers were attached to the pelvis at the left ilium, right superior pubic ramus, and either posterior sacrum or anterior sacrum. Each accelerometer package contained the acceleration and angular rate in the local x, y, and z directions. An array of ten (10) strain gauges were attached: eight tri-axial gauges at the bilateral ilium, sacroiliac joint, superior pubic rami, and inferior pubic rami; and two single-axis strain gauges at the bilateral iliopubic eminence. The pelvic bowl was backfilled with ballistics gelatin (Custom Collagen, Addison, IL) to compensate the lost mass from the removed contents.

Three different pelvic angles were tested in this series of tests: 28°, 40°, and 56°. These pelvic angles were chosen to test a wide range of sitting postures to see possible effects on injury during axial loading. The pelvic angle was measured from a line between the midpoint of the left and right anterior superior iliac spine (ASIS) and the midpoint of the left and right pubic tubercle, and the z-axis (see Figure 12).

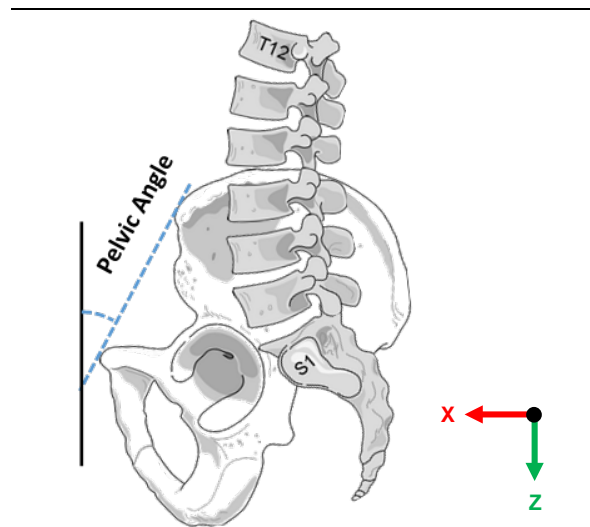


Figure 12. Method used to measure pelvic angle.

The pot was rigidly attached to a six-axis load cell to measure forces and moments on the lumbar end of the pelvis. This load cell was rigidly attached to a 12 kg carriage that represented the effective mass of a 50th percentile male's torso during high-rate axial loading. The carriage had ultra-high-molecular-weight polyethylene bearings that slid on a single-axis rail system (80/20 Inc., Columbia City, IN) (see Figure 11). Two constant-force springs were attached from the carriage to the static base of the rig to create a preload equal to the effective mass of the torso on the pelvis while sitting. The seat platen also slides on single-axis bearings and has an additional six-axis load cell attached. Downstream of the seat platen is a pneumatically driven impact piston that strikes the seat platen at a constant velocity, utilizing various rubbers and foams to tune the pulse impacted into the pelvis. The input velocity was 2 m/s with a 10 ms velocity rise time, and no injuries were recorded from these impacts. Additional tests following the 2 m/s impacts were performed

on the same pelves in ascending velocities. Following each increase in velocity, another 2 m/s impact was performed to compare to the original 2 m/s impact. Comparing data between the two tests sandwiching a higher impact test was used as a method to determine whether the pelvis had sustained any injuries. CT scans and autopsy of the pelves occurred only after all impacts were completed. While this method may be effective in determining if any gross injury had happened, it censors the data, and the data of any following impacts cannot have an absolute certainty that there was not pre-existing injuries that changed the results or influenced future injuries. Because of this fact, only initial hits were used as reference in this thesis.



## **3 Material Testing**

### **3.1 Introduction**

While in a seated posture, the gluteal muscles slide under the ischial tuberosities, creating padding of fat and muscle. Understanding how load travels through the pelvis when loaded vertically begins with the interaction of the load through the tissue into the ischial tuberosities. While there exists quasi-static testing of gluteal tissue in the literature, there is a lack of dynamic testing. From tissue mechanics, soft tissue is shown to be viscoelastic, meaning the stress depends on the strain rate. Therefore, using quasi-static material properties of gluteal tissue is not suitable for the dynamic environment of underbody blasts. Dynamic testing of other tissues also exists, but the literature shows that different tissue types can have different material properties. In order to accurately model gluteal tissue in vertical loading, it needs to be tested in the same conditions.

In this chapter, gluteal tissue is tested dynamically using a custom drop tower apparatus. The objectives of this chapter are to first, perform a sensitivity analysis to test appropriate input and boundary conditions. Second, gluteal tissue specimens are procured from post-mortem human subjects and prepared appropriately to perform compression tests. Third, a custom drop tower apparatus is built and is used to test the gluteal tissue specimens.

### **3.2 Design of Experiment**

#### **3.2.1 Sensitivity Analysis**

To determine appropriate test parameters for the tissue compression tests, a sensitivity analysis was performed. The analysis had two objectives: 1) determine the response of tissue size boundary effects with variations of tissue properties and test parameters, and 2) determine the response of substrate boundary effects for varying tissue thickness. The overall objective of these analyses was to find the maximum size of

indenter and the maximum displacement of the indenter into the tissue without being affected by significant boundary effects. While an inverse finite element approach was used to characterize the tissue material properties (discussed later in Chapter 3.1) which can generally recreate boundary conditions, it is desirable to minimize these effects to simplify the FE model.

A parametric finite element model (Figure 13) was created for this investigation using LS-DYNA (Livermore Software Technology Corporation, Livermore, CA). The model consists of an indenter that strikes the center of a tissue surrogate that sits on a static plate. The indenter was modeled as a rigid cylinder with a fillet on one end to avoid computational complications from sharp edges. The gluteal tissue was modeled using the GHBMCM50-O v4.4 simplified rubber material model for pelvis tissue (\*MAT\_SIMPLIFIED\_RUBBER/FOAM), modified with dynamic rate effects from dynamic testing performed on cadaveric heel pad samples by Gabler et al. [21]. The tissue was also meshed as a cylinder, utilizing a combination of radial and concentric circular lines to form elements that increase with size as the radius increases to reduce computational time. The concentric circular lines also allowed the model to be easily changed to different radii, all while keeping a cylindrical shape. Hexahedral elements were used, with the finest mesh at the center having approximately 2 mm edge lengths. The plate was modeled as a rigid solid and served as a rigid boundary condition. Two contacts were created using \*CONTACT\_AUTOMATIC\_SURFACE\_TO\_SURFACE between the impactor and tissue, and between the tissue and the static plate. The model was reduced to a quarter model with planes of symmetry to reduce computational time. The indenter and tissue were meshed using Hypermesh (Altair Engineering, Troy, MI).

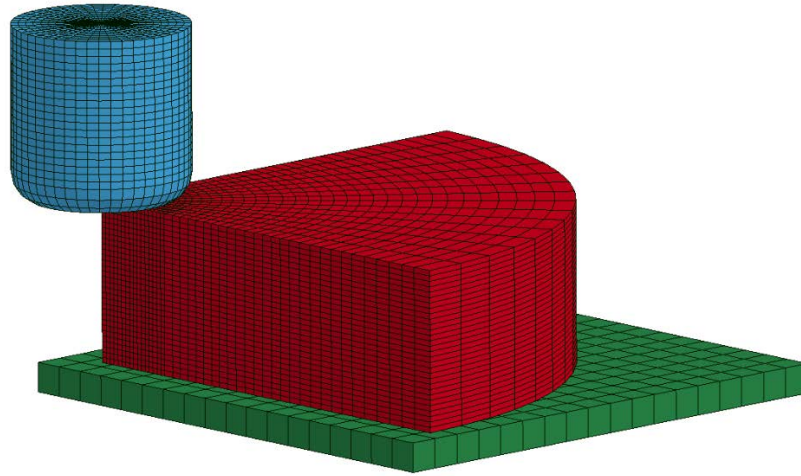


Figure 13. Parametric FE model of tissue used in the sensitivity analysis.

For the first part of the sensitivity analysis, tissue thickness, tissue stiffness, indenter velocity, and indenter displacement served as the parameters. A value for each parameter was chosen to form a base condition for comparison. Tissue thickness values were chosen from initial measurements taken of the tissue specimens and represent the thinnest, mean thickness, and thickest specimens. The nominal tissue stiffness was the tissue properties calculated by Gabler et al. Indenter velocity and displacement values were chosen as ranges achievable by equipment used later in this study. A realistic range (Table 2) of each parameter was simulated with each change in parameter tested individually at a range of tissue sizes. The tissue size was expressed as a ratio of the tissue radius,  $r$ , to the indenter radius,  $R$  (referred to from here onward as radius ratio, and shown as  $r/R$ ). The radius ratio was varied from 1 to 15 with the ratio of 15 serving as the “infinite” case which was absent of boundary effects. Boundary effects from the infinite case were considered absent since any increase in ratio resulted in less than a 5% change in the force response with the change getting smaller as the ratio increased past 15. The baseline model had the following parameters: 55 mm tissue thickness, nominal tissue stiffness, 5 m/s indenter velocity, and 50% indenter displacement.

Table 2. Sensitivity analysis

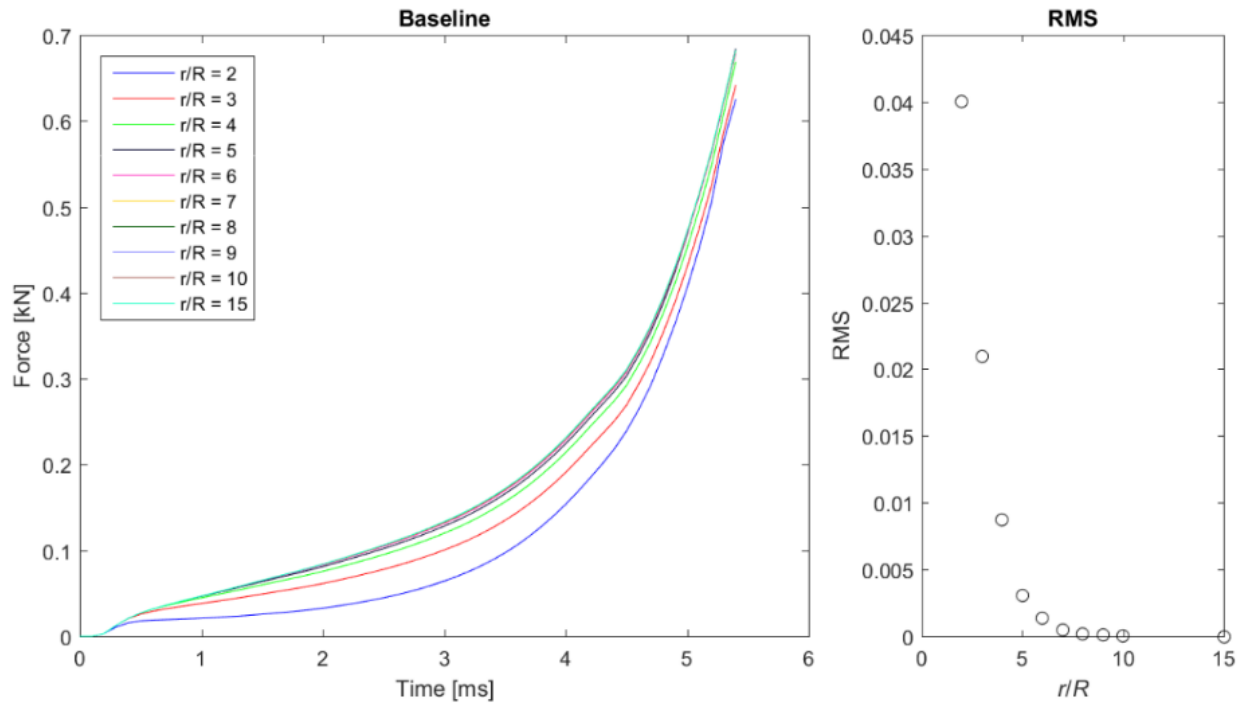
Parameters	Values Tested
Tissue Thickness	35 mm, 55 mm, 85 mm
Tissue Stiffness	± Order of magnitude of dynamic stiffness response
Indenter Velocity	5 m/s, 10 m/s
Indenter Displacement	25%, 50%, 75% of tissue thickness

The force-time trace of the radius ratios at each parameter level were compared to the “infinite” case. The root-mean-square error (RMSE; see Equation 1) was also calculated to compare each set of results to the infinite case ( $\hat{y}_i$ ).

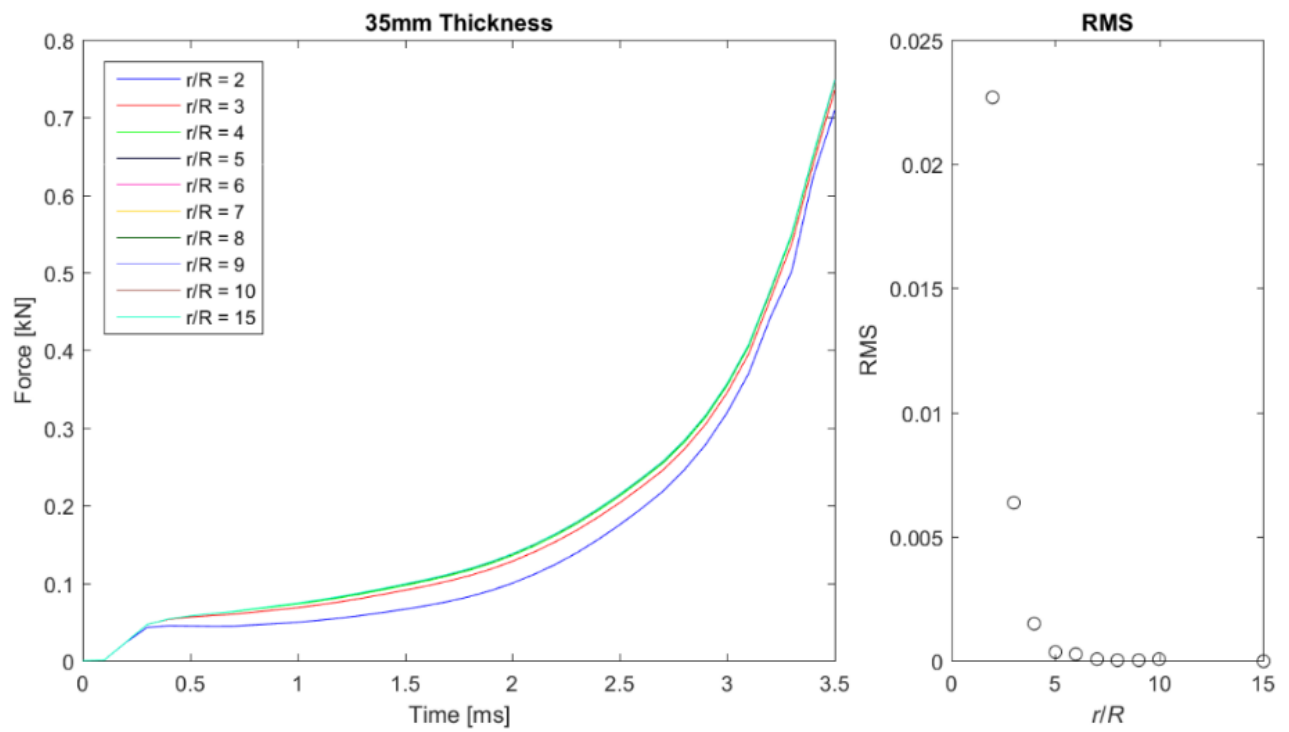
$$RMSE = \sqrt{\frac{\sum_{i=1}^n (\hat{y}_i - y_i)^2}{n}} \quad \text{Equation 1}$$

Force-time and RMSE results can be found in Figure 14. In the baseline model, all radius ratios share a similar shape, with a  $r/R$  value of 4 almost completely converging to the “infinite” case of  $r/R = 15$ . When varying thickness, the thinner tissue converged quicker than the thicker tissue. The thinner tissue (35 mm) converged by a radius ratio value of 4, while the thicker tissue (85 mm) did not converge until a value of 6. Comparing the change in tissue stiffness, the less stiff tissue converged to a radius ratio of 5, while the stiffer tissue seemed nearly insensitive to the radius ratio. The 10 m/s model was very similar to the base case and also converged to a radius ratio of 4. Larger displacements converged much quicker than smaller displacements, with the 25% model converging to a  $r/R$  ratio of 5 and the 75% model being seemingly insensitive to change in ratio.

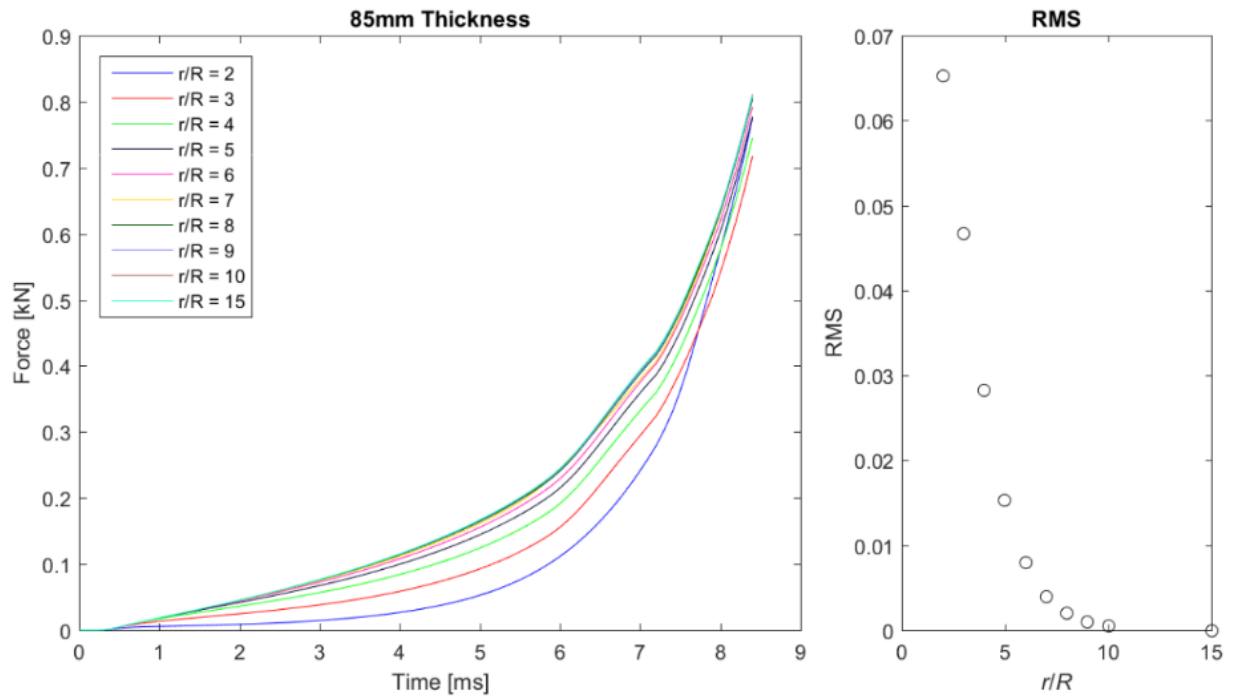
(a)



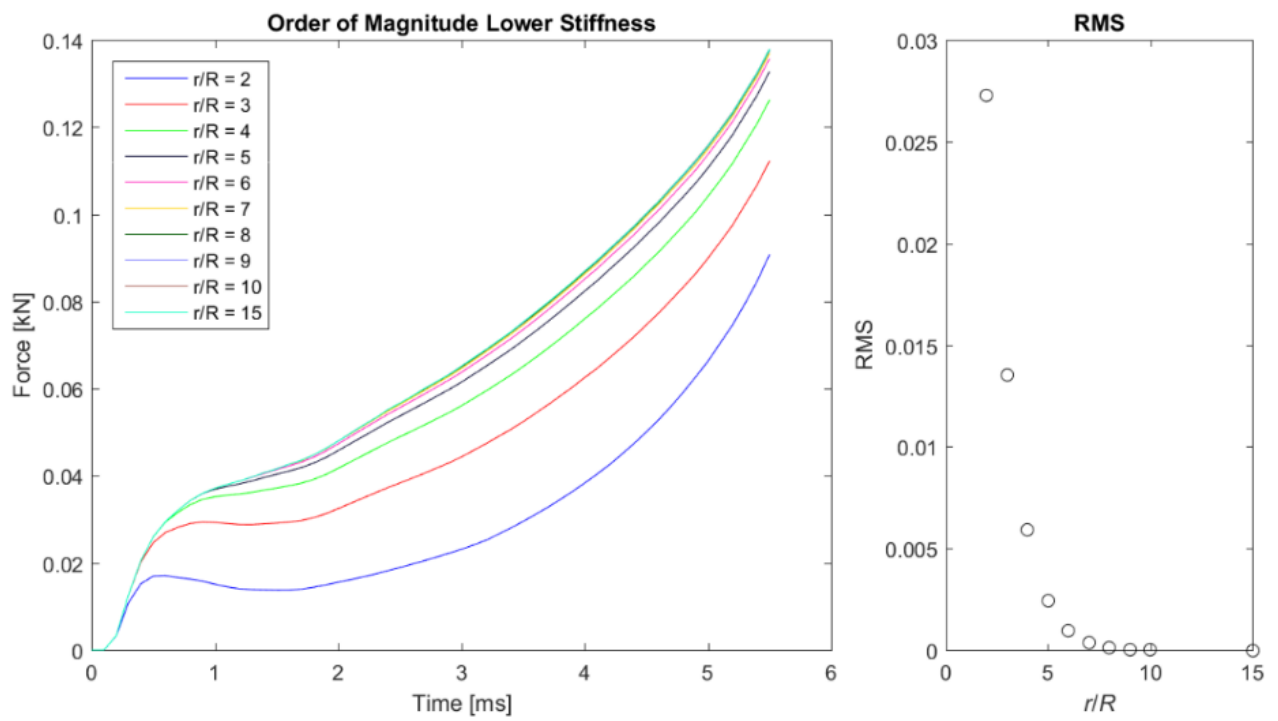
(b)



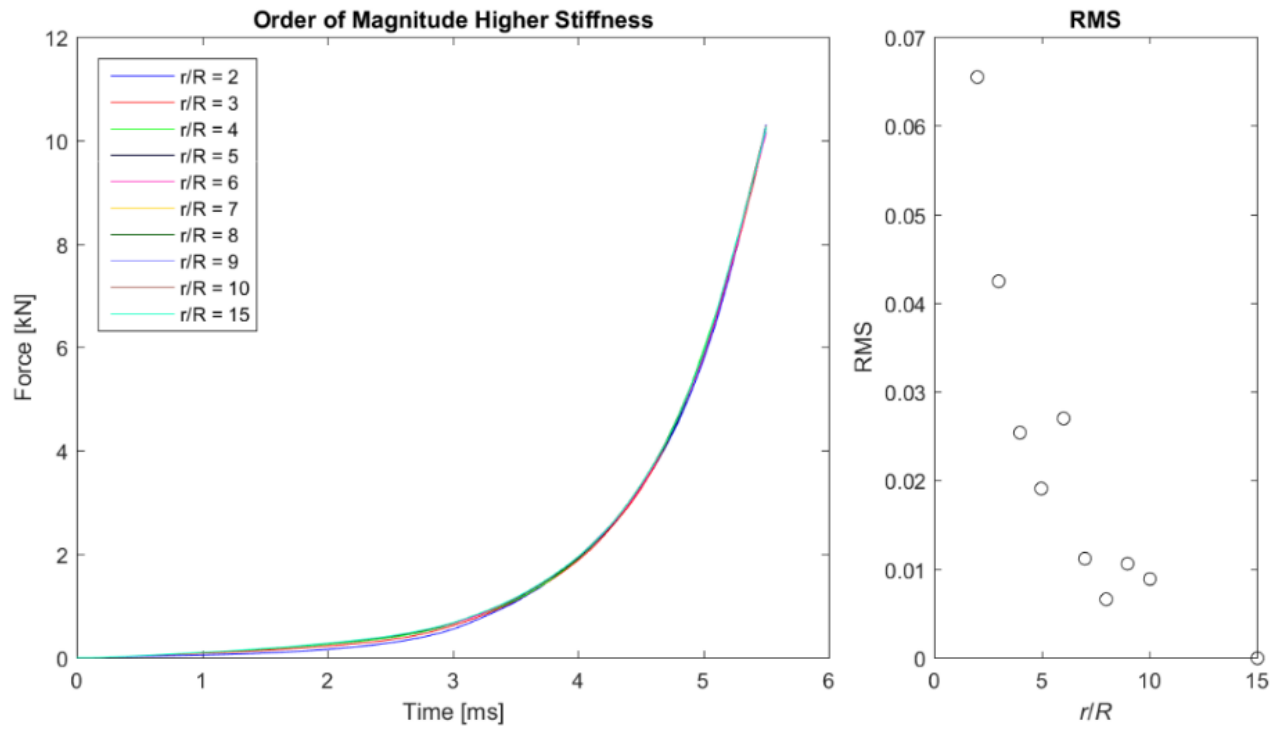
(c)



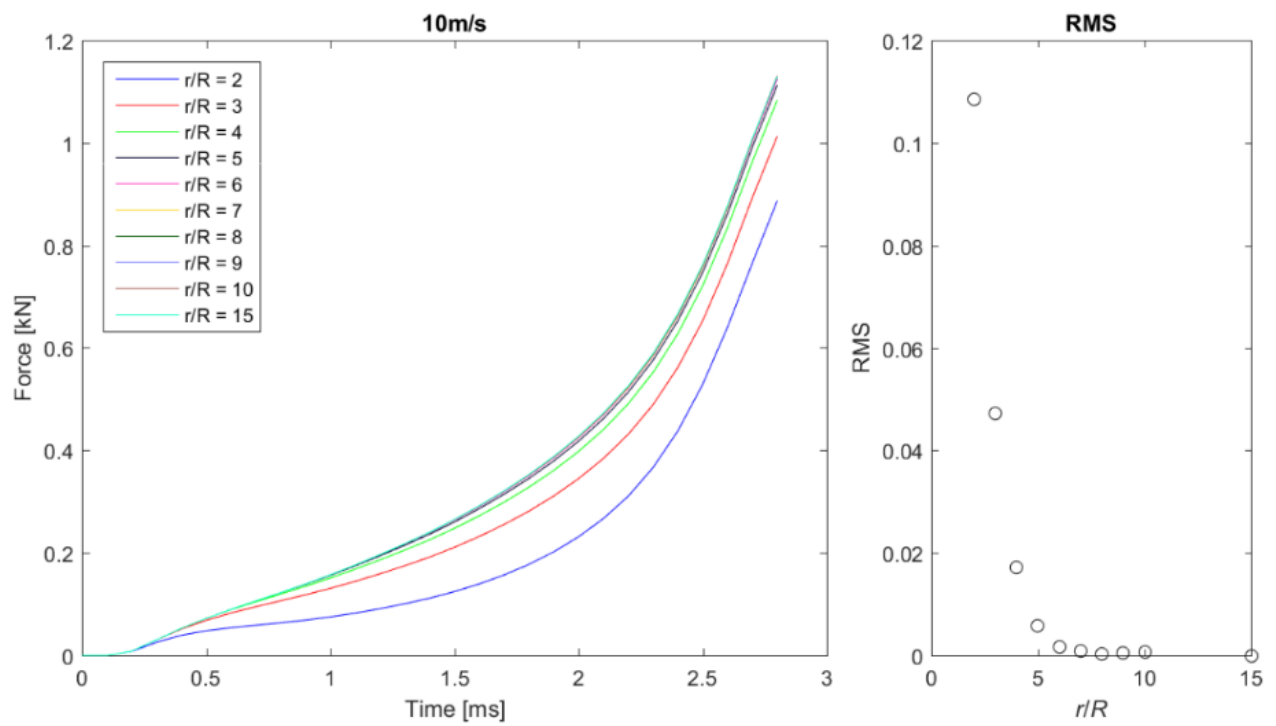
(d)



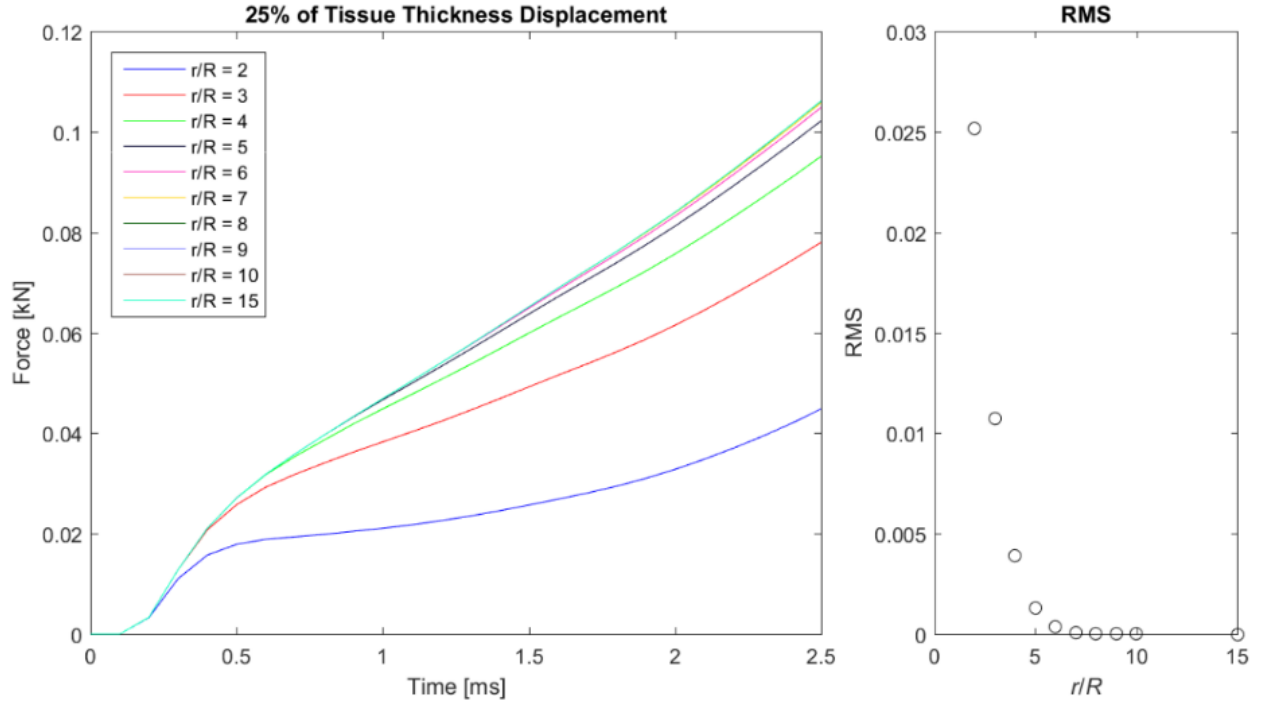
(e)



(f)



(g)



(h)

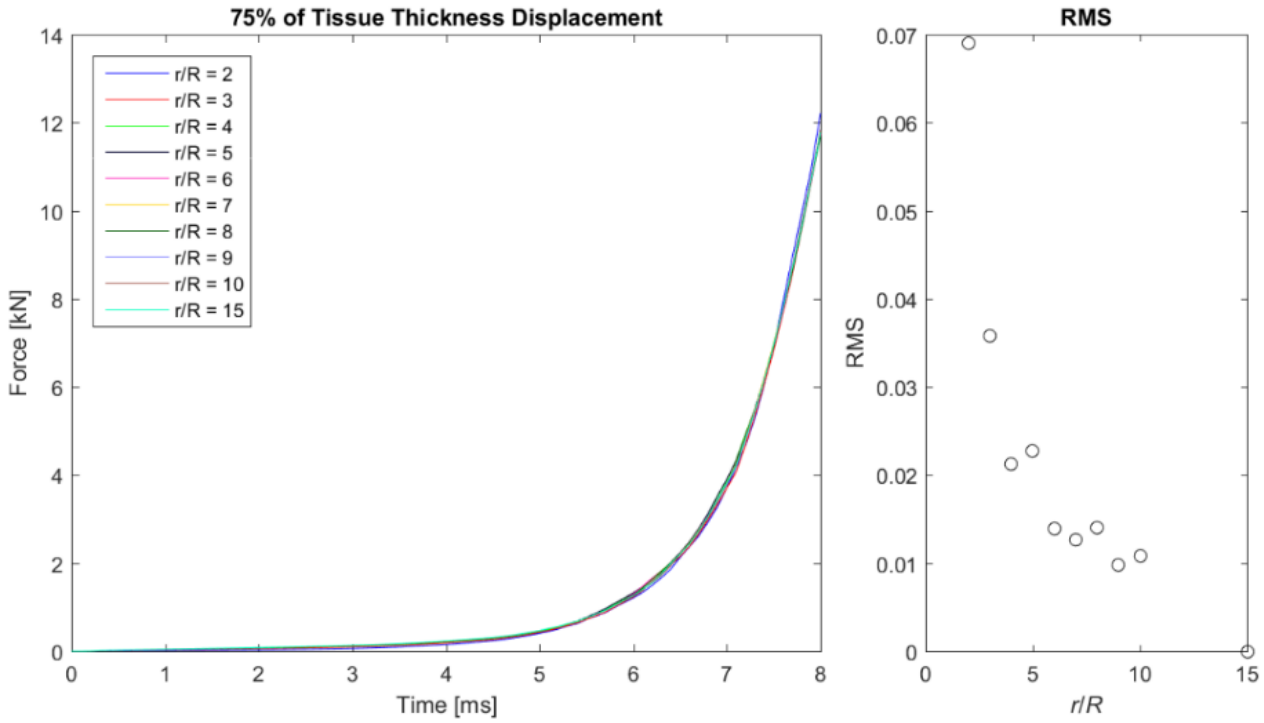


Figure 14. Results from the first part of the sensitivity analysis: baseline (a), variations in tissue thickness (b–c), tissue stiffness (d–e), indenter velocity (f), and indenter displacement (g–h).



Based on these results, a radius ratio of 5 was chosen. The actual size of each sample tissue to be tested was based on the smallest tissue sample collected so that all specimens could be used and be uniform in diameter. Each specimen had a finite area where a relatively even layering of muscle, fat, and skin was present suitable for testing. The tissue sample with the smallest suitable testing area was used as the base for the radius ratio. This sample measured approximately 110 mm in diameter; therefore, the tissue sample size radius was chosen as 55 mm with an indenter radius of 11 mm.

### **3.2.2 Strain**

From the UBB experimental PMHS pelvis tests described in Chapter 2.6, it is not possible to tell how much the gluteal tissue was compressed with the instrumentation suite used. However, it was possible to make a good approximation based on early developments of the VIP FE model described in detail later (Chapter 5). Measurements of soft tissue compression were taken from various areas on the pelvis during no load, pre-compression, and peak loading (Figure 15). Magnitudes of compression varied significantly by location, with some areas receiving very little compression and peak compression nearing 75% in prominent areas such as the ischial tuberosity. However, due to design constraints in the drop tower testing (see Chapter 3.4), 50% overall compression was targeting in order to consistently test across specimen variability in thickness and stiffness.

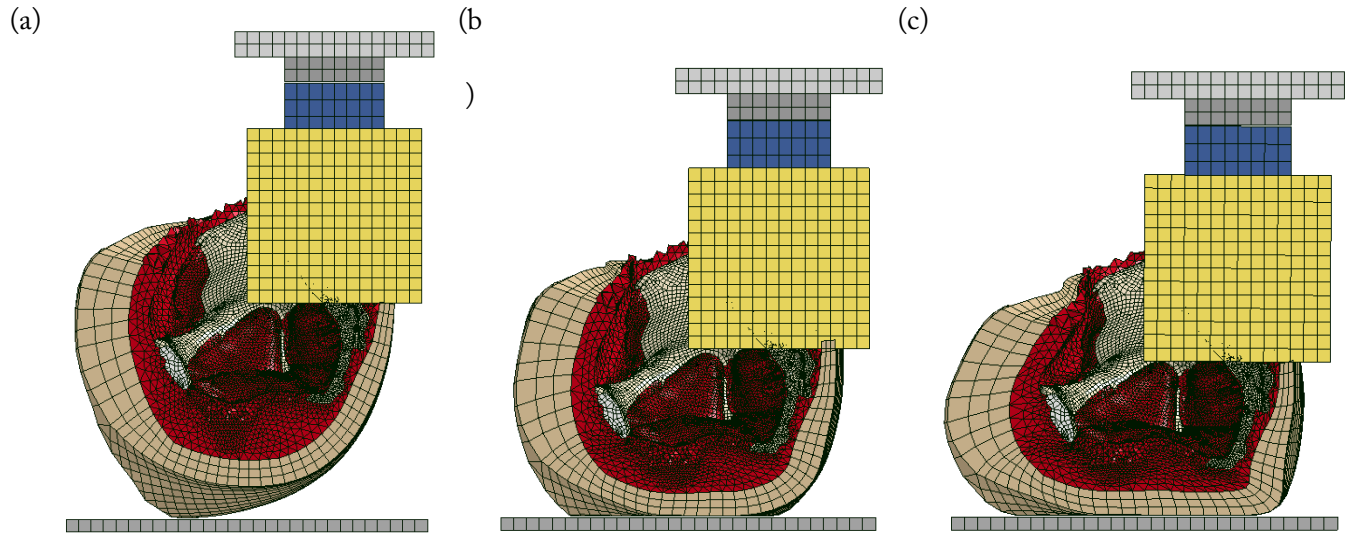


Figure 15. Pelvis component FE model under no compression (a), preload (b), and loading (c).

### 3.2.3 Strain Rate

Tissue is well known to exhibit viscoelastic properties; therefore, it was imperative to test the tissue at the correct strain rates. In this case, it was desired to at least match peak strains seen in the UBB experimental pelvis tests. While input velocities from the pelvis PMHS tests were known ( $\sim 2$  m/s), it was uncertain whether the difference in boundary conditions and loading mechanisms between the PMHS pelvis tests and the tissue indentation tests would result in the same peak strain rates. To estimate the strain rates of the gluteal tissue from the UBB experimental pelvis tests, an early version of the VIP FE model was utilized. This early version used \*MAT\_SIMPLIFIED\_RUBBER as its tissue material model which was used in the GHBMC v4.4 pelvis model. Only a single load curve was referenced, which meant that there was no differentiation between different strain rates. While it was acknowledged that this material would not accurately represent tissue in dynamic loading for the purposes of the testing in this thesis, it was sufficient to set up the design of experiments.

Strings of beam elements were implanted into the pre-compressed gluteal tissue, positioned perpendicularly to the loading plate. The keyword `*CONSTRAINED_BEAM_IN_SOLID` was used to capture the deformation of the tissue elements so that strain could be calculated. The beams were formulated using `*MAT_NULL` with very low density and stiffness to avoid affecting the deformation and motion of the tissue. Nineteen beams were implanted near four bony locations: coccyx, ischial tuberosity, superior pubic ramus, and posterior superior iliac spine (PSIS). Each string of beams spanned from the skin to bone. The closest four beams to the skin and to the bone were initially 1 mm in length, with the remaining beams evenly spaced between. The end nodes' (i.e. the node at the bone and at the plate) coordinates were used as the end points when the tissue was compressed after 500 ms of precompression. This was done in order to avoid kinking the beams during the significant compression of the tissue prior to the impact. This allowed the beams to be orthogonal to the impact plate prior to the impact.

To calculate strain and strain rate, each node's position from the beam elements was recorded. The length of each beam was calculated from the x-, y-, and z-coordinates from the nodes on either end of the beam, and Green strain was used to calculate strain. Green strain is commonly used for large displacements.

$$\varepsilon_G = \frac{1}{2} \left( \frac{l^2 - L^2}{L^2} \right) \quad \text{Equation 2}$$

The current length is represented by  $l$  and the initial length by  $L$ . Then, strain rate was calculated from the strain-time history by using the finite difference method. The forward difference method was used for the first time step, the backward difference method for the last time step, and the central difference method for all other time steps.

$$\text{Forward Difference Method } f' = \frac{f(i+1) - f(i)}{\Delta t} \quad \text{Equation 3}$$

$$\text{Central Difference Method } f' = \frac{f(i+1) - f(i-1)}{2\Delta t} \quad \text{Equation 4}$$

$$\text{Backward Difference Method } f' = \frac{f(i) - f(i-1)}{\Delta t} \quad \text{Equation 5}$$

The strains and strain rates of the beams imbedded into the gluteal soft tissue were compared (see Figure 16). Because the soft tissue of the pelvis FE model is made of two parts—an outer layer of hexahedral elements and an inner layer of tetrahedral elements—some unstable behavior occurred at the boundary of the two layers. In addition, because of the unstable behavior of the tetrahedral layer in general, the beams that resided in that portion were omitted. Only the beams that were imbedded in the outer, hexahedral layer were used.

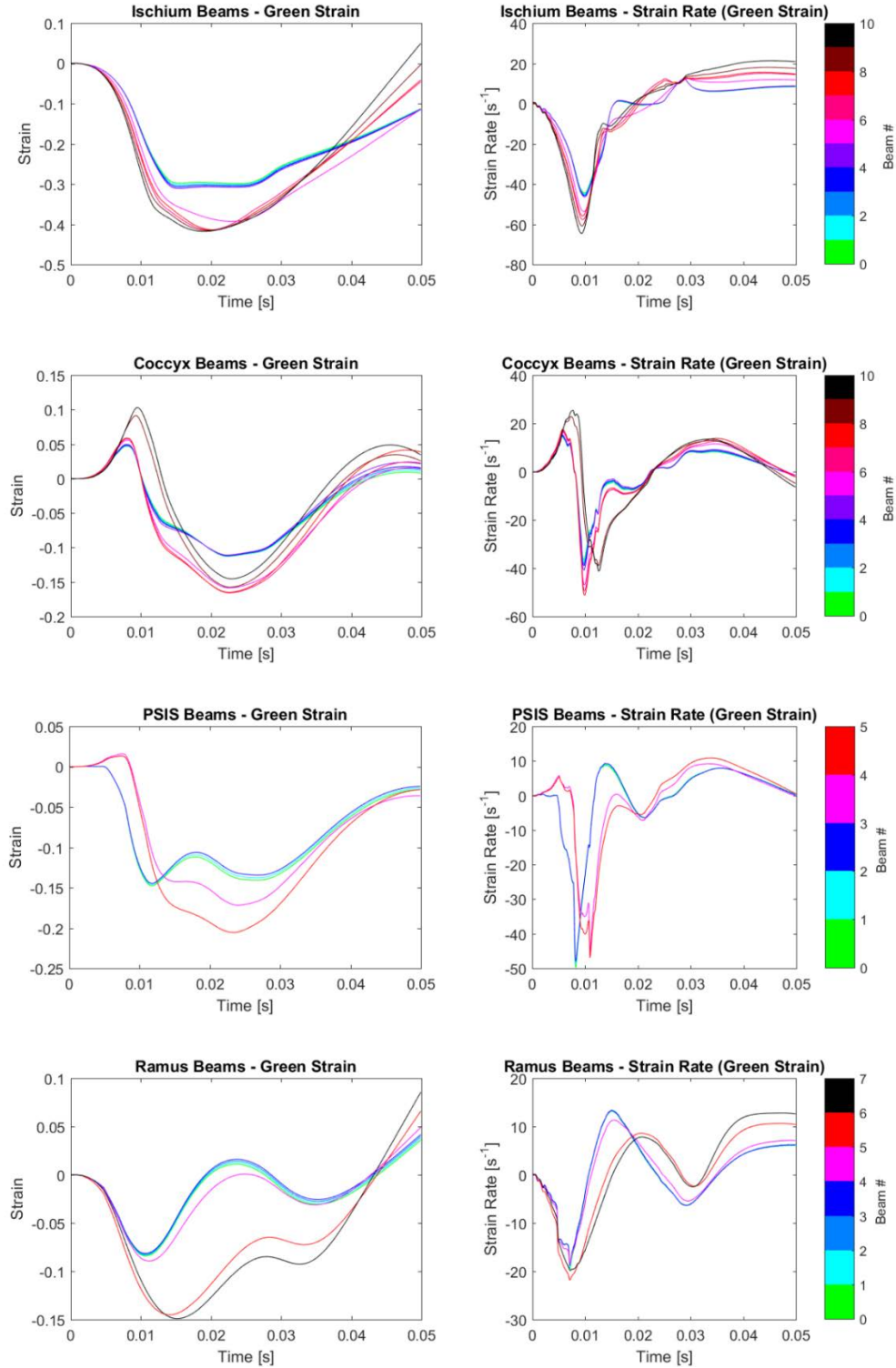


Figure 16. Strain and strain rates of beams on the ischial tuberosity, coccyx, PSIS, and superior pubic ramus. Lower beams numbers represent beams closer to the skin, and higher beam numbers represent beams closer to the bone.

The ischium was subjected to both the highest strains and strain rates with -0.42 and -65 s<sup>-1</sup>, respectively (negative sign indicates compression). A summary of the strains and strain rates can be found in Table 3.

Table 3. Peak strains and strain rates of gluteal tissue beams

Location	Peak Strain	Peak Strain Rate [s <sup>-1</sup> ]
Ischial Tuberosity	-0.42	-65
Superior Pubic Ramus	-0.15	-22
PSIS	-0.21	-50
Coccyx	-0.17	-51

Because the outer layer of tissue is only three elements thick at most places, there was little variation between some of the beams. Many adjacent beams produced almost identical strain and strain rates because they were completely enveloped in the same element.

To back out the needed input velocity to match the peak strain rate, the strain rate was simplified as shown in Equation 6.

$$\epsilon' = \frac{d\epsilon}{dt} \approx \frac{\epsilon}{\Delta t} \quad \text{Equation 6}$$

A linear displacement was assumed, with average specimen thickness (44.2 mm) and 50% strain. Solving for  $\Delta t$  led to a required 2.85 m/s to achieve 50% strain with a 65 s<sup>-1</sup> strain rate. Based on designs of the drop tower testing that were in development at the time, it was believed that a linear displacement step-hold was a reasonable assumption. Based on this, a 3 m/s input velocity for the tissue testing was decided.

### 3.3 Specimen Preparation

Eleven gluteal soft tissue specimens from 8 PMHS were dissected from male pelvises. All tissue was screened for Hepatitis A, B, and C, and HIV and was fresh-frozen after procurement. Computed tomography (CT) scans were performed before any testing to screen for any pre-existing injuries. All protocols were reviewed

and approved by the University of Virginia Institutional Review Board (IRB) and the internal lab protocol committee.

During dissection, care was taken while separating the tissue from the bony pelvis to leave as much of the muscle as possible intact. Tissue from the area inferior to the ischia and on the posterior surface of the ilium was kept and separated into left and right specimens down the midline of the sacrum and coccyx. The anteriorly facing tissue of the pelvis was not included. The specimens were then stored flat and kept frozen.

The specimens were then cut into cylinders using a drill press while frozen (Figure 17a). Using T-slotted aluminum (80/20 Inc., Columbia City, IN), a frame was created to clamp the tissue (Figure 17b) to the drill press table. The two sides of the frame were made adjustable to account for the various sizes of soft tissue dissected from the pelvis. The frame was placed on top of plywood that sat on top of the drill press table. Two c-clamps held the frame and wood into place. An 82.5 mm deep hole saw with an inner diameter of 110 mm and a fine tooth pattern was attached to the drill press to cut the tissue. After coring, each piece of tissue was immediately returned to the freezer.

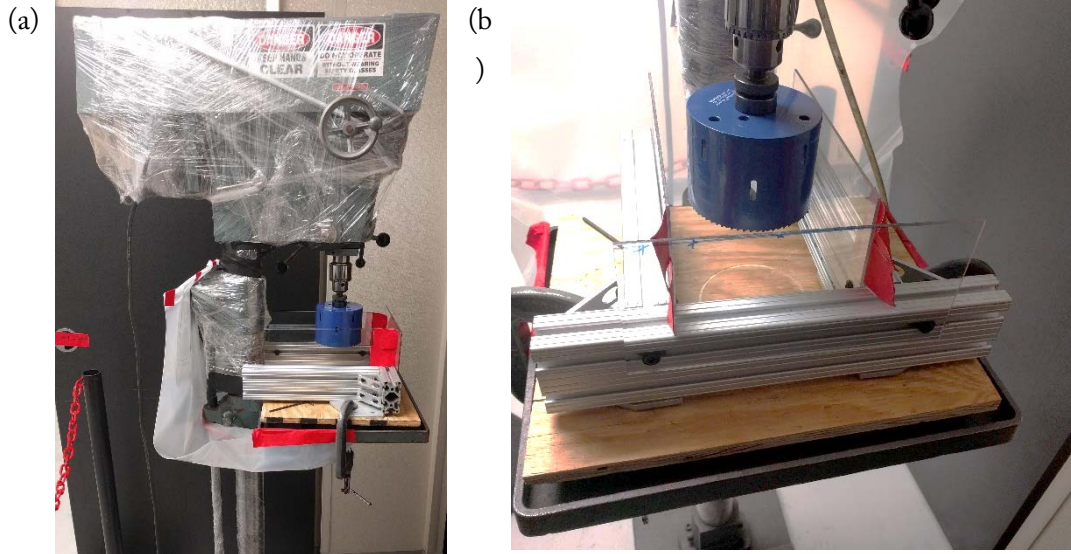


Figure 17. A drill press (a) and hole saw (b) were used to cut each piece of tissue down to a 110 mm diameter cylinder.

Prior to testing, each sample was thawed for at least 12 hours to ensure that it reached room temperature. The samples were thawed in clear acrylic tubes with an inner diameter of approximately 111 mm. Using ultrasound (Aixplorer®, Supersonic Imagine, Aix-en-Provence, France), a perpendicular plane in each quadrant of the tissue (Figure 18a) was imaged to obtain fat, muscle, and skin thicknesses (Figure 18b).

To calculate each tissue composition percentage (e.g. the volume percent of the tissue made up of muscle), each quadrant was approximated as three truncated right triangular prisms, one for each type of tissue (Figure 18c). The volume of each prism was calculated and summed by tissue type, and overall tissue percentages were calculated from these sums. As evident in Figure 18b, the tissue specimens rarely had even layers of fat and muscle. Because ultrasound imaging can typically only recreate 2D planes, the actual volume of each tissue type would have to be approximated. This method of percent volume approximation was chosen because the triangular prisms could account for gross non-uniformity in the muscle-fat layers, while still being able to easily calculate volume. Figure 18d shows the uneven triangular prisms approximating the uneven muscle and fat layers with the ultrasound image from Figure 18b overlaid.



Because each quadrant of the tissue is pie-shaped in reality, there is a significant amount of error in the volume between the prism approximation and the actual pie-shaped quadrant, so while it makes a reasonable approximation for relative percent volume, the prisms cannot be used for the total overall volume of the tissue. Instead, since each tissue specimen was thawed in a tube and kept a nearly perfect cylindrical shape along the circumference, the actual overall volume of each specimen was approximated as a cylinder with a height equal to that of the average of the five overall height measurements (four edge measurements and one center). Hand measurements using a ruler were also performed in case of any ambiguous fat-muscle boundaries in the ultrasound images. The mass of each specimen was taken prior to testing. A summary of specimen thickness and tissue percentages can be found in Table 4.

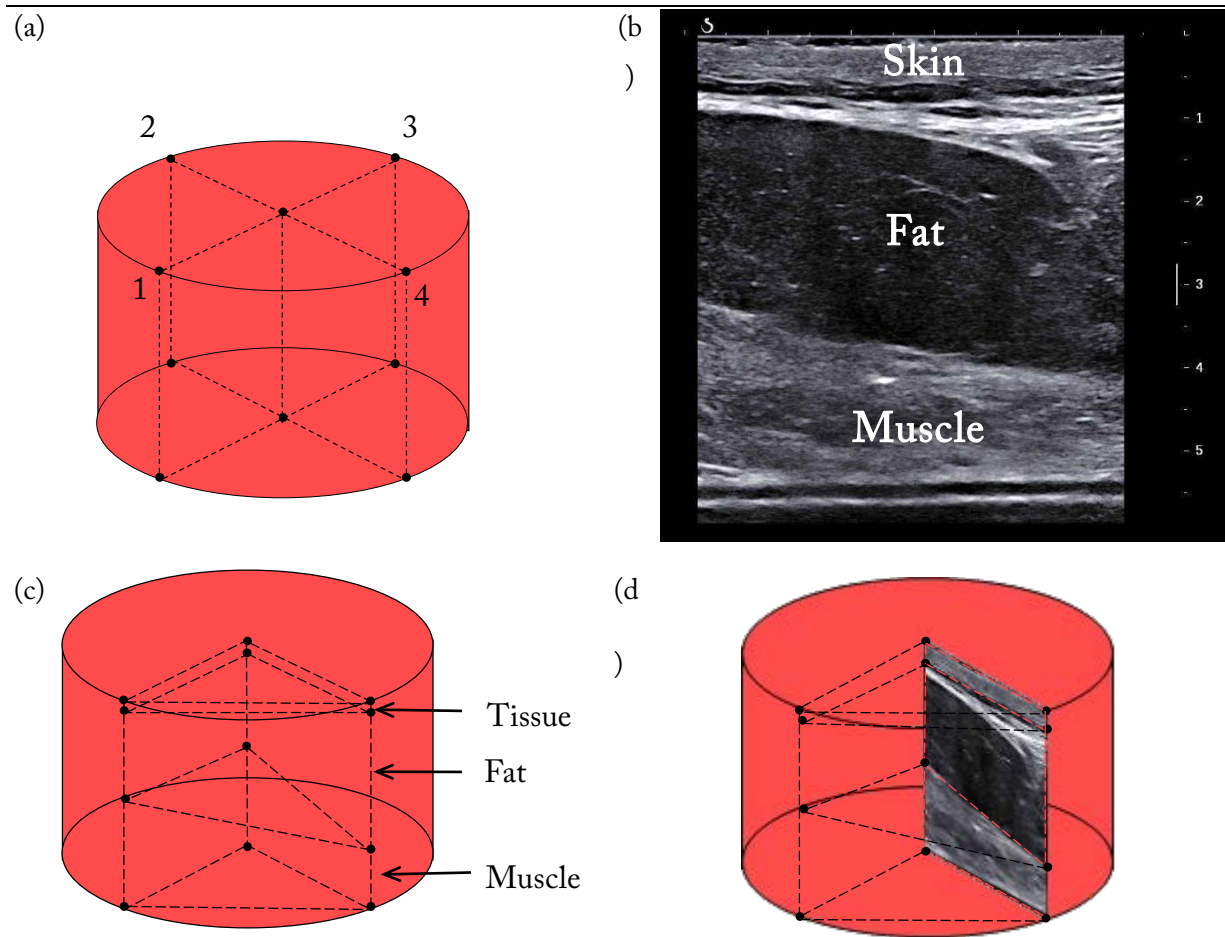


Figure 18. Four planes (a) were imaged using ultrasound (b) to obtain skin, fat, and muscle thicknesses of each sample. Ultrasound planes were used to approximate volume percentages by using right triangular prisms (c). Notice the triangular prisms capturing the gross uneven fat and muscle layers found in the ultrasound image (d).

The specimen matrix for this part of the study is found in Table 4. The average donor age of the specimens was 68.5 years, with a BMI of 24.9 kg/m<sup>2</sup>. The average specimen thickness was 44.1 mm with a mass of 400 g. The thickest specimen was 52 mm and the thinnest was 39 mm. Averaged muscle volume percent, fat volume percent, and skin volume percent were 49.8, 42.5, and 7.7, respectively. BMI, specimen mass, and specimen thickness all had weak or no correlations with respect to muscle/fat percentages (see Figure 52). While a high BMI was thought to possibly correlate with fattier specimens, this was not the case in this data set. This could be for many reasons including variations in body type and location of sample taken

from the PMHS. BMI was also not seen to correlate with specimen mass or thickness. Only specimen mass and thickness were found to have a strong correlation, which was expected.

Table 4. Summary of specimen soft tissue contents.

Specimen	Age	BMI	Specimen Mass (g)	Thickness (mm)	% Muscle	% Fat	% Skin
805L	67	24	360	40	56.2	38.0	5.8
805R	67	24	375	41	57.2	36.9	5.8
811R	65	27.9	370	39	53.5	38.6	7.9
831L	67	19.0	420	47	50.9	42.9	6.2
831R	67	19.0	400	45	55.1	37.8	7.1
836R	67	29.6	380	41	35.0	55.9	9.0
837L	68	23.8	375	41	47.4	43.4	9.2
869L	73	29.4	440	47	41.5	47.4	11.1
869R	73	29.4	485	52	46.1	47.3	6.6
874R	59	26	365	45	54.4	36.5	9.1
876L	80	21.9	435	47	50.5	42.8	6.6
Average	68.5	24.9	400.5	44.1	49.8	42.5	7.7
Standard Deviation	5.4	3.9	39.8	4.0	6.8	5.9	1.7

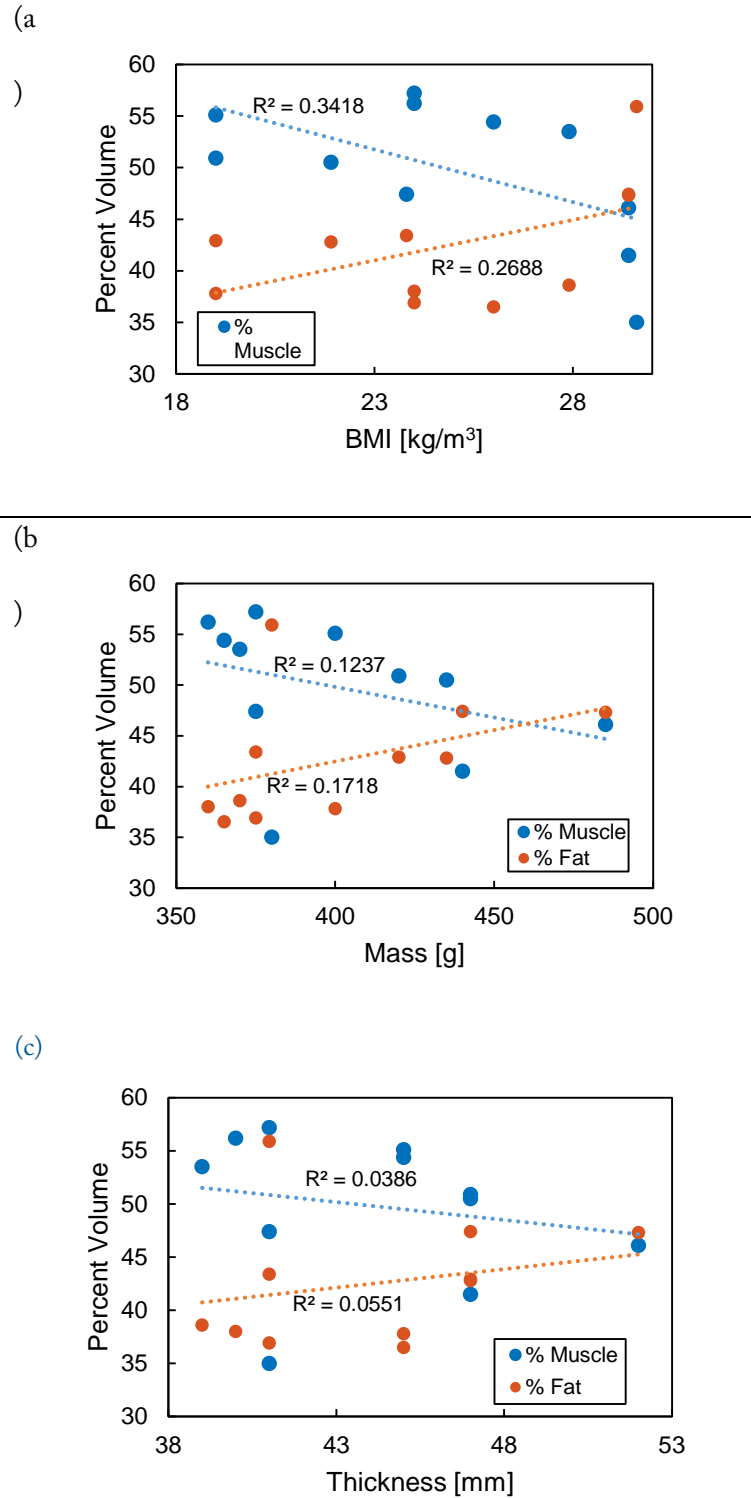


Figure 19. BMI (a), mass (b), and thickness (c), did not correlate will with percent volume of muscle and fat.

## 3.4 Drop Tower Testing

### 3.4.1 Design

To achieve high-rate compression of tissue, a custom drop tower rig was created (Figure 20). A two-stage indentation system was created using a heavy drop mass that impacts an indenter, which in turn strikes the tissue specimen. The drop mass consisted of a crossbar that slides vertically on plastic bearings to keep aligned. An adjustable mass is attached to the bottom of the crossbar with a spherical indenter attached through the drop mass to the crossbar. The spherical indenter insures a singular point of contact to the indenter crossbar. Two padded blocks sit atop 19 mm [0.75 in] threaded rods to arrest the drop weight after it impacts with the indenter crossbar and before the indenter strikes the specimen, ensuring that the mass from the drop mass is not transferred into the indenter system.

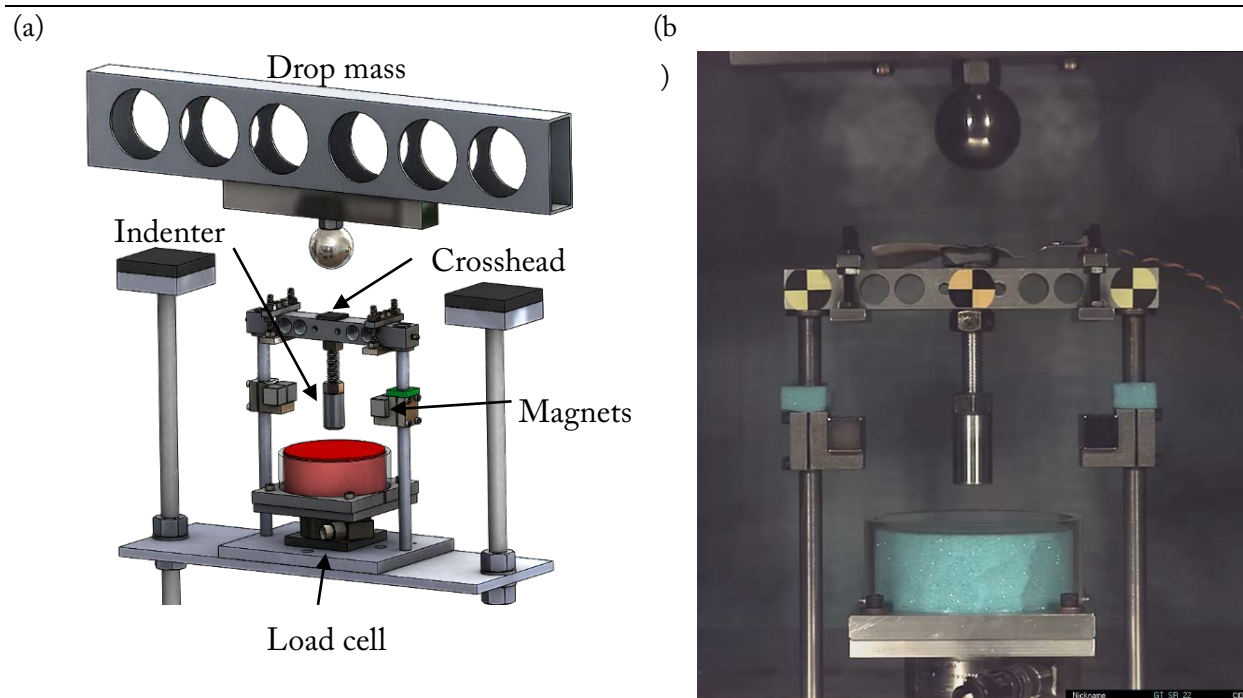


Figure 20. A schematic (a) of the indenter device and an overall photo (b) of the drop tower setup.

The indenter crossbar slides vertically on two 12.7 mm [0.5 in] shafts using oil-embedded bronze sleeve bearings. A cylindrical indenter is attached to the crossbar by a 12.7 mm [0.5 in] in diameter threaded rod. Photo targets were placed on the center and on each end of the crosshead in front of the bearings. A high-speed camera (nac Image Technology, Simi Valley, CA) was placed orthogonal to the indenter, using levels to ensure orthogonality. The camera sampled at 4000 Hz and an open-source motion tracking program (Tracker, [www.physlets.org/tracker](http://www.physlets.org/tracker)) was used to track the displacement of the indenter. The tissue sat on a substrate attached to a 2.2 kN [500 lb] load cell (Honeywell, Columbus, OH) sampling at 20 kHz.

A “step-hold” is achieved through a magnet-catch system. Two steel plates are attached to the bottom of the indenter crossbar by an adjustable threaded rod. Custom steel shaft collar clamps were attached on each shaft and are adjustable to accommodate varying specimen thicknesses. The interior half of each shaft collar has a 90° step which allows cubic magnets to sit. Each shaft collar houses two cubic magnets (BCCC-N52, K&J Magnetics, Inc., Pipersville, PA) that have 12.7 mm [0.5 in] in side lengths. Before the test begins, the indenter cross head is held at the top of the shafts by two spring plungers that mate into small divots in the side of each shaft. When the drop mass strikes the indenter crossbar, the spring plunger nose force is exceeded and is released from the divot. The indenter then strikes the center of the tissue specimen. The shaft collars are positioned to arrest the indenter after the maximum displacement is reached. When the indenter reaches the maximum displacement into the specimen, the steel plates attached to the indenter crossbar attract to the magnets housed on the shaft collars and prevent the indenter from rebounding off the tissue specimen.

During a pilot test, it was clear that some tissue cylinders would have a tendency to sag in a certain direction and no longer keep a cylindrical shape. Most specimens did not have a flat fat-muscle boundary, which creates sagging along the boundary due to the difference in stiffness between fat and muscle. While the

indenter to tissue radius ratio was designed to minimize boundary effects at the circumferential surface, the thickness of the tissue immediately underneath the indenter was found to be the most sensitive factor in the force-time response. Therefore, it was important to keep the tissue in the same position that it was measured. To keep the tissue constrained, each specimen was kept in the clear acrylic tube that it was thawed in. Two brackets of aluminum were made to clamp the tube circumferentially in the center of the load cell plate and prevent the tube from rattling during loading.

The input velocity was defined as the velocity of the indenter at the moment it begins to strike the tissue. To capture this moment, a small piece of copper was placed on top of the skin of the tissue where the indenter would strike. The piece of copper was cut to be smaller than the diameter of the indenter to ensure that it did not create any boundary effects between the tissue and indenter. A corresponding small trigger strip made out of two separated pieces of copper was taped to the bottom of the indenter that would strike the copper on the tissue. The trigger strip was made as small and thin as possible, with small gauge wires wrapping around the indenter to avoid boundary effects. The DAS system was set to trigger when a complete circuit was detected in the trigger strip. The complete circuit was created when current was passed from one piece of copper on the trigger strip to the other by way of the piece of copper on the tissue. Before each test, with the magnets moved out of the way, the indenter was slid down to check the positioning of the piece of copper and ensure that it would successfully trigger.

Pilot tests were performed to find the drop heights necessary to achieve 3 m/s and a range of input velocities around 3 m/s. Because of the low friction of the rails used to constrain the drop mass and because the drop mass was released using an electromagnet, it was found that the drop tower was very repeatable (usually within 0.1 m/s of the target velocity).

The data from the load cell in the drop tower was found to pick up a lot of noise. The drop tower base was made out of wood, with a platform made out of aluminum and supported by a series of aluminum rods offsetting it from the base. Because of this, the load cell was not well isolated and picks up a lot of vibration.

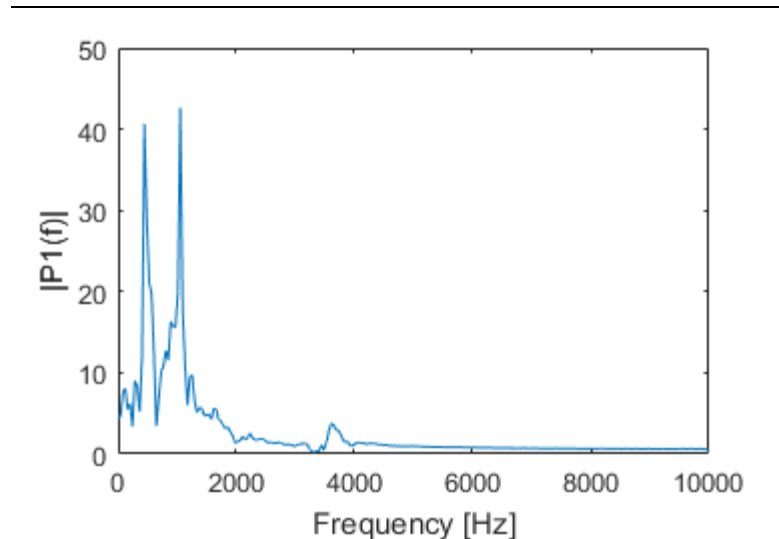


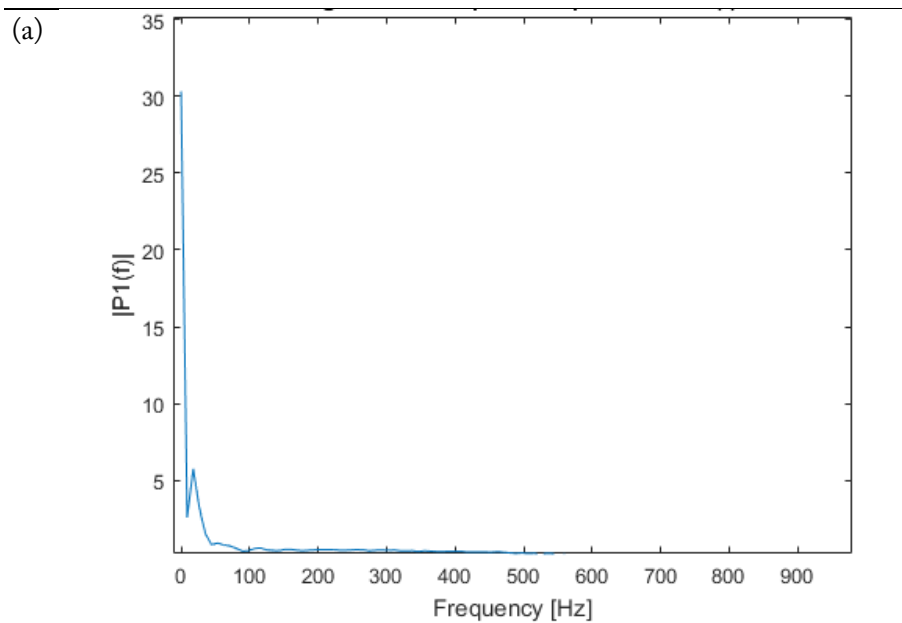
Figure 21. Example of power spectral density estimate from rig isolation pilot test. The two large spikes are two frequencies that are attributed to metal ringing on the rig.

---

A series of pilot tests were performed to try to attribute certain frequencies from the noise to various parts of the rig. Several tests were run with only the drop mass (indenter setup was not present), and several more tests were run with the drop mass hitting the indenter, but without a specimen present. Lastly, several tests were performed by manually indenting the foam tissue surrogate as quick as possible without using any moving parts from the rig. Power spectral density (PSD) estimates were calculated by using fast Fourier transforms (FFT) for each test to divide the frequency components from each test. The PSDs were compared from each set of pilot tests, and it was found that all the high frequency content was attributed to the rig and not the tissue. The metal base, the drop mass arresters, and the indenter crosshead striking the shaft collars were all thought to contribute to this noise. To try to decrease the noise, thicker foam between the shaft collars and indenter crosshead was used, but without costly and time intensive



modifications, little could be done to the other contributors. Based on the PSD analysis, however, the frequency content from the specimen alone was extremely low ( $<100$  Hz), and a CFC 180 (300 Hz) filter was able to filter out most of the high frequency content from the rig (see Figure 52). The peaks of the raw and filtered data were also compared to ensure that the peaks and overall shape of the signal were not drastically changing when filtered. The test with the biggest change in peak force due to filtering was about a 5% drop in value, with most tests only decreasing a couple percent after filtering.




---

Figure 22. Example power spectral density plot of the isolated tests in which the indenter was manually indented into the test specimen to differentiate from frequencies found in the rig. All frequencies from the specimen only were found to be well under 100 Hz.

---

Initial tests, including specimen 837L, were tested at 4 m/s. At the time, even though 4 m/s was above our target of 3 m/s, since the designed drop tower system could easily achieve higher velocities, it was thought to be beneficial to get as high rates of indentation as possible. However, as described in the previous section, high frequency content was found in the data stemming from various dynamic parts of the rig, especially at higher rates. While the data for specimen 837L was reasonably good when filtered, another specimen tested

at higher rates during pilot tests did not turn out nearly as good even when filtered. It was decided to decrease the input velocity back down to 3 m/s to decrease noise.

Expressed in more detail in Chapter 3, it was found that the center thickness of the tissue was the driving factor in the force response of the tissue. While the thickness of each specimen were calculated using ultrasound, the tissue was very deformable and a final center thickness of the tissue while on the rig was desirable. To measure this, with the trigger strips attached to the rig and the tissue, the indenter was lowered very slowly until it triggered the data collection system. The spring plungers on the indenter crosshead were then tightened so that the crosshead could no longer move. Using calipers, the height of the crosshead was measured relative to the base of the indenter rig. Using geometry of the rig via CAD, a parametric formula was created to solve for the tissue height based on the location of the crosshead and the known dimensions of each part on the rig. This thickness is the de facto thickness reported in this thesis and is the one used in further calculations such as the tissue finite element model described later.

### **3.5 Results**

Eleven specimens were successfully tested in the drop tower apparatus. After the trial runs, a few specimens (not included in the eleven) produced unusable data. This was due to some very thick specimens (~70 mm) that failed to compress enough for the magnets to engage the indenter crosshead. The data could still have been used had it not been for the magnets continuing to pull into the tissue after the video had ended. Since the displacement was measured through motion tracking, any displacement of the indenter after the camera had concluded recording would render the data useless because the long term response of the tissue would be unable to be solved for during the inverse FE process. The thick specimens were tested a second time at a higher velocity and were successful in catching the magnets, but it is unknown how this type of indentation damages the soft tissue, so the data was left out of this study.

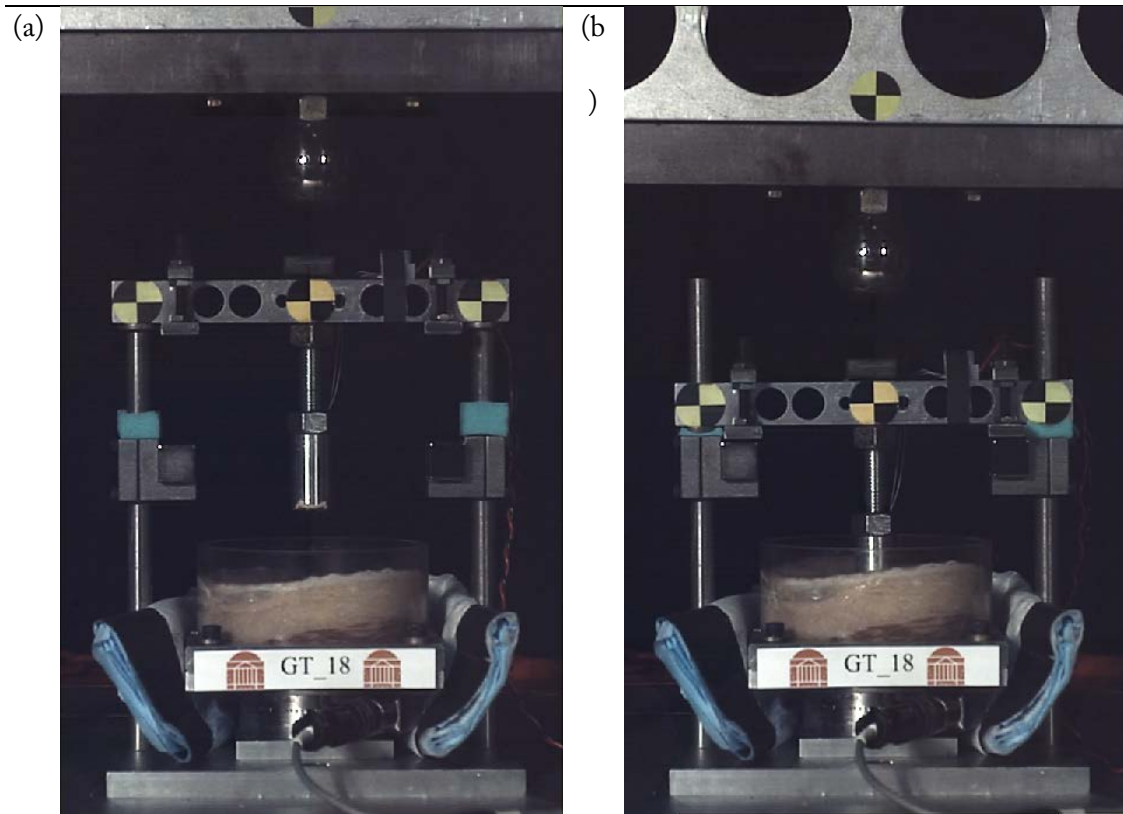


Figure 23. Example of tissue prior to indentation (a) and after indentation (b).

These occurrences were recognized in the data as an increasing force after the end time of the camera, rather than a decreasing force due to relaxation. All other tests were checked for this indicator. In a couple of other tests, it was found in the high-speed video that the magnets tended to pull in the indenter similarly to the case described before; however, these cases were less severe. Most importantly these motions were all captured while the high-speed video was still recording and decayed sufficiently before the recording ended. Therefore, these cases still produced good data, and since the displacement of the indenter along the whole video was recorded, it would still be able to be used in the long-term response during the iFE process.

Table 5. Summary of input conditions and outputs.

Specimen	Input Velocity [m/s]	Total Displacement [mm]	Time to Peak Displacement [ms]	Peak Force [N]	Relaxed Force (50 ms) [N]	Relaxed Force (30 s) [N]
805L	3.1	18.4	8.5	155.7	65.0	11.1
805R	3.1	19.3	9.5	246.9	117.9	10.1
811R	3.1	18.0	8.5	120.6	40.9	36.2
831L	3.1	21.6	8.5	135.9	57.0	21.4
831R	3.0	19.3	8.8	114.2	52.0	23.3
836R	3.0	18.0	8.8	44.5	14.6	11.1
837L	3.9	19.7	6.5	229.4	41.9	37.7
869R	3.6	24.0	9.8	133.5	57.1	20.5
874L	3.0	18.9	9.5	222.5	81.6	4.5
874R	3.1	19.6	9.0	196.8	66.7	19.0
876L	3.1	19.6	9.5	86.8	47.0	19.9
Average	3.18	19.8	8.8	139.6	53.9	17.9
Standard Deviation	0.3	1.7	0.9	63.8	26.0	8.8

Table 5 outlines the input conditions and key output results for the material tests. For specimens tested at 3 m/s, the average input velocity was 3.05 m/s with a standard deviation of 0.08 m/s. Specimen 837L was tested at 3.9 m/s, and 869L was tested at 3.6 m/s. Because of the difficulty the rig had indenting thick specimens, it was decided to indent these at a slightly higher input velocity to ensure that the magnets caught and created a good step-hold.

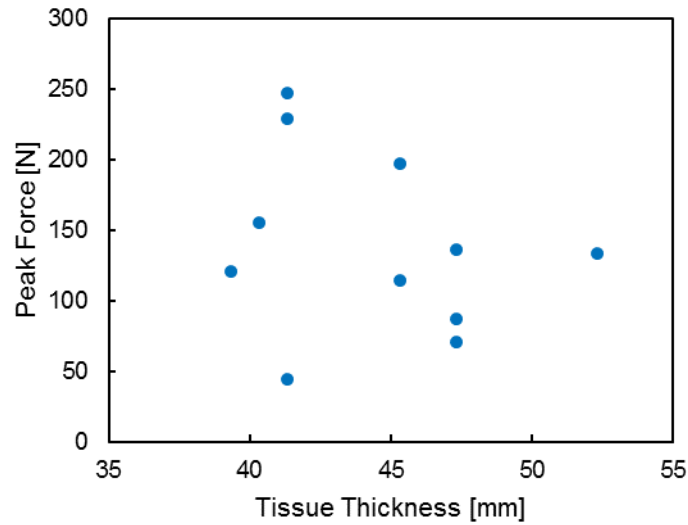


Figure 24. There was a poor relationship between tissue thickness and peak force.

---

The indenter was able to input a nearly perfect linear pulse into the tissue (see Figure 25) and hold the indentation to capture the relaxation of the tissue. The average time of peak displacement was 9.0 ms, and varied based on the thickness of the tissue and the input velocity. The average displacement was 44.4% of the tissue thickness. The force response and different data processing steps for an example specimen can be found in Figure 26. The average peak force was 139.6 N, and despite thicker tissue having deeper indentations, tissue thickness (and therefore indentation thickness) was a bad predictor of peak force (see Figure 24). After 50 ms, the average force was 53.9 N, and 17.9 N after relaxing 30 s. The final recorded force (30 s) was on average 14.2% of the peak force during indentation.

All indentation data can be found in Appendices 9.1—9.3.

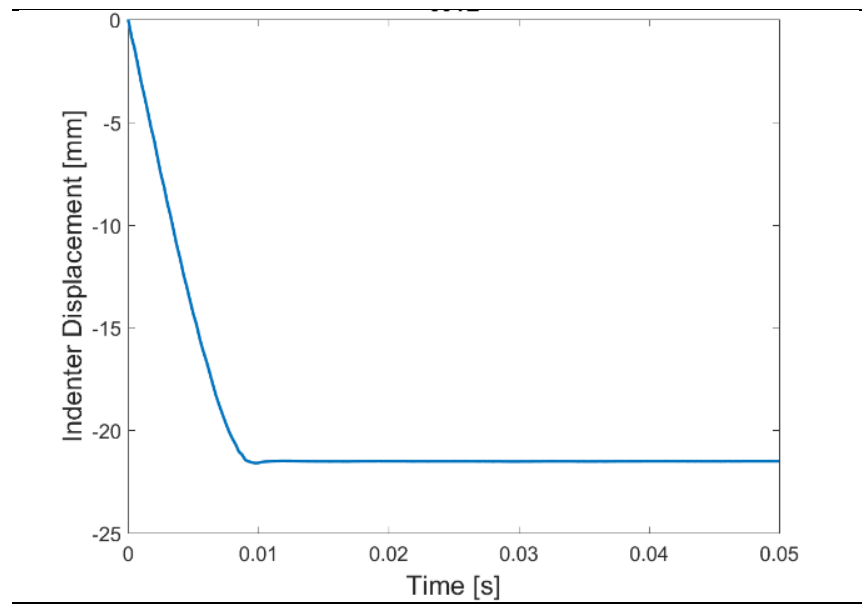


Figure 25. Example input displacement versus time.

---

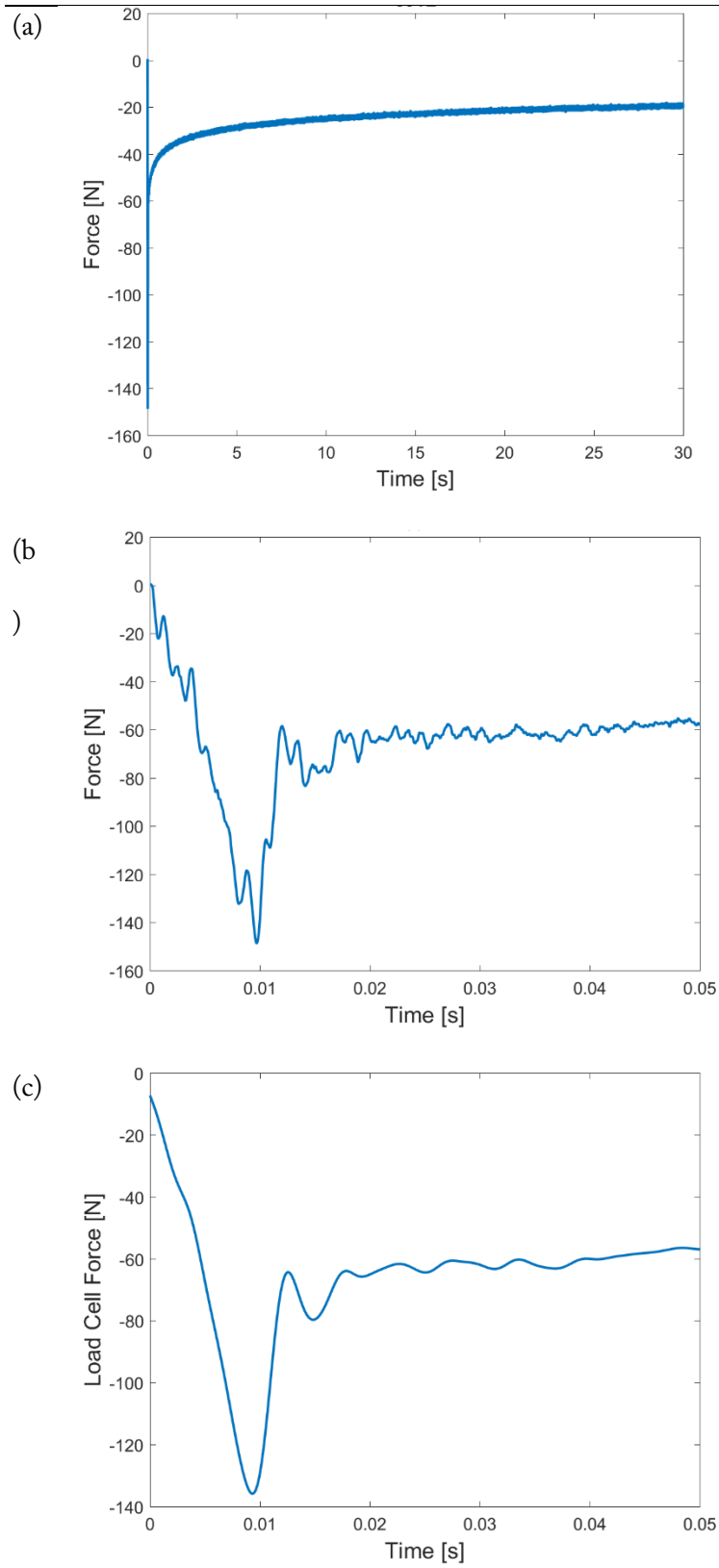


Figure 26. Example force output at 30 s raw (a), 50 ms raw (b), and 50 ms filtered (c) for test 831L.

### 3.6 Conclusion

In this chapter, a custom drop tower apparatus was designed to test gluteal tissue specimens in compression. A sensitivity analysis was performed to determine test parameters that minimized boundary effects. From this, the indenter and tissue radii were chosen. Because this test was intended to at least match the approximate strain rates from component pelvis vertical impact tests, the indenter velocity was chosen through a strain and strain rate analysis of the pelvis tests.

The custom two-stage drop tower system was capable of indenting the tissue specimens at a constant velocity, and through a magnet system, was able to approximate a step-hold environment with very small overshoot of the intended maximum displacement. Eleven specimens were successfully tested in this manner; a few other specimens were not successfully tested because of input velocity limits and were not used in the data set in this chapter. These specimens were unsuccessful because of the difficulty of managing the relationship between noise seen in the load cell from metallic ringing through the rig and the input velocity required to fully indent tissue specimens. It was found that thicker specimens reduced the noise in the system (i.e. they insulated the load cell better); however, they required a higher velocity in order to reach 50% strain and have the magnet system engage. Because of the difficulty in choosing an appropriate input velocity for these specimens, some were successful and others were not.

It was also found that in a couple specimens, the magnets did not fully engage. In these cases, because of the strength of the magnets, after the impact the magnets slowly continued to pull the indenter into the tissue. Because of the limits of storage of high-speed video capture, only a finite amount of time was captured. While the load cell data could continue to capture this increase in force after the impact, if the magnets were still pulling the indenter into the specimen after the high-speed video stopped recording, this data could not be used since the indenter position was captured through the video.



For the data from these eleven specimens to be useful in finite element modeling, a material model based on the data from these specimens is needed.

## 4 Material Modeling

### 4.1 Introduction

Because there is a lack of material testing of gluteal tissue at high rates, there is also a lack of dynamic material models for gluteal tissue. Currently, material models for gluteal tissue used in finite element models for dynamic tests are approximated and are not based on dynamic material tests. For example, the material model used in the GHBM automotive model is a hyperelastic model without viscoelasticity. The stress of the tissue is based on a single stress-strain curve and therefore cannot accurately capture the stress from different impacts that cause different strain-rate loading.

With a dataset of force- and displacement-time history of soft tissue specimens now available, a material model for these specimens is needed. The inverse finite element (iFE) method has been shown to be an effective way to find material parameters for a constitutive model [66,71]. In this method, an FE model is created that simulates the boundary conditions and inputs from experimental testing of a material. The material model constants are then iteratively changed in subsequent simulations until some measured output from the FE simulation matches or reaches some threshold of similarity to that of the experiment. Often, optimization routines are utilized to reduce total computation time to find a solution. The iFE method is particularly useful for experiments that have complex boundary conditions or inputs or for experiments in which stress and strain of the material cannot be easily calculated. In the case of this thesis, an FE model of each tissue specimen discussed in Chapter 3 was created, and material properties were iteratively changed until the output force from the FE model matched that of the experimentation data.

The objectives in this chapter were to first, create a specimen specific finite element model capable of recreating each tissue specimen tested, and second, establish an inverse finite element routine to find material constants for the material model chosen to represent each tissue specimen. Successfully creating a

material model for the gluteal tissue specimens allows for finite element models to accurately model the compression of gluteal tissue in vertical loading. With the gluteal tissue acting as a barrier between the bony pelvis and the vertical impact, accurately modeling the soft tissue is critical.

## 4.2 Finite Element Model

### 4.2.1 Tissue Mesh Design

To assist in creating the material model for the gluteal tissue, a finite element model similar to the model described in Section 3.2.3 was created. The new FE model uses the same radial mesh pattern with hexahedral elements. During the design process of the FE model, tissue material properties from the GHBMC model and from Gabler et al. were used (\*MAT\_SIMPLIFIED\_RUBBER); however, the strain-rate dependent properties were simplified while benchmarking the model. Instead of having a wide range of stress-strain curves for varying strain rates, only a single strain rate table was used. This was important because the strain rate distribution for different levels of mesh sizes were found to be different, and a direction comparison between mesh sizes was needed.

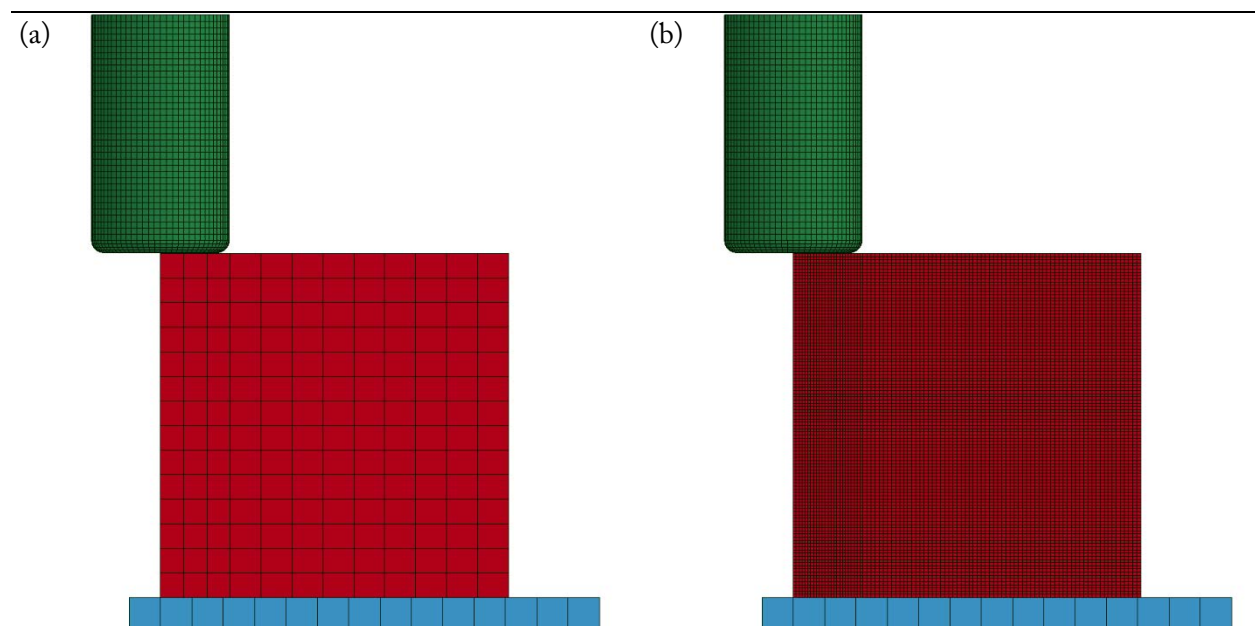



Figure 27. Example of coarsest (a) and finest (b) mesh for the 55 mm thick model.

From the design of the pelvis tissue experimentation, the tissue was set to a radius of 55 mm with the indenter set to a radius of 11 mm. The indenter strikes the tissue at a constant 5 m/s and holds at the prescribed maximum displacement calculated in Section 3.2.3. The plate was modeled as a rigid solid and served as a rigid boundary condition. The model was reduced to a quarter model with planes of symmetry to reduce computational time. The force-time response is recorded from the contact formulation (\*CONTACT\_AUTOMATIC\_SURFACE\_TO\_SURFACE) between the bottom of the tissue and the rigid plate underneath (i.e. the “load cell”).

Table 6. Edge lengths and number of elements in each mesh size of the FE tissue model.

Mesh Size	Approximate Edge Length	Total Number of Elements (30 mm Thickness)	Total Number of Elements (55 mm Thickness)	Total Number of Elements (99 mm Thickness)
Coarse	3.8 mm	352	616	1100
	2.8 mm	1050	1890	3360
	2 mm	2520	4536	8332
	1.4 mm	6930	12600	22680
	1 mm	20160	36288	65856
Fine	0.5 mm	161280	304873	526848

To reduce the computational time needed to run simulations using this FE model, six different mesh sizes were tested (see Figure 27 and Table 6) at minimum, median, and maximum tissue thicknesses. The grid convergence index (GCI) method [96] was used to estimate the exact solution and compare error of each mesh size to the estimated solution. This method is based on Richardson’s extrapolation technique to improve rate of convergence of a sequence [97] and is useful because it does not require an exact solution. The estimated solution,  $f_{exact}$ , can be expressed as:

$$f_{exact} \approx f(h) + Ah^p + H.O.T. \quad \text{Equation 7}$$

$f(h)$  represents the model solution,  $A$  is a constant,  $h$  is a measure of grid spacing,  $p$  is the order of convergence, and  $H.O.T.$  represents the higher order terms. If the meshes being used are refined enough, (i.e. the meshes are converging and not changing rapidly), then the higher order terms can be neglected [98], and the exact solution can be written as:

$$f_{exact} \approx f_1 + \frac{f_1 - f_2}{r^p - 1} \quad \text{Equation 8}$$

$r$  represents the refinement ratio, and  $f_1$  is the finest grid solution with increasing numeric subscripts corresponding to coarser mesh solutions.  $r$  and  $p$  can be defined as:

$$r = \frac{h_3}{h_2} = \frac{h_2}{h_1} \quad \text{Equation 9}$$

$$p = \frac{\ln(\frac{f_3 - f_2}{f_2 - f_1})}{\ln(r)} \quad \text{Equation 10}$$

Peak forces and errors from the different mesh sizes relative to  $f_{exact}$  were calculated for each mesh size at 30 mm, 55 mm, and 99 mm thicknesses. The 2 mm mesh was chosen, which had an error of 4.1% and 26.0% error for the 55 mm and 30 mm thicknesses, respectively. The 99 mm thickness samples failed to converge for the GCI study, but considering the thicker samples produced less error and few actual tissue samples were measured thicker than 55 mm, the lack of comparison for the 99 mm thick samples was insignificant. Figure 28 shows example force-time curves for the 55 mm samples, as well as plots of peak forces and absolute error by thickness and element size.

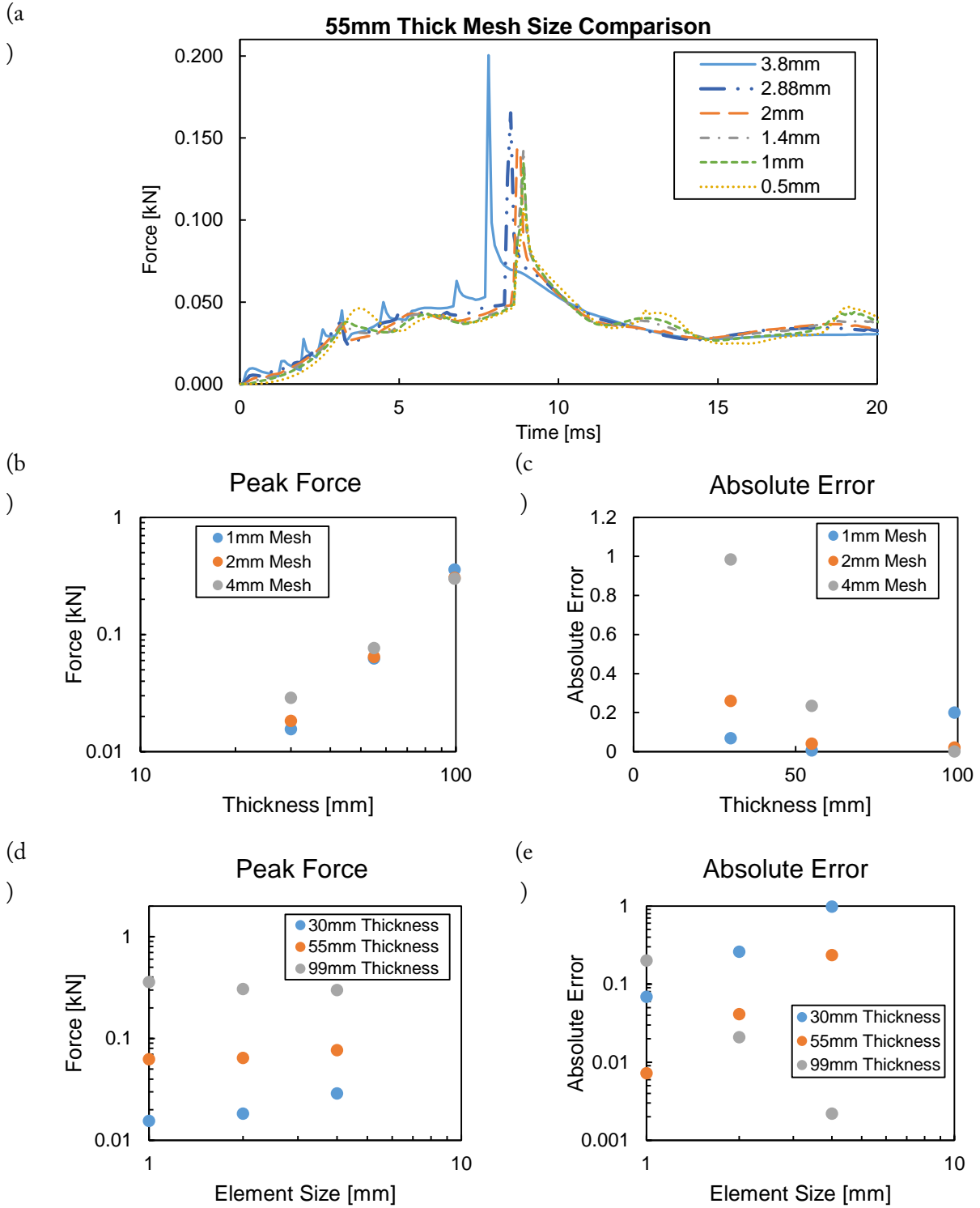


Figure 28. Example comparison of mesh size on force-time response for 55 mm sample. Peak force and absolute error by thickness (b–c) and by element size (d–e).

#### 4.2.2 Shape Effects

For the inverse finite element method shown in the next chapter (Chapter 4.3), each tissue specimen requires its own model based on the height of the specimen. While the top layer (skin) of some specimens were very flat and relatively uniform, others were not. Because of this and because of the difficulty in preserving shape of soft tissue, it was important to analyze whether the specimen specific FE model could have an idealized flat top and how much error would be involved. From the previous analysis in Section 3.2.1, the ratio of the tissue to the indenter was chosen to avoid boundary effects along the circumferential surface. Therefore, the FE model will be relatively insensitive to irregularities on the circumferential surface after cutting the tissue; however, this does not account for any surface irregularities since the models used to test this were all flat. To preserve the ratio of muscle and fat in each specimen as well as to preserve the layer of skin, tissue was not removed during specimen preparation to flatten them, and any irregularities were kept. To test for effects of irregular top surfaces of the specimens, a series of FE models were created with a curvature on the top surface and were compared to a corresponding flat model. To test the most deviance from a flat specimen (i.e. the largest volumetric difference), a curved model was created that tapered continuously from the point of indentation to about 20–25% of the thickness (see Figure 29).

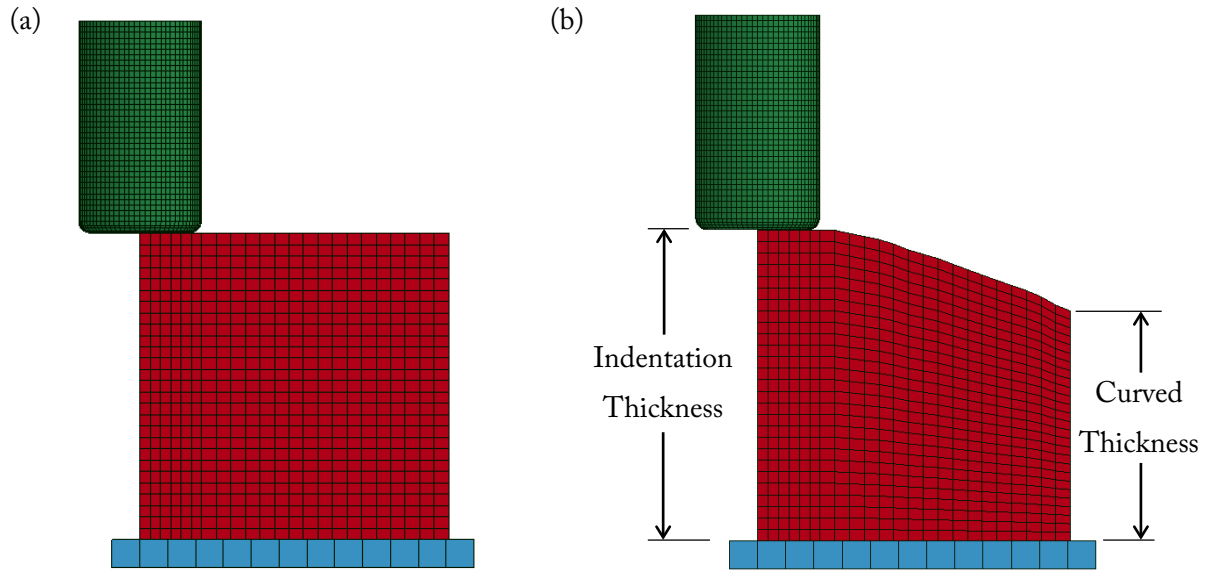


Figure 29. Comparison of the flat (a) and curved (b) FE models. Both models have equal thickness at the indentation point.

To investigate this, both the flat and curved models were subjected to various displacements with different thicknesses. Example results can be found in Figure 30. The results show that the force-time response was not influenced by difference in volume as long as the indentation thickness between the two models were the same. The thickness of the specimen and the point of indentation clearly dominates the force response; therefore, there are very small amounts of error when approximating a specimen as flat, despite surface irregularities. All heights of specimens reported were accordingly measured at the center where each specimen would be indented.



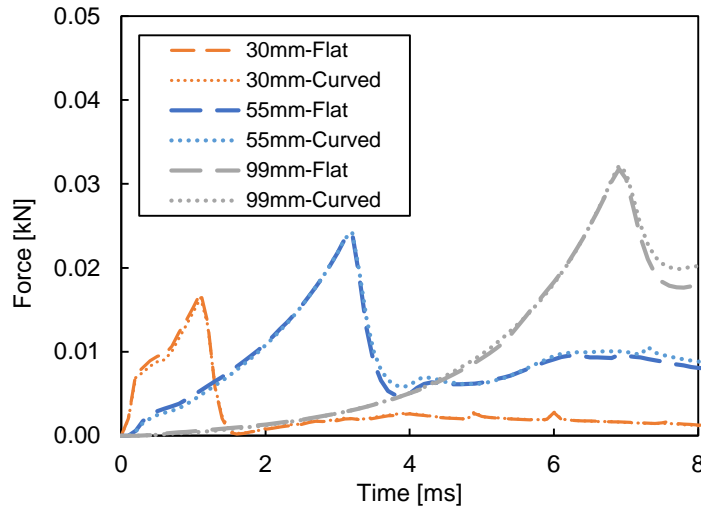


Figure 30. Comparisons of flat and curved models at varying thicknesses.

#### 4.2.3 Constitutive Model

The tissue was chosen to be modeled using an Ogden rubber model [99]. This was done for several reasons. First, the Ogden rubber model is a relatively simple model. Since the material constants were going to be iteratively changed over perhaps hundreds of simulations for each specific model during the inverse finite element model process, small amounts of added computation time could be substantial when summed across all simulations. Second, it is able to capture viscoelastic effects. Tissue is well reported to exhibit viscoelastic properties, and being able to capture these effects in the finite element model is critical to capturing the response during dynamic compression. Third, the Ogden rubber model is a widely used constitutive model whose constants can easily be reported in literature and adapted to FE software.

The Ogden model (Equation 11) is a hyperelastic model in which the nonlinear stress-strain relationship is derived using a strain energy density function,  $W$ . The strain energy density is expressed as a function of its principal stretches,  $\lambda_i$ , shear modulus,  $\mu$ , with  $n$  and  $\alpha$  representing material constants. In the LS-DYNA Ogden formulation, a hydrostatic work term,  $K$ , is included in the strain energy function to model

the rubber as an unconstrained material. The hydrostatic work term is a function of the relative volume,  $J$ , and  $K$  is the bulk modulus. The asterisk,  $*$ , denotes elimination of volumetric effects.

$$W^* = \sum_{i=1}^3 \sum_{j=1}^n \frac{\mu_j}{\alpha_j} (\lambda_i^{*\alpha_j} - 1) + K(J - 1 - \ln J) \quad \text{Equation 11}$$

Optional rate effects can be enabled in LS-DYNA through a linear viscoelasticity convolution integral (Equation 12). The stress,  $\sigma$ , is expressed using a relaxation function,  $g$ , with  $\sigma^E$  representing the instantaneous stress. The relaxation function (Equation 13) is represented as a Prony series, where  $G_i$  are the shear relaxation modulus, and  $\beta_i$  are the decay constants.

$$\sigma_{ij} = \int_0^t g_{ijkl}(t - \tau) \frac{\partial \sigma_{kl}^E}{\partial \tau} d\tau \quad \text{Equation 12}$$

$$g(t) = \sum_{i=1}^n G_i e^{-\beta_i t} \quad \text{Equation 13}$$

If given enough time to relax after being compressed, the final stress of the material is only a function of  $\mu$  and  $\alpha$ ; that is, the viscoelastic effects will have completely relaxed, and the final stress state would theoretically be equal to the same input conditions without viscoelasticity included in the material model.

#### 4.2.4 Full Design

The indenter was meshed using Hypermesh and exactly matches the indenter geometry machined for the tissue testing. It was modeled as a rigid material and was constrained to z-axis movement. The indenter's movement is prescribed by the displacement collected from the motion capture analysis. \*CONTACT\_AUTOMATIC\_SURFACE\_TO\_SURFACE was used as the contact between the shell skin part and the indenter.

Even though the gluteal tissue was modeled as homogenous, a thin shell layer was created on the top layer of the tissue where the skin would have been modeled. This was done to give the finite element model more

stability. The skin was modeled using \*MAT\_NULL so that the skin shell did not affect the response of the tissue. Because of the high velocity impact and large amounts of deformation, the shell thickness on the skin layer was adjusted based on whether the tissue material model had viscoelasticity included or not. The change in viscoelasticity in the Ogden model formulation often changed the stability of the tissue during large deformation. Increasing the shell thickness from 0.1 mm to 1.0 mm increased the stability when viscoelasticity was turned off. To offset the increase of the functioning thickness of the tissue model by 1 mm, the indenter was offset away from the tissue by 1 mm in these cases to keep the same indentation depth.

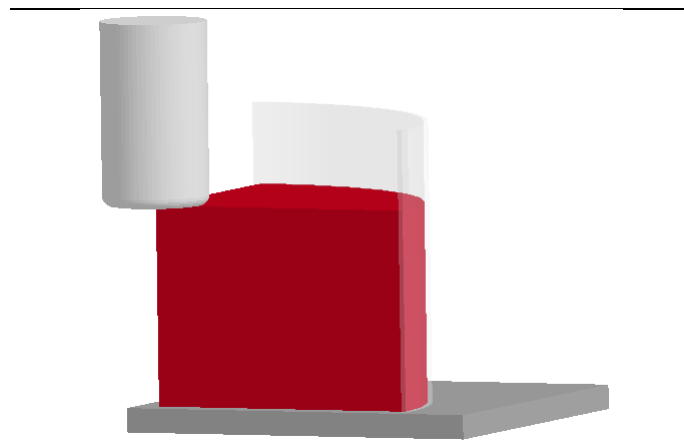
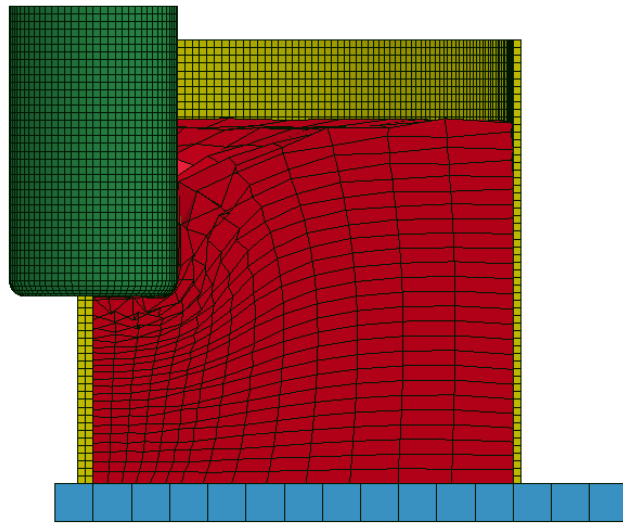


Figure 31. View of final design of the tissue indentation FE model.

The tube surrounding the tissue has the same inner diameter as the tube described in the material testing. The tube was also modeled as a rigid material and was fully constrained. Before implementing the tube as a rigid part, three methods of constraining the tissue were tested: \*RIGIDWALL, nodal constraints, and rigid part. The \*RIGIDWALL formulation is a simplified contact method that reduces nodal velocities from a deformable body to zero and prevents any nodal penetration. Because of this, this method also lacks any friction between a deformable body and the \*RIGIDWALL. While simple and computationally quick, this method was found to be unrealistic in this situation because of the relatively high amounts of friction

and suction between the tissue and the acrylic tube in the actual experimental tests. Conversely, using nodal constraints overly constrained the nodes and prevented the tissue part—especially the top surface of the tissue—from capturing the correct deformation of the tissue around the indenter. Modeling the tube as a rigid part and using \*CONTACT\_AUTOMATIC\_SURFACE\_TO\_SURFACE between the two allowed for the most flexibility in selecting more realistic friction coefficients and ultimately gave the most realistic response of the three.



---

Figure 32. Example of hourglassing and overall general instability of the tissue model.

---

Because of the large deformation of the tissue, hourglassing and high hourglass energy were common issues in the development of the tissue model (see Figure 52). As mentioned previously, whether viscoelasticity was included in the material model also changed the stability of the model, including hourglassing effects. Dozens of combinations of hourglass forms, coefficients, and element forms for the skin shell model were tested to find the best combination to decrease hourglassing, while keeping the hourglass energy to internal energy ratio as small as possible. In the end, a different combination was used based on whether the model was running with viscoelasticity or not.

## 4.3 Inverse Finite Element Method

### 4.3.1 Insight from the Vertical Impact Pelvis FE Model

Many parts of this thesis were done, at least partially, in tandem. Notable is the VIP FE model described in full in Section 5.2 and referenced in Section 3.2. An early version of the VIP model existed during the process of creating the tissue FE model and the iFE process, and therefore could be used as reference. While developing the material model for the tissue based on the experimental results, the model was periodically inserted into the pelvis FE model to check for stability and performance.

Because tissue is viscoelastic and strain rate dependent, and due to the relatively high rate loading of the tissue, an initial thought was that the short-term response of the tissue compression tests would dominate the overall response and the long-term response that captures relaxation would be negligible. However, because the component pelvises in the experimental pelvis tests (see Section 2.6) were loaded while precompressed via constant force springs to simulate the upper body weight, the VIP model needed to be loaded likewise. This required around 500 ms of settling to reach equilibrium before the pelvis could be impacted. After inserting an example of tissue model fitted only to the short term response, it was clear that the long-term relaxation of the tissue was crucial to the overall response. The overall compression of the tissue compared with the GHBMC stock material (hyperelastic model with no viscoelasticity) was significantly less and resulted in a lower axial force (Figure 52). This showed that while the short-term constants of the material model were indeed important, the long-term relaxation of the model could not be ignored because of its large influence on the force response.

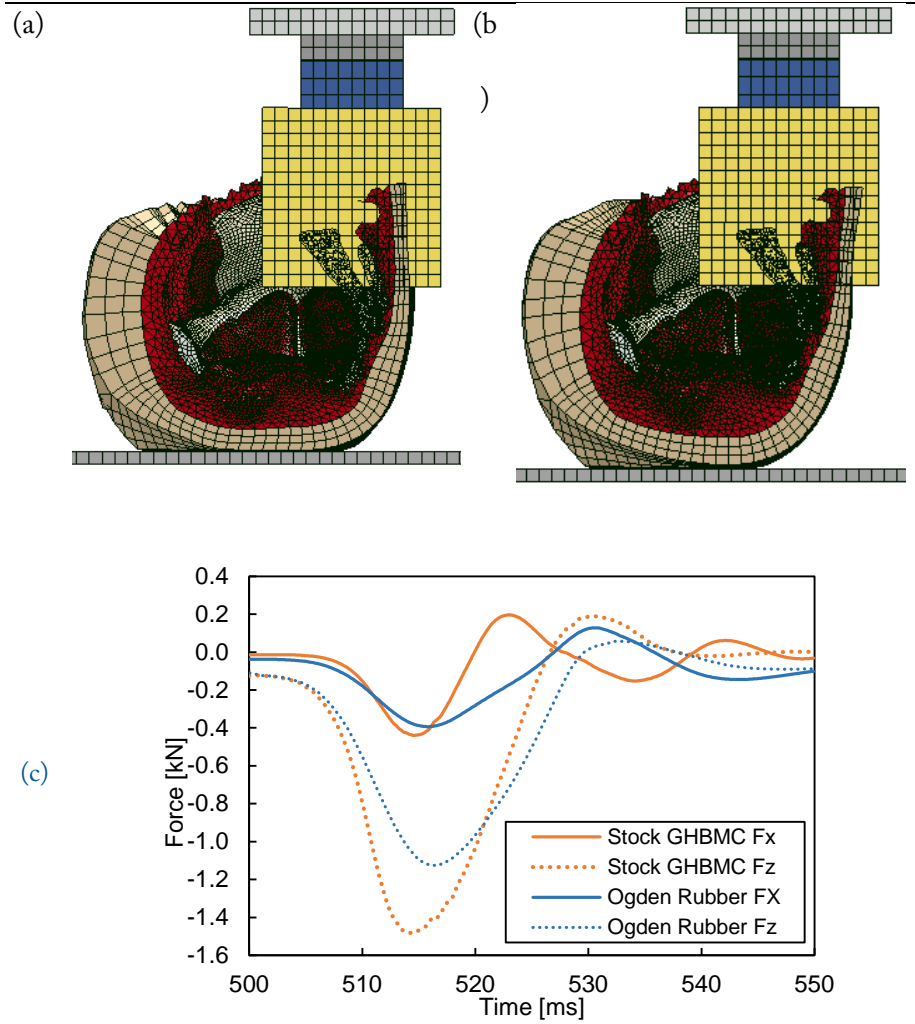


Figure 33. Tissue compression comparison with the GHBM stock tissue material (a) and an example short-term fitted Ogden (b). Axial (Fz) and shear (Fx) forces compared in (c).

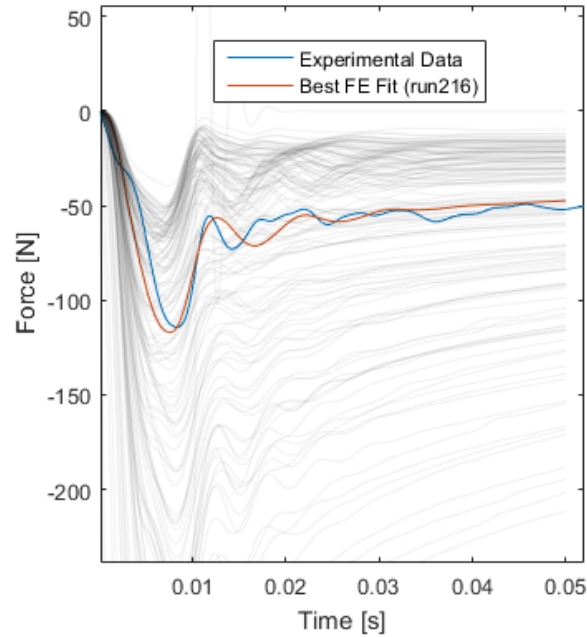
#### 4.3.2 Design

The iFE process was set up using MATLAB (Mathworks, Natick, MA) and LS-DYNA. The FE model files were set up parametrically so that the tissue height and the material constants of the tissue could be modified systematically. A series of MATLAB scripts were written that created the FE model file of the tissue based on the measured height of the tissue and could iteratively write new material constants in the FE file.

With a framework in place, material constants needed to be determined. In order to ascertain these, a simple optimization routine was created. This method combined Monte Carlo sampling with minimizing of sum-squared-error (SSE) (Figure 52). First, a number  $n$  of simulations with randomly generated material constants were executed, and then the SSE was calculated for each simulation with respect to the experimental data. The material constants of the  $n/2$  simulations with the lowest SSE were averaged and the standard deviation (SD) was calculated. The next  $n$  simulations were run with new bounds for the randomly generated material constants equal to  $\text{cavg} \pm c\text{SD}$ , where  $c$  is any material constant. This process would continuously run until the model response converged to the experimental results. Convergence was declared once the average SSE of the most recent five simulations were within 5% error of the simulation with the lowest SSE (i.e. the minimum SSE is not significantly decreasing with addition simulations).

$$SSE = \sum_{i=1}^n (y_i - f(x_i))^2$$

Equation 14




---

Figure 34. Example plot of simulations from Monte Carlo approach.

---

While this method proved to be effective, it occasionally did not converge to the best fit. The routine could converge to a false minimum if the variation in the  $n$  simulation did not sample in the range of the actual response. This is because after  $n$  simulations, the best  $n/2$  were chosen to set the new bounds. If the  $n$  simulations did not sample in the actual range, the optimization could minimize to a false minimum. In these cases, the model was usually not far off from the experimental data. With an approximate solution found, tight bounds could be created, and a new set of Monte Carlo simulations would eventually find a better fit. This usually did not take long, and a better solution would be found.

In a few cases, it was found that despite a sufficient amount of sampling, the FE response could not entirely capture the experimental response. This was evident from the FE model being able to capture the initial spike of force, but not the 50 ms relaxed force or vice versa (see Figure 52). Because of how the iFE process was developed, the best fit model would converge to a response in between the two; that is, that the peak FE value would be less than that of the experimental peak, and the 50 ms relaxed force of the FE model would be higher than that of the experimental. While this was probably sufficient as is, in the end it was the loading behavior—the peak force—and not the unloading behavior—the 50 ms relaxed force—that was desirable for the model to capture. In cases like these, a slightly modified iFE process was used that instead of finding a best fit by minimizing SSE, the best fit was determined by minimizing error between the peak force levels. In most cases the FE model was able to capture both, but in cases in which it could not, this modified approach was used.



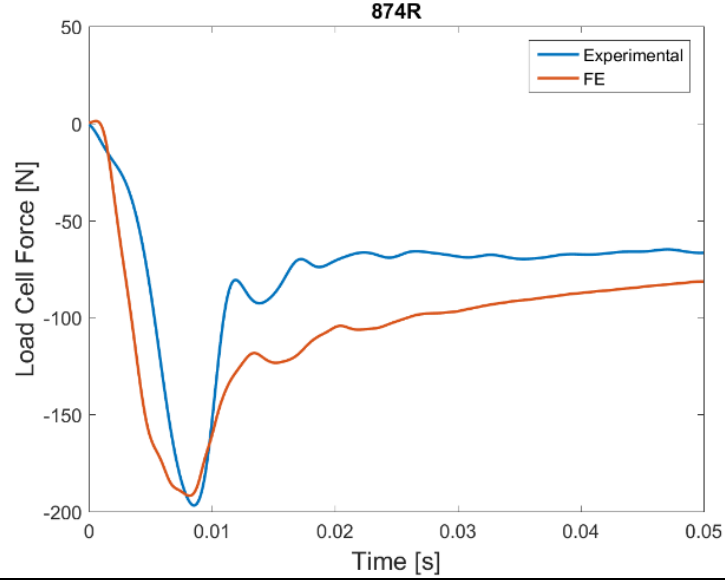


Figure 35. The FE material model was unable to capture both the peak load and the 50 ms relaxed force.

As stated in the previous section, both the short- and long-term responses were important to accurately model the pelvis component FE model. However, this was problematic since the experimental tests ran for 30 seconds, and to run tens or even hundreds of models during the iFE process for a single specimen with this run time was not feasible. To approach this problem, the iFE process was split into two parts. The first part was to capture the long-term, or steady-state response; that is, to capture the final state of the tissue at 30 s of experimental data. The second part was to capture the short-term, or instantaneous response.

To reduce the complexity in the model,  $\alpha$  was chosen to be constant across all models. The initial value of  $\alpha$  started as the value found in hyperplastic models of other rubber materials and was later adjusted to a value of 4 for stability once the magnitude of  $\mu$  was determined. Likewise, the time constants,  $\beta_i$ , were also kept constant throughout all the tissue models. With a knowledge of the indentation event timing and window of interest in the data, the time constants were chosen as 1.0, 0.1, and 0.01. Adding additional time constants to either a lower or higher decade did not increase the performance of the model. This left  $\mu$  to be solved by the steady-state simulation and  $G_i$  to be solved by the instantaneous simulation.

For the steady-state simulation, viscoelasticity was removed from the Ogden material model of the tissue to converge to the steady-state response quicker. This left the Ogden as only a function of  $\mu$  and  $\alpha$ . This model solves very quickly, and while the iFE optimization routine could be used here to solve for  $\mu$ , it was faster to optimize the constants “by hand” because of the linear relationship  $\mu$  and  $\alpha$  have with the material response (see Equation 10 in Section 4.2.3).

For the instantaneous simulation viscoelasticity was returned to the tissue model. The short-term response was determined to be the first 50 ms of data, because only 50 ms of run time was needed to capture the area of interest in the component pelvis model.  $G_i$  was then solved for each specimen using the iFE optimization routine described. After the material constants were solved for each specimen, a mean model was created and compared to each individual fit.

## 4.4 Results

Table 7 shows the full results from the iFE process for each specimen. The average shear modulus,  $\mu$ , was 2.8E-6 with a standard deviation of 1.3E-6. The shear relaxation moduli,  $G_i$ , had an average values of 0.61, 0.18, and 0.15, respectively. There was less deviation in the shear relaxation moduli than in the shear modulus.

Table 7. Material constants solved from the iFE process

Specimen	$\alpha$	$\mu$ [GPa]	$G_1$ [GPa]	$G_2$ [GPa ]	$G_3$ [GPa ]	$\beta_1$ [ms- 1]	$\beta_2$ [ms- 1]	$\beta_3$ [ms- 1]
805L	4.0	3.7E- 6	0.63	0.17	0.14	1.0	0.1	0.01
805R	4.0	5.6E- 6	0.62	0.18	0.15	1.0	0.1	0.01
811R	4.0	1.9E- 6	0.67	0.15	0.14	1.0	0.1	0.01
831L	4.0	2.8E- 6	0.61	0.17	0.16	1.0	0.1	0.01
831R	4.0	4.0E- 6	0.54	0.20	0.15	1.0	0.1	0.01
836R	4.0	8.0E- 7	0.62	0.19	0.14	1.0	0.1	0.01
837L	4.0	1.7E- 6	0.67	0.19	0.13	1.0	0.1	0.01
869L	4.0	1.6E- 6	0.62	0.18	0.15	1.0	0.1	0.01
869R	4.0	2.6E- 6	0.59	0.18	0.17	1.0	0.1	0.01

874R	4.0	2.8E-6	0.66	0.16	0.15	1.0	0.1	0.01
876L	4.0	3.3E-6	0.53	0.20	0.15	1.0	0.1	0.01
<hr/>								
Average		2.8E-6	0.61	0.18	0.15			
Standard Deviation		1.3E-6	0.05	0.01	0.01			
<hr/>								

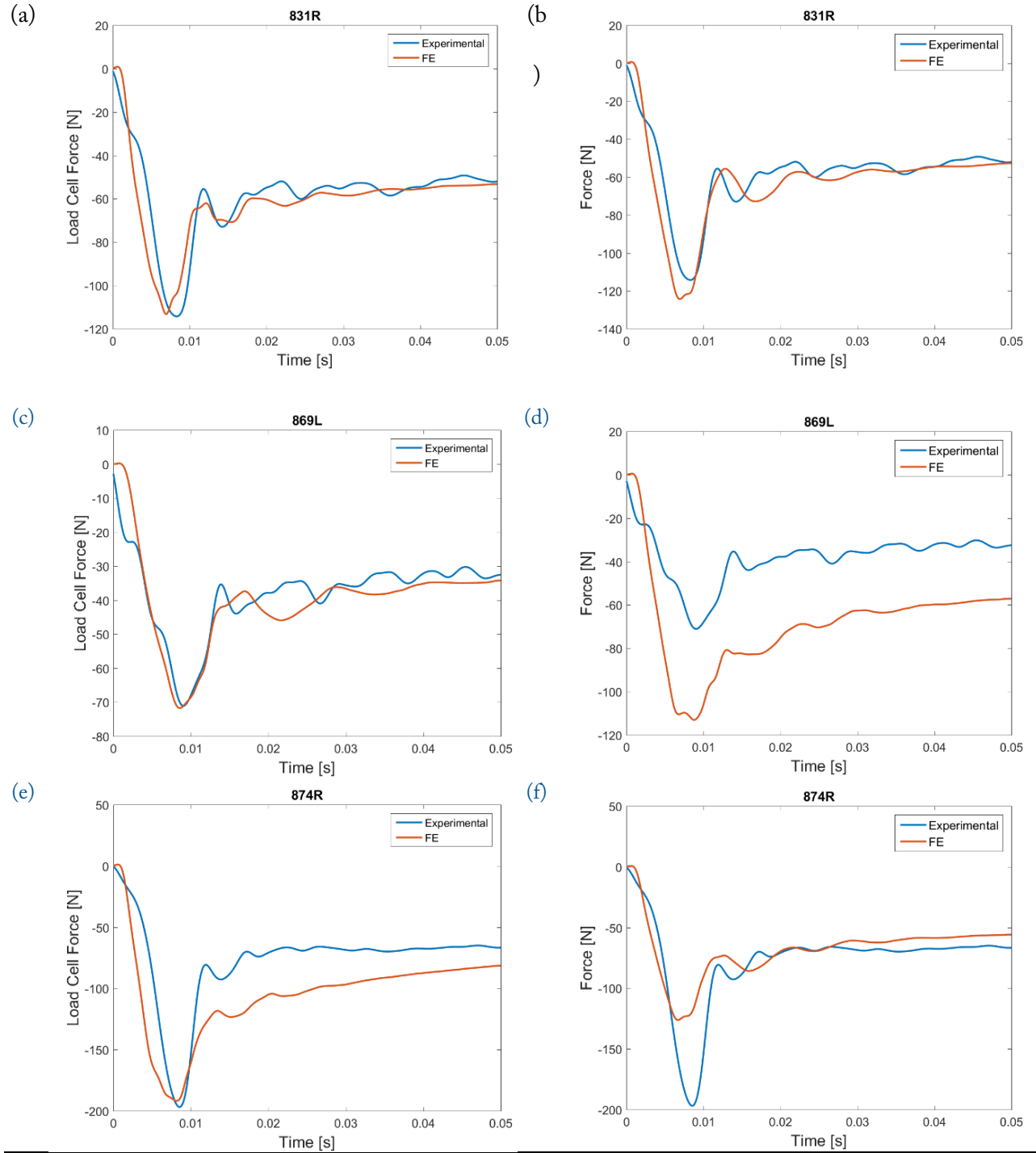


Figure 36. Various examples of how individual fits (a, c, e) compare to their corresponding average model (b, d, f).

These mean values were used to create a mean model. Each model was run a second time with the mean values instead of the individual fit values. When the individual and mean models for each specimen were compared, each specimen fell into three categories. The first category includes specimens in which both the

individual FE model (Figure 52a) and average FE model (Figure 52b) matched the experimental data well. It was natural to think that the specimens that fell into this category would have material constants close to the average values, but that was not always the case. Specimen 831R, for example, had three of the four solved material constants roughly one standard deviation away from the average and had a better fit than specimen 869R, which had material constants closer to the average.

The second category includes specimens in which the individual FE model (Figure 52c) compared well to the experimental data, but the average FE model (Figure 52d) compared less well. Lastly, the third category includes specimens in which both the individual FE model (Figure 52e) and average FE model (Figure 52f) compared less well to the experimental data.

However, this is a very subjective way to compare the two models, especially when considering that some models were tweaked to match peak force values, rather than the best fit for the whole 50 ms time history. To further this analysis, CORA was used to compare the curves [100]. CORA, or CORrelation Analysis, is an objective method to rate how well a simulation response compares to experimental responses. Two overall ratings are given: a corridor rating and a correlation rating (see Figure 37). The correlation rating itself is made of three different metrics: phase, size, and slope. Both the corridor and correlation ratings can be weighted to influence the importance of one rating over another. Likewise, phase, size, and shape, are also weighted to influence the correlation rating. Since there was only one experimental test per specimen, the corridor rating was not used, and the phase, size, and shape weights were set to equal weights.

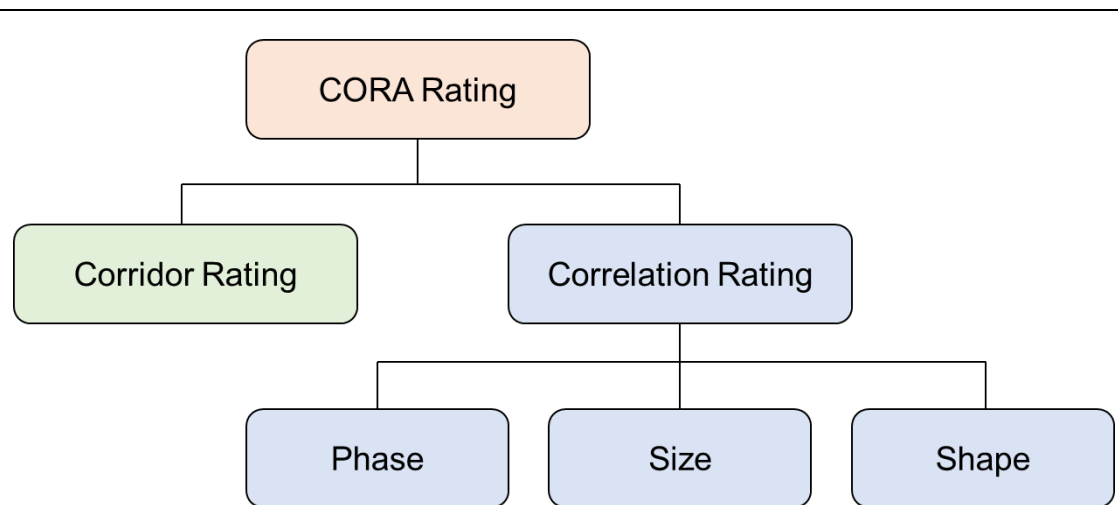


Figure 37. CORA method of comparing simulation and experimental responses.

Table 8 shows the CORA scores for each specimen. Because the peak was given preferential fit in some of the FE models, it was decided to compare only the curve up to the peak load. The CORA method requires data sets of equal length, so the time window was the time average time of peak load for both the individual and average model.

Table 8. CORA scores for each specimen.

Specimen	Individual Model				Average Model			
	Phase	Size	Slope	Total	Phase	Size	Slope	Total
805L	1.00	0.64	0.99	0.88	1.00	0.830	0.996	0.942
	0	6	4	0	0			
805R	1.00	0.65	0.98	0.87	1.00	0.544	0.992	0.845
	0	7	1	9	0			
811R	1.00	0.90	0.99	0.96	1.00	0.691	0.993	0.895
	0	1	6	6	0			
831L	1.00	0.57	0.99	0.85	1.00	0.554	0.993	0.849
	0	8	3	7	0			
831R	1.00	0.63	0.99	0.87	1.00	0.599	0.994	0.864
	0	9	1	7	0			
836R	1.00	0.73	0.98	0.90	1.00	0.155	0.982	0.712
	0	0	4	5	0			
837L	1.00	0.74	0.99	0.91	1.00	0.779	0.997	0.926
	0	8	6	5	0			
869L	1.00	0.94	0.98	0.97	1.00	0.301	0.989	0.763
	0	5	8	8	0			
869R	1.00	0.92	0.99	0.97	1.00	0.718	0.993	0.904
	0	5	3	3	0			
874R	1.00	0.57	0.98	0.85	1.00	0.911	0.988	0.966
	0	3	0	1	0			
876L	1.00	0.98	0.99	0.99	1.00	0.523	0.992	0.838
	0	3	4	2	0			

As expected, in most cases, the average model had a lower CORA score than its individual model counterpart. However, there were a few cases in which the average model had a higher CORA rating than its corresponding individual model. In cases like specimen 874R (see Figure 52a), the FE model was able to match the peak load of the experimental model, but because the slope at different points leading up to the peak were different, it could have a worse CORA score than one that did not match the peak force as



well. Figure 38b shows another simulation in which the FE simulation “split” the experimental curve much differently, and could have a better CORA score even though both examples matched peak force well.

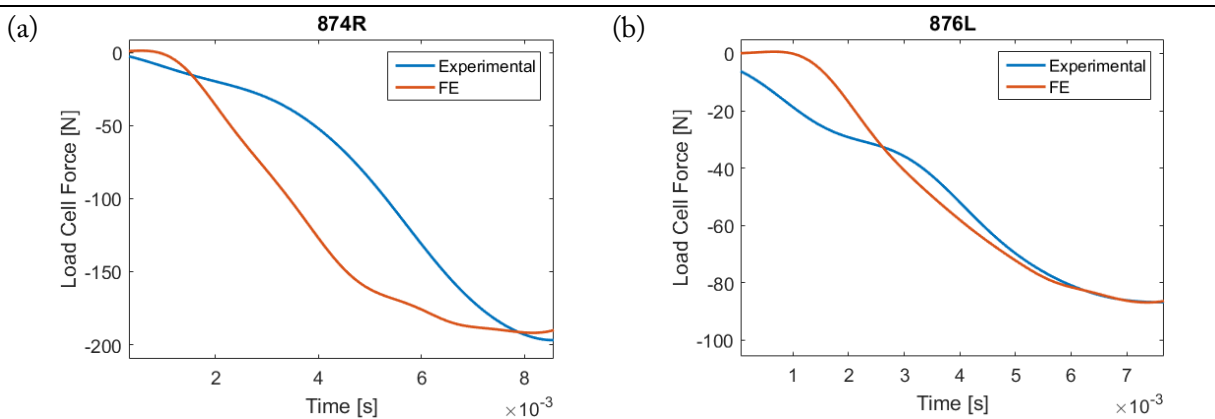


Figure 38. Differences in slopes, not just the peak values, can affect the CORA rating.

The reason that the slopes between the FE and experimental data do not always match is likely explained by the reality of experimental testing versus the idealization of FE modeling. The FE model assumes that the tissue is completely homogeneous, that is, that the tissue is composed of a single uniform material, rather than layers of skin, fat, and muscle, in which each type of tissue can have variation. Fat is less dense than muscle and would resist less as the impactor indents through the initial layers of fat before engaging more muscle over time. The experimental curve can be seen in most specimens lagging behind the FE model until they more or less meet at the peak force. However, this could also be an effect of filtering. Although the filter was shown to not have significant effects on the overall signal, it is possible on a smaller scale—such as the loading time in the first 10 ms—that the signal affected the shape and slope of the curve that it looks significantly different from the FE model. Overall, however, the average model is still able to reasonably represent the different tissues tested.

## 4.5 Conclusion

In this chapter, specimen specific FE models were created for each tissue specimen tested in Chapter 3. The displacement of the indenter from each test was used as the input condition to the FE model. Boundary conditions between the indenter, surrounding tube, and load cell were also made to match those from the experiments. An inverse finite element process was established to solve for the material properties of the Ogden model for each specimen. An optimization routine was implemented into the iFE process to decrease time needed to find the material constants.

The iFE process was split into two parts. The first portion was to capture the shear modulus of the material mode. Since the shear modulus was only as function of the completely relaxed tissue, viscoelasticity was not used in the model, and the objective was for the FE simulation output force to match that of the fully relaxed force of the experimental tissue at 30 seconds after indentation. The second part was to determine the short-term response through solving for the shear relaxation moduli. The model in this case included viscoelasticity, and took much longer to solve, even with the end time only being 50 ms. The total time for each specimen to converge to a solution was approximately 6 hours.

While most of the specimens were able to capture both the peak force spike and the 50 ms relaxation, some were unable to capture both. In these cases, because the optimization routine was minimizing the sum-squared error over the whole 50 ms run time of the simulation, the converged solution under-predicted the peak force and over-predicted the tissue relaxation. Because the material model is intended to be used in dynamic loading scenarios, capturing the correct loading (i.e. the peak force) of the tissue is much more important than capturing the relaxation of the tissue. In these cases, a new optimization iFE routine was run, but this time instead of the SSE calculated over the entire run time, only the error between the peak force of the experiment and FE model was used as the threshold metric.

An aggregate model was created by taking the average values of each material constant from the eleven models. Through a CORA analysis, it was found that the aggregate model as a whole still performed well in modeling the experimental results. With a dynamic material model for gluteal tissue now created, it can be used in finite element models for vertical impact scenarios.

## 5 Application to Component Pelvis Finite Element Model

### 5.1 Introduction

As mentioned previously, current pelvis FE models do not use material models based on dynamic gluteal tissue experiments. Instead, they use approximations that typically are sufficient for their use. However, using these models, such as automotive FE models, in high-rate vertical impact scenarios will not have accurate results. To correctly model high-rate vertical loading, new FE pelvis models need to be created evaluated against appropriate experimental data.

There are three objectives outlined in this chapter. First, a component pelvis FE model named the Vertical Impact Pelvis (VIP) model is created, and is evaluated against experimental UBB tests outlined in Chapter 2.6. The model is based on the GHBMCM pelvis model and modified to match input and boundary conditions taken from experimental data. The pelvis material properties were updated to include the new material model found in Chapter 4. Second, different rate impacts are applied to the model, and analysis techniques are created to analyze how the response of the tissue changes in varying loading rate scenarios. Third, a sensitivity study is performed to determine if other material properties have an effect on the load path through the pelvis.

The purpose of this FE model is to accurately model the UBB pelvis experiments outlined in Chapter 2.6 and use it to understand the load path through the pelvis. Beyond the research found in this thesis, the ultimate purpose of this pelvis model is to accurately predict injuries from high-rate vertical impacts from UBB scenarios. With this capability, this model will be an effective tool to test different counter-measures capable of protecting soldiers from injuries.

## 5.2 Vertical Impact Pelvis Model

### 5.2.1 Design

The VIP FE model started with the GHBMC full body model (v4.4) (Figure 39a). All modeling and simulations were performed using LS-DYNA, and Hypermesh was used for remeshing. Body regions from the GHBMC model were systemically removed until the pelvis was completely isolated from the whole body model (Figure 39b). To better represent the specimens used in the UBB experimental tests, large portions of the distal thigh tissue were removed and the most superior tissue elements were trimmed down to be level with the iliac crest. Both the hexahedral and tetrahedral layers of outer pelvis tissue were updated with the new tissue properties found in Chapter 3.6, with the average tissue properties representing the nominal model. In addition, the skin model was changed to \*MAT\_NULL to match the formulation used in the tissue model. The contents of the pelvic bowl were removed, and the added gel mass from the experiments was simulated using \*ELEMENT\_MASS\_NODE\_SET. While the gel mass was secured to the PMHS pelvis through self-adhesive wrap, there was no way to completely fix it to the pelvis. Because of this, the total mass of the \*ELEMENT\_MASS\_NODE\_SET was set to approximately half of the average gel mass from the experiments, 0.375 kg, to create an effective mass. The model was then halved down the sagittal plane to reduce computation time, with a plane of symmetry down the cut boundary (Figure 39c).

The mass of the FE pelvis was 8.9 kg before halving, which was close to the average PMHS pelvis mass of 10.0 kg. While the GHBMC model used was based off the 50th percentile male, the PMHS used in the experimental testing had an average height of 180 cm and an average BMI of 29.5 kg/m<sup>2</sup>, both higher than the 50th percentile male, which could help explain the 1 kg difference between the model and the PMHS.

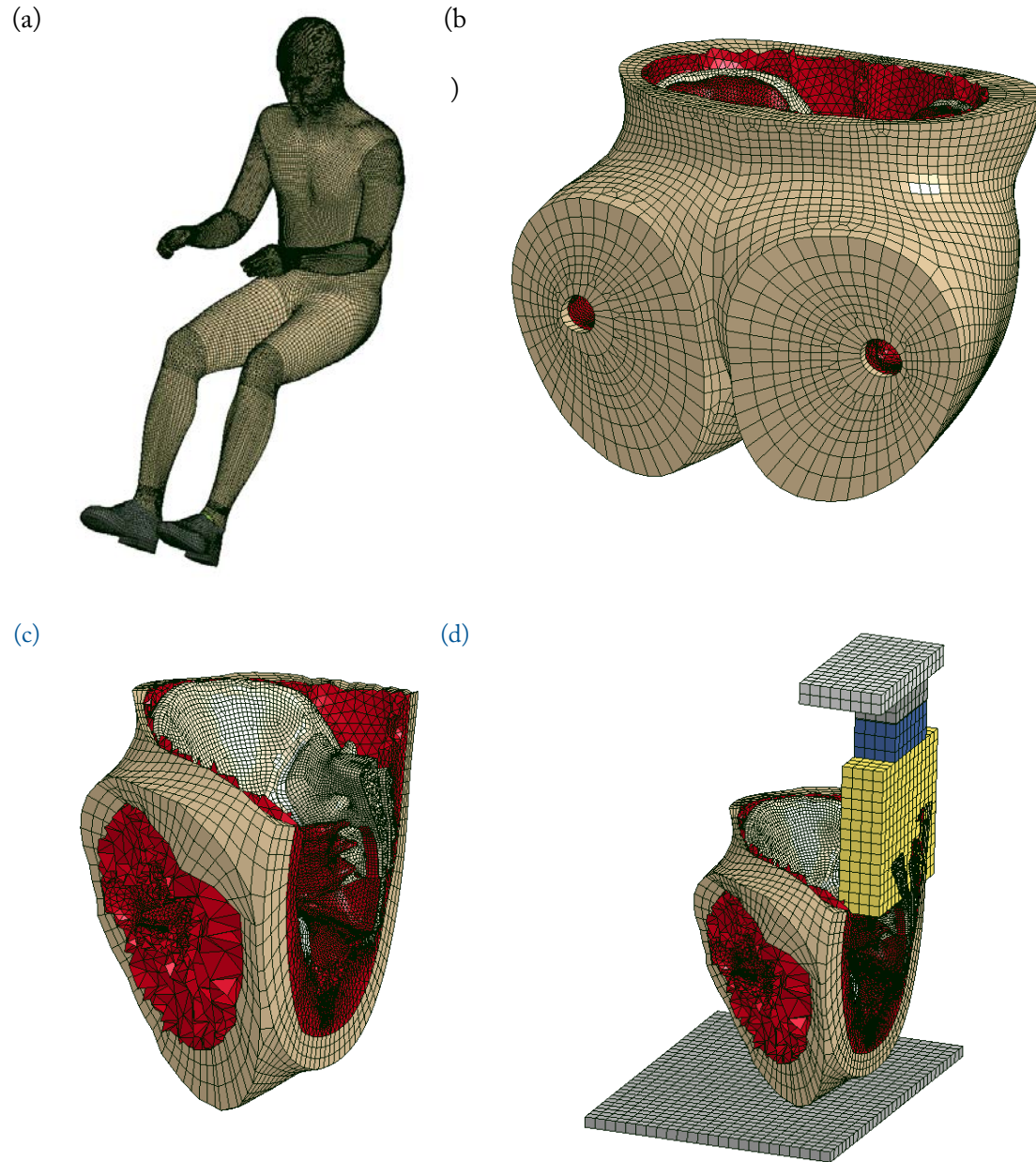


Figure 39. The whole body GHBMC FE model (a) was used as the base for the pelvis component FE model. The pelvis was isolated (b), then elements were trimmed to represent the experimental tests, and the model was halved to decrease computation time (c). Finally, the pot and test hardware were added (d).

The pot was created using the `*MAT_PIECEWISE_LINEAR_PLASTICITY` material card, matching dimensions and material properties of the material data sheet from the manufacturer (Figure 39d). It measured 140 mm in the x-axis, 80 mm in the y-axis (before halving), and 140 mm in the z-axis, with a density of 1.04 g/cm<sup>3</sup>. The sacrum was constrained in the pot using `*CONSTRAINED_LAGRANGE_`

IN\_SOLID, and the pot was constrained via shared nodes to a rigid load cell part created to match the mass of the experimental load cell. Careful consideration was given to how each individual pelvis was positioned into the pot. Computed Tomography (CT) scans from each experimental pelvis test were analyzed using MIMICS 19.0 (Materialise, Leuven, Belgium) to ensure that the sacrum positioning in the pot was preserved. The load cell was split down the neutral axis of the load cell and a stiff beam using the \*MAT\_LINEAR\_ELASTIC\_DISCRETE\_BEAM material card was inserted to calculate the loads and moments. The load cell was attached via shared nodes to the carriage, which represents the effective mass of the upper body, and matches the mass used experimentally. The skin of the pelvis made contact with a rigid seat platen using \*CONTACT\_AUTOMATIC\_SURFACE\_TO\_SURFACE, with an assumed 0.3 static coefficient of friction.

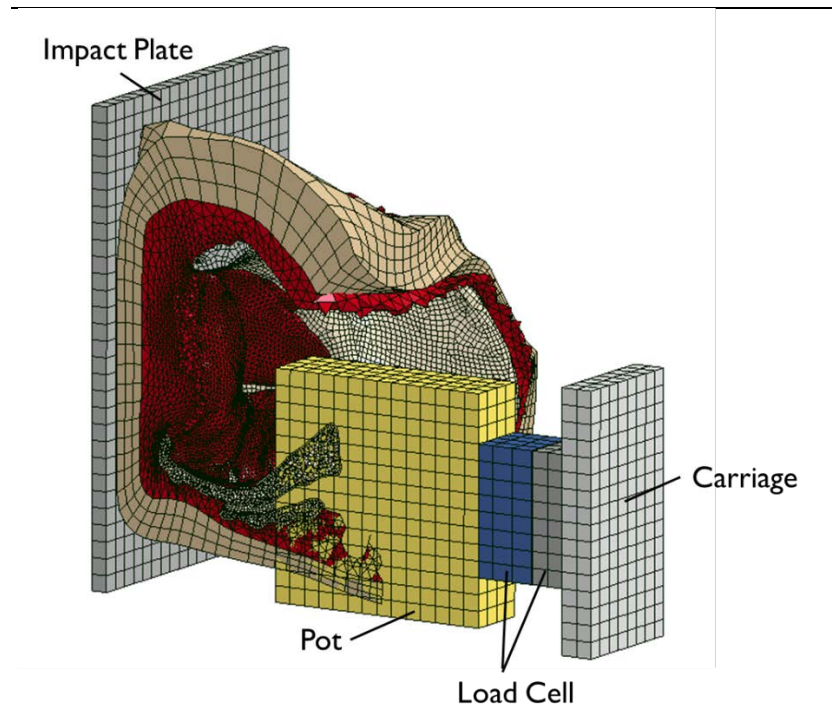
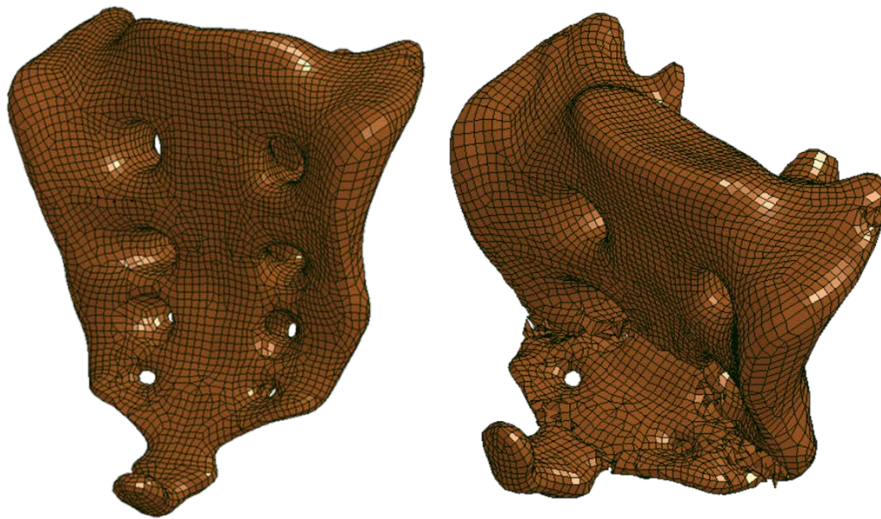


Figure 40. The VIP model shown with the impact plate, pot, load cell, and carriage modeled after their respective experimental counterparts.



Initially, specimen specific models were created for all thirteen experimental pelvises in terms of pelvic angle and sacrum positioning. However, early benchmarks of the VIP models in the 56° pelvic angle showed that the coccyx and sacrum suffered significant fractures under nominal failure strains, when no fractures were reported in the experimental study (see Figure 52). While the fracture properties of the bone could be changed to prevent fracturing, it was clear from that posture that significant amounts of loading go through the sacrum and coccyx. The material properties of the sacrum, coccyx, and associated ligaments are not validated to any experimental data, so just eliminating fracture is not enough to ensure biofidelity of these parts.



---

Figure 41. The Sacrum of the 56° angle pelvis model fractured under nominal bone fracture values.

---

In this end, the objective of this model was not just to show that a model could be built to recreate the UBB experimental tests; it was also used as validation so that the load path could be analyzed using the VIP model. While the VIP model has the flexibility to change posture to recreate all the different UBB experimental tests, a single test was chosen as the base model to simplify the analysis through the test matrix. In addition, when using a single load curve, it was found that FE recreations of the UBB experimental tests



within the same posture had very little difference between each other (see Figure 52). Therefore, small variations in pelvic angle and sacrum positioning in the pot had little effect on the overall response in the FE, and that the difference in response was almost entirely driven by the variation in the input from the impact plate. While individual pelvis geometry, mass, and tissue thickness has an effect on the load response, those were not specifically looked at in this thesis for the purpose of validation from the experimental data.

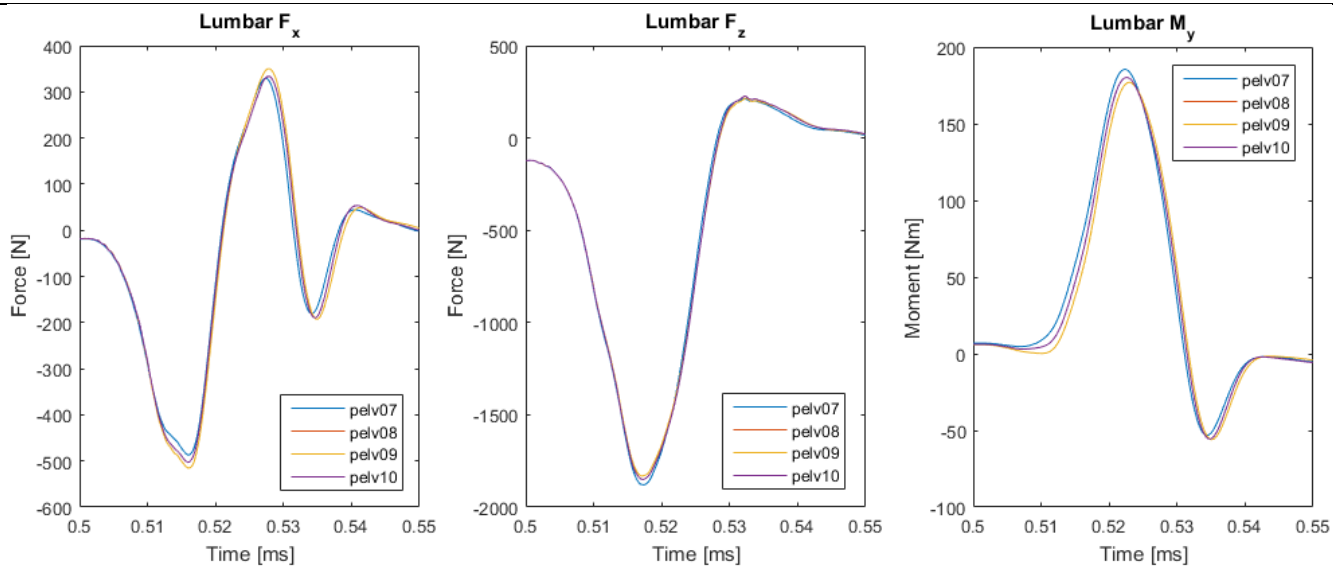


Figure 42. Using the same load curve for a set of experimental tests with the same pelvic angle, small variations in pelvic angle and sacrum positioning within the pot had little effect on the overall response.

### 5.2.2 Coordinate System

The global coordinate system used for the VIP model is consistent with the Society of Automotive Engineers (SAE) J1733 standard (Figure 52a) [101]. With the pelvic angle prescribed from the UBB experimental tests, the z-axis measures from the pelvis orthogonal to the impact plate. The y-axis is to the right of the pelvis, and the x-axis is the cross product of the y- and z-axes. The origin of the load cell is at the center of the small beam connecting the two load cell sections. The load cell beam uses the x-, y-, and

z-global axes, with the recorded outputs being the force in the x- and z-axes and the moment in the y-axis— $F_x$ ,  $F_z$  and  $M_y$ , respectively (Figure 52b).

The rotation of the pelvis during impact was also recorded. The angle was measured between a line from the center of mass of the pubic symphysis to the midpoint of the right and left sacroiliac joint center of mass, and the z-axis (Figure 52c).

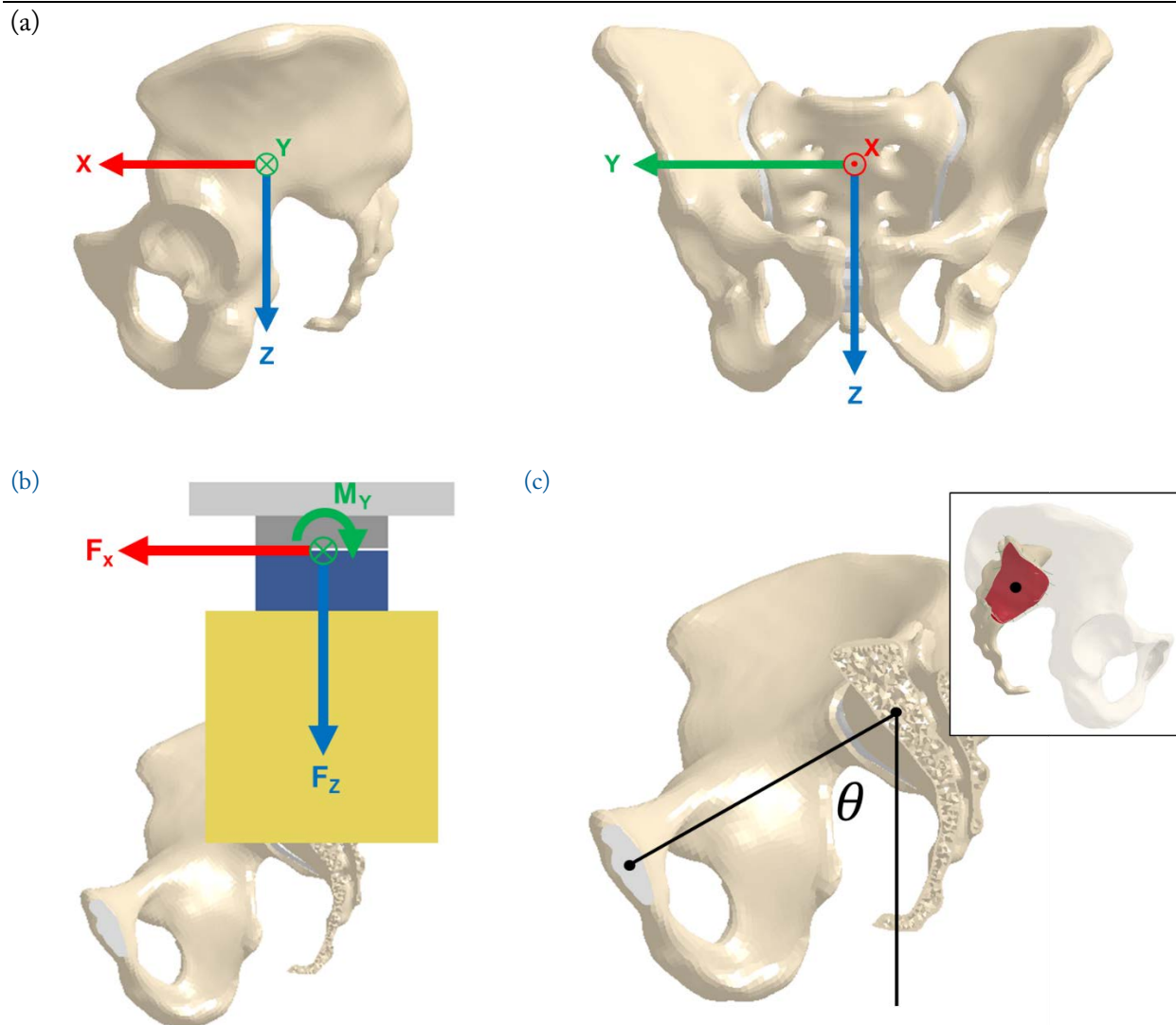


Figure 43. Global coordinate system (a), load cell force and moment directions (b), and pelvic angle (c) with sacroiliac joint highlighted red in alternate view.

### 5.2.3 Input and Boundary Conditions

Each simulation was split into two segments: the preload simulation and the load simulation. Similar to the process for the gluteal tissue model, the preload simulation did not have viscoelasticity enabled. This allowed the simulation to settle much quicker and reduce total computation time. To represent the constant force springs in the UBB experimental tests, a constant force in the negative z-axis was applied to the impact plate. This forced the pelvis to compress against the impact plate while the carriage was set to be static. Although experimentally the springs were actually pulling the carriage to the impact plate rather than the impact plate being pulled to the carriage, but the effective precompression state is equivalent, and the simulation reached equilibrium quicker because fewer elements were accelerated during the precompression. In addition, gravity was introduced using a constant force in the negative x-direction applied to all parts. The carriage, load cell, and impact plate were constrained to only translate along the z-axis. Each preload simulation ran for 500 ms, which was the time it took for the tissue compression to reach equilibrium. The final node positions of the pelvis were extracted from the simulation.

For the load simulation, the extracted final node positions were set to be the starting node positions so that the pelvis started in the precompressed state. To keep the stress state of the tissue from the preload, \*INITIAL\_FOAM\_REFERENCE\_GEOMETRY was used. This option is available to most hyperelastic models in LS-DYNA and allows initial stresses to be calculated by the difference in the original node positions (uncompressed state) and the starting node positions (compressed state). The stress calculation only depends on the deformation gradient  $F_{ij}$ , which is equal to the derivative of the deformed state,  $x_i$ , with respect to the undeformed state,  $X_j$  (see Equation 15).

$$F_{ij} = \frac{\partial x_i}{\partial X_j} \quad \text{Equation 15}$$

The impact was achieved by prescribing the displacement of the impact plate. The displacement was taken as the double derivative of the average acceleration from the four accelerometers on the experimental impact plate. The nominal impact was a 2 m/s impact with a time to peak velocity of 10 ms. After differentiation, this amounted to a 32 mm intrusion in 28 ms. The spring force was switched to be in the positive z-direction, and in addition, a smaller friction force was also added in the positive z-direction. This friction force, ~100 N, was tested experimentally as the force required to pull a simulated pelvis on the carriage along the tracks. The load simulation run time was 50 ms, which was able to capture all of the loading behavior as well as some unloading behavior of the pelvis.

#### 5.2.4 Test Matrix

A total of 26 different simulations were run with varying material properties, loading rates, and tissue geometries (see Table 9). The nominal model had the mean soft tissue material properties and was used as the baseline comparison. Including the nominal model, nine base simulations were run using different variations of the updated soft tissue properties from the gluteal tissue model. Each simulation had a combination of either the maximum, mean, or minimum of the recorded shear moduli,  $\mu$ , and shear relaxation moduli,  $G_i$ . Using the maximum and minimum values allowed for the observation of large variation in the tissue types tested experimentally. Each model was named after which extreme values were used in the material formulation. Since the shear modulus was found via the preload simulation, and the shear relaxation moduli from the load simulation, the extrema were prefixed by either “P” for preload or “L” for load. For example, the simulation with the mean shear modulus and minimum shear relaxation moduli was named “Pmean\_Lmin”.

Because the model had three time constants—and therefore three shear relaxation moduli—the maximum, mean, and minimum of each modulus could not necessarily be taken separately. Since  $\sum G_i + G_\infty = 1$ , in this case the maximum of each relaxation modulus could not be included in a single model, because the

sum exceeded 1. Instead, the shear relaxation moduli from the model with the maximum and minimum  $\sum G_i$  were used to represent the maximum and minimum shear relaxation portions of the material model. This way,  $\sum G_{max}$  had the smallest  $G_\infty$ , and vice versa.

Table 9. Summary of all variations of VIP FE model simulations.

Model Name	$\mu$ [GPa]	$G_1$ [GPa]	$G_2$ [GPa]	$G_3$ [GPa]	Load Time [ms]	Other
Pmin_Lmin	8.0E-7	5.13E-1	1.95E-1	1.50E-1	28	
Pmin_Lmean	8.0E-7	6.14E-1	1.77E-1	1.48E-1	28	
Pmin_Lmax	8.0E-7	6.65E-1	1.85E-1	1.30E-1	28	
Pmean_Lmin	2.8E-6	5.13E-1	1.95E-1	1.50E-1	28	
Pmean_Lmean	2.8E-6	6.14E-1	1.77E-1	1.48E-1	28	Nominal model
Pmean_Lmax	2.8E-6	6.65E-1	1.85E-1	1.30E-1	28	
Pmax_Lmin	5.6E-6	5.13E-1	1.95E-1	1.50E-1	28	
Pmax_Lmean	5.6E-6	6.14E-1	1.77E-1	1.48E-1	28	
Pmax_Lmax	5.6E-6	6.65E-1	1.85E-1	1.30E-1	28	
Pmin_Lmean_HighRate	8.0E-7	6.14E-1	1.77E-1	1.48E-1	14	
Pmean_Lmin_HighRate	2.8E-6	5.13E-1	1.95E-1	1.50E-1	14	
Pmean_Lmean_HighRate	2.8E-6	6.14E-1	1.77E-1	1.48E-1	14	
Pmean_Lmax_HighRate	2.8E-6	6.65E-1	1.85E-1	1.30E-1	14	
Pmax_Lmean_HighRate	5.6E-6	6.14E-1	1.77E-1	1.48E-1	14	
Pmin_Lmean_LowRate	8.0E-7	6.14E-1	1.77E-1	1.48E-1	56	
Pmean_Lmin_LowRate	2.8E-6	5.13E-1	1.95E-1	1.50E-1	56	
Pmean_Lmean_LowRate	2.8E-6	6.14E-1	1.77E-1	1.48E-1	56	

Pmean_Lmax_LowRate	2.8E-6	6.65E-1	1.85E-1	1.30E-1	56	
Pmax_Lmean_LowRate	5.6E-6	6.14E-1	1.77E-1	1.48E-1	56	
Pmean_Lmean_Thin	2.8E-6	6.14E-1	1.77E-1	1.48E-1	28	Tissue thickness reduced
Pmean_Lmean_Heavy	2.8E-6	6.14E-1	1.77E-1	1.48E-1	28	1 kg added to carriage
Pmean_Lmean_SISStiff	2.8E-6	6.14E-1	1.77E-1	1.48E-1	28	b = 0.008
Pmean_Lmean_SILoos	2.8E-6	6.14E-1	1.77E-1	1.48E-1	28	b = 0.002
GHBMCE	-	-	-	-	14	Default GHBMCE tissue properties
GHBMCHighRate	-	-	-	-	28	
GHBMCLowRate	-	-	-	-	56	

To compare the rate sensitivity of the VIP model with the new soft tissue properties, various simulations were rerun while either doubling or halving the displacement time of the impact plate. Enough of the nine base simulations were rerun with these changes to be able to compare the effects of different shear moduli and shear relaxation moduli on rate effects.

While the VIP model was updated to resemble the UBB experimental tests, it was not an exhaustive approach to make the model more biofidelic. Joint and bone material properties, morphing of the bone and soft tissue, and pelvis mass were not explored to the point of validation in the scope of this thesis. While actions were not taken to validate any of these properties in the VIP model, it was hypothesized that they would have an effect on the impact response. To explore this hypothesis, two more types of simulations were run.

In one of these simulation types, the sacroiliac (SI) joint material properties were varied (see Figure 44).

The cartilage portion of the SI joint in the VIP model is modeled using a Mooney-Rivlin rubber model

(\*MAT\_MOONEY-RIVLIN\_RUBBER), and the ligaments were modeled using \*MAT\_CABLE\_DISCRETE\_BEAM. To investigate the effect the SI joint material properties had on loading, the shear modulus of the cartilage part was increased and decreased. The nominal material constant,  $b$ , for the shear modulus was 0.0041 GPa, with the variations being changed to 0.008 and 0.002.

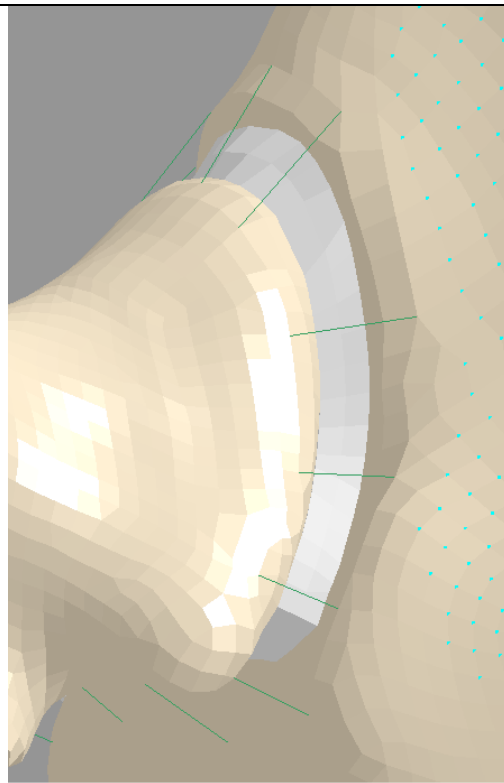


Figure 44. The SI joint of the VIP model. The white elements represent the cartilage while the green beams represent the ligaments.

From early iterations of the VIP model, it was clear that the force response of the pelvis was sensitive to the thickness of the tissue prior to impact. A thinner layer of tissue led to higher forces at the lumbar load cell than a layer of thicker tissue. Without changing input conditions, boundary conditions, or material properties, the thickness of the tissue is dictated by the relaxation of the tissue. It was theorized that, when compared to thicker layer of tissue, a thinner layer of tissue with the same material properties and relaxation would also increase the forces at the lumbar load cell. To test this, a simulation was run where the portion



of the soft tissue that comes in contact with the impact plate was morphed and thinned relative to the nominal model. At the thickest point, the tissue was 18 mm thinner than nominal. This reduction led the thickness of the tissue in between the impact plate and the ischium after precompression to be about 8 mm thinner, or a reduction of 36%. This also led to a reduction of about 6% overall tissue volume and a loss of 0.44 kg. Because a change of mass was also assumed to play a role on loading forces, the nominal model was rerun with the carriage being 1 kg heavier. While this is not exactly the same as the pelvis being 1 kg heavier, it allowed a clear comparison with the nominal case without changing material properties. which in turn has its own effects on the force response.

### 5.2.5 Methods

In order to compare the different simulations, several methods of comparison were used. The lumbar force response from the load cell was used as a metric to compare the FE models to the UBB experimental data and is used again when comparing different FE simulations. In addition, the rotation of the pelvis was also recorded, measured from the pubic symphysis about the SI joint.

Two methods were used to compare lumbar forces and moments from the VIP models to the experimental data. The first method was a corridor method. In this technique, the mean and standard deviation (SD) signal for each point in time was calculated for all of the experimental data curves. The corridor is created by enclosing an area between  $mean + SD$  and  $mean - SD$  at each data point. The VIP model output was then compared to this corridor, and the percentage of how much that signal was in the corridor was calculated. The second method was to use CORA, as described in detail earlier. This time, the corridor rating was used and had equal weights with the correlation rating. Phase, size, and shape also had equal weightings.

A series of cross-sections (\*DATABASE\_CROSS\_SECTION) were also used for analysis (see Figure 52). The cross-sections were placed in the transverse plane, or xy-plane, and were parallel to the impact plate. Cross-sections were placed across the whole z-length of the precompressed pelvis every 5 mm, which amounted to 40–50 cross-sections depending on the amount of compression in the tissue. The output of each cross-section measures position, centroid, force, and moment in each axis. These outputs are the sum from each element that is bisected from each plane in its initial state. Each cross-section follows the same elements throughout the entire simulation, regardless of deformation.

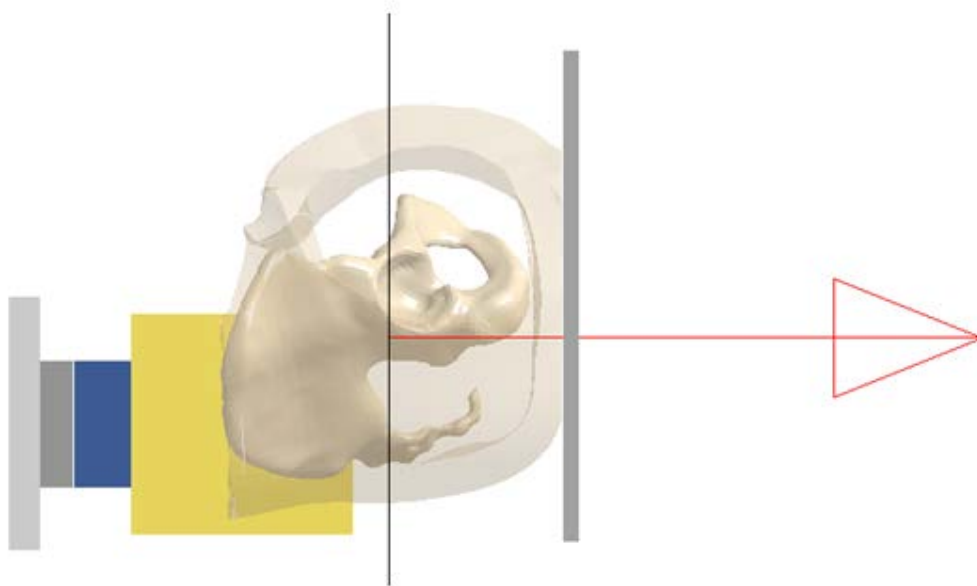


Figure 45. The vertical black line represents one of many cross-sections in the FE model. The red arrow dictates the positive direction of the values recorded from the cross-section.

Five copies of each cross-section were made, with each cross-section measuring output of only specific types of elements and their respective nodes. The first cross-section included all elements in each plane. The next two measured only the hard tissue (i.e. bone) and soft tissue, respectively. The final two cross-sections measured either only the coxal bone elements or the elements from the coccyx.

The first type of analysis using the cross-sections was the analysis of the load path. This was done by calculating the point of average force along the x-axis,  $X_{avg}$ . Each cross-section sums all the forces found in each element it bisects. It also sums the total moment created by that force applied about the centroid. The location of average force represents a point within that plane that if the total force is applied as a single force at that point it creates an equivalent total moment about the centroid. The distance that point is from the centroid is the equivalent moment arm created by that force. While forces and moments were recorded in each axis, because the model is symmetric and because the force in the z-axis goes through the centroid in the x-axis, the center of force in the x-axis is only a function of the centroid in the x-direction,  $X_{centroid}$ , the moment in the y-direction,  $M_y$ , and the force in the z-direction,  $F_z$  (see Equation 16).

$$X_{avg} = X_{centroid} + \frac{M_y}{F_z} \quad \text{Equation 16}$$

The center of force was calculated for each cross-section at each point in time. Visualizations were also created in order to see the change in location and magnitude the center of force during the entire simulation run time. A video of the simulation of the VIP model being impacted was overlaid by these points to visualize the location of the center of force in the pelvis. Figure 46 shows an example of the nominal model at 16 ms, with each cross-section represented by a dot. The vertical axis shows the location of the average force in the x-axis, and the horizontal axis is the centroid of each cross-section in the z-axis. The color of the point corresponds to the total force in the cross section, referenced to the color bar legend to the right of the plot. The vertical red line represents the cross-section with the highest load at that point in time. In the example in Figure 46a, the peak force is currently in the cross-section bisecting the sacral ala. This entire process was repeated for the anterior-posterior orientation, where instead the average force was calculated for the y-axis (see Figure 46b).

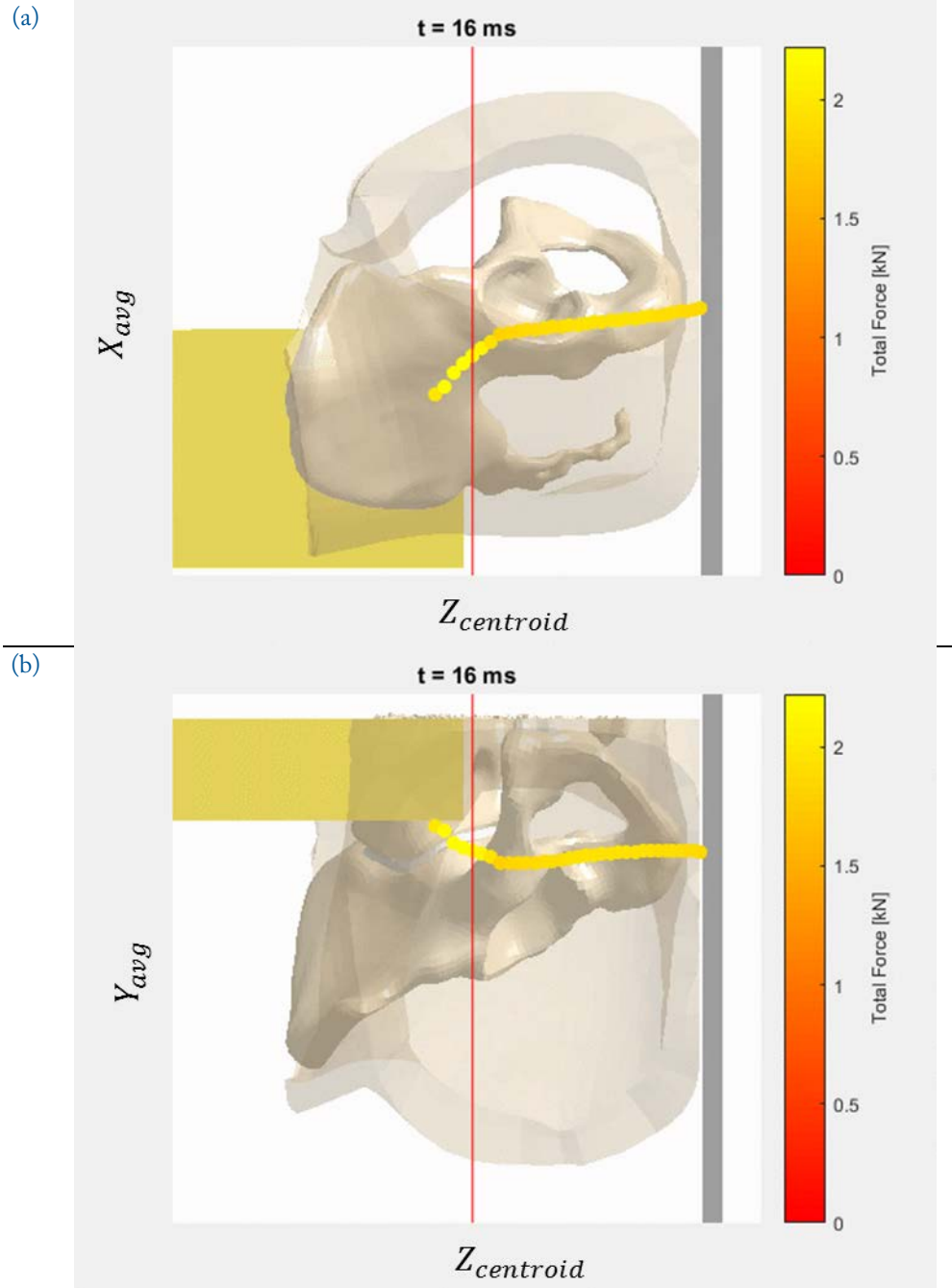


Figure 46. Example of the nominal simulation showing the position of the center of force in the x-axis (vertical axis) and the cross-section centroid in the z-axis (horizontal axis). The color of each point corresponds the total force in that cross-section at that point in time. The red vertical line represent the cross-section with the highest force at that time.

Using the cross-sections that used either the bone or soft tissue, the amount of the load being carried by the bone and soft tissue was calculated in terms of the percent of the total load. Another visualization was

created, but this time representing these percentages. Figure 47 shows the nominal model and the amount of the total load being carried by the bone and tissue. In this visualization, the vertical axis does not represent a location in the pelvis, but instead shows the percentage of total load, shown on the vertical axis. The horizontal axis is the same as the previous visualization and shows the location of the centroid of the cross-section in the z-axis.

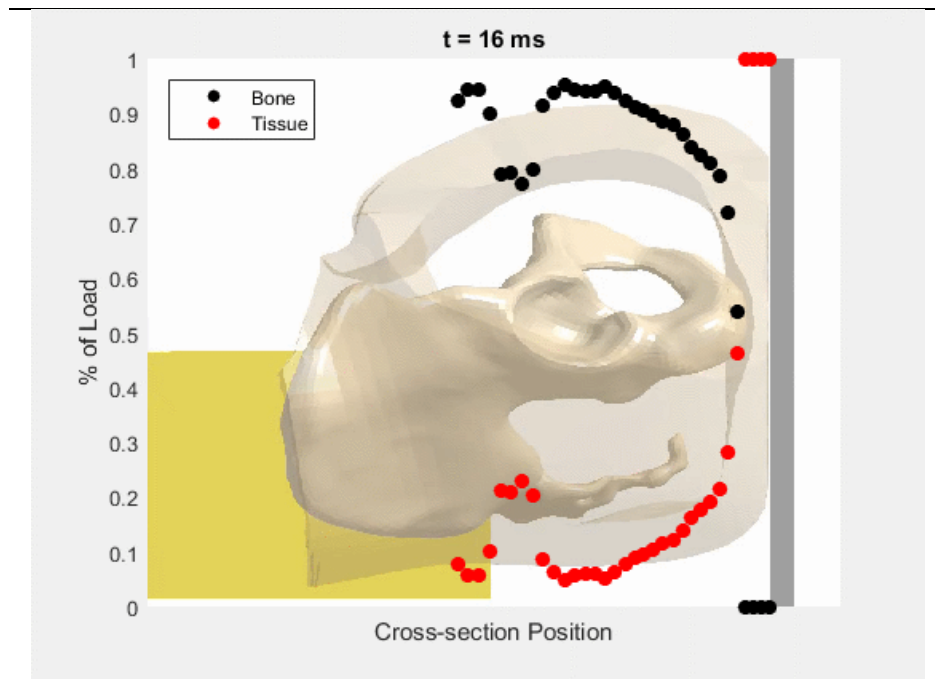


Figure 47. Example of the nominal case simulation showing the percentage of total load carried by the tissue and bone with respect to each cross-section.

In an identical method, the percentage of the total load through bone carried by the coxal bone and coccyx is shown in Figure 48.

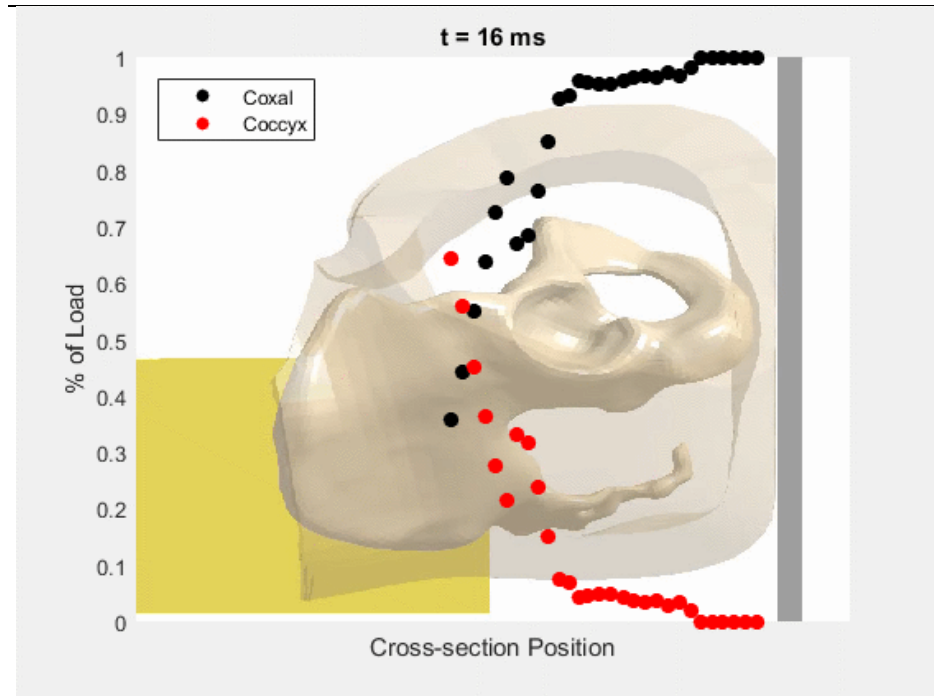


Figure 48. Example of the nominal case simulation showing the percentage of total bone load carried by the coxal bone and coccyx with respect to each cross-section.

## 5.3 Results

### 5.3.1 Tissue Compression

The variation in the shear and shear relaxation moduli resulted in vastly different tissue thicknesses and tissue compression (see Table 10). The thickness of the tissue was measured between the impact plate and the closest point of the ischium in the z-direction to the impact plate. A higher tissue thickness means less compression occurred. This thickness was recorded at the end of precompression and at peak compression during the impact. The tissue thickness in the model after precompression with the mean shear modulus was 22 mm. The maximum shear modulus resulted in a 30 mm thickness and 7.3 mm in the minimum model. In all nine of the base cases, a higher  $\sum G_i$  resulted in less compression than models with a lower  $\sum G_i$ , though the difference was much lower than the difference between the different shear moduli. For example, the Pmean\_Lmean model compressed about 2 mm more than the Pmean\_Lmax model and about 1 mm less than Pmean\_Lmin model.

Table 10. Summary of tissue compression.

Model Name	Ischium to	Ischium to Plate
	Plate Distance, Relaxed [mm]	Distance, Impacted [mm]
Pmin_Lmin	7.3	2.2
Pmin_Lmean	7.3	2.3
Pmin_Lmax	7.3	2.9
Pmean_Lmin	22.0	8.3
Pmean_Lmean	22.0	9.4
Pmean_Lmax	22.0	11.5
Pmax_Lmin	30.0	13.3
Pmax_Lmean	30.0	15.1
Pmax_Lmax	30.0	18.2
Pmin_Lmean_HighRate	7.3	2.0
Pmean_Lmin_HighRate	22.0	6.6
Pmean_Lmean_HighRate	22.0	7.4
Pmean_Lmax_HighRate	22.0	9.4
Pmax_Lmean_HighRate	30.0	12.3
Pmin_Lmean_LowRate	7.3	2.8
Pmean_Lmin_LowRate	22.0	10.7
Pmean_Lmean_LowRate	22.0	12.0
Pmean_Lmax_LowRate	22.0	14.4

Pmax_Lmean_LowRate	30.0	18.5
e		
Pmean_Lmean_Thin	14.2	3.3
Pmean_Lmean_Heavy	22.0	9.2
Pmean_Lmean_SIS stiff	22.0	9.0
Pmean_Lmean_SILoos	22.0	9.9
e		
GHBMC	19.9	12.9
GHBMC_HighRate	19.9	12.0
GHBMC_LowRate	19.9	14.2

This trend is consistent between the different loading rates. All the higher rate models compressed more and all of the lower rate models compressed less than their respective nominal model. The higher rate models compressed between 0.2 and 3 mm more than the nominal models—or between 10 and 19% more—with the largest change occurring in the Pmax\_Lmean model. The thin model, which was 36% thinner than the nominal model, compressed 35% more on both the precompression and during peak compression during impact.

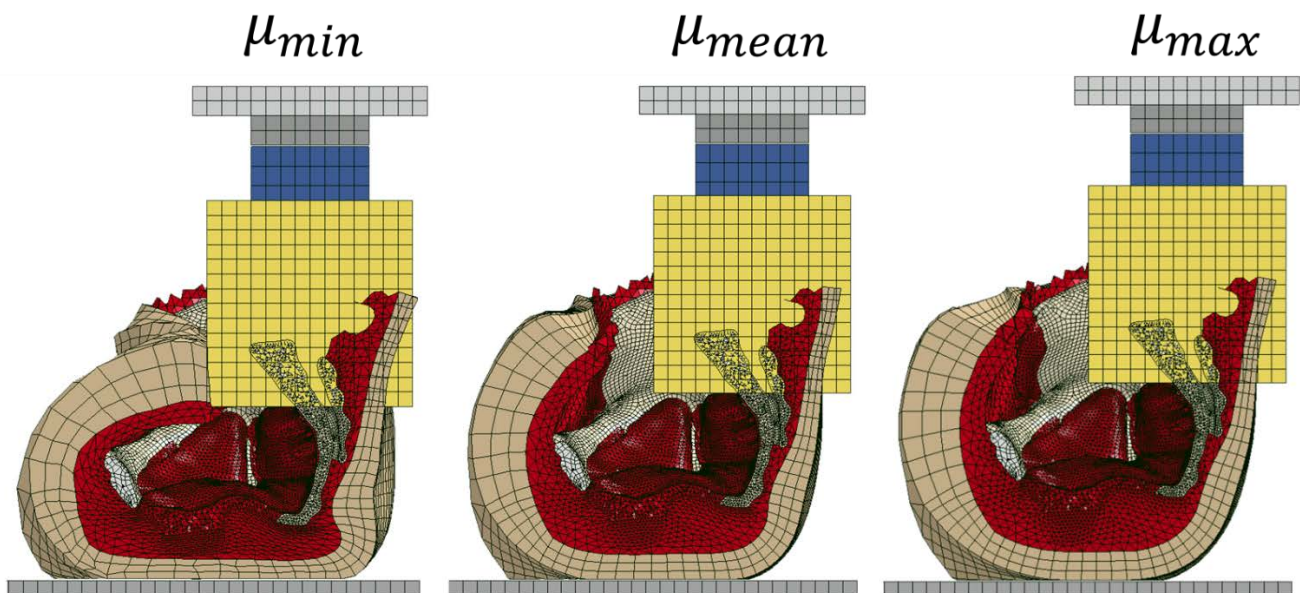


Figure 49. Tissue compression between models with different shear moduli was significantly different.



The GHBMC tissue model compressed 2 mm more during precompression but compressed 3.5 mm less during peak impact. In addition, the GHBMC was less sensitive to change in rate in terms of tissue compression. The high rate compressed 7% more on the high rate and 10% less on the low rate, compared to the nominal model which compressed 21% more in the high rate and 22% less in the low rate model.

The heavy model and the models with different SI joint stiffness had negligible differences in tissue compression.

### 5.3.2 Event Timing

From the results, it was important to understand the timing of the different events during the impact of the pelvis. Because the carriage was not fixed in its position, the timing of some events was not necessarily straightforward. For example, even though the impact plate reached peak displacement at 28 ms in the nominal case, the peak force happened much earlier, because the pelvis started to overcome friction and begin accelerating. More so, the pelvis tended to start disconnecting from the plate prior to the peak displacement of the impact plate. Table 10 shows a summary of peak timings.

Forces in the x- and z-direction typically peaked around the same time, usually within a couple milliseconds of each other, although the rate of the impact varied this trend. In the nominal 28 ms load time,  $F_x$  typically peaked 1–2 ms before  $F_z$ , although there were a couple cases in which  $F_z$  either peaked first or peaked at the same time. In the higher rate impact, 14 ms load time,  $F_z$  peaked before  $F_x$ , and in the lower rate impact, 56 ms load time, the opposite was true. Just milliseconds before the forces peak is when the carriage overcame the spring force and friction and began translating (see Figure 52). The forces peak and start to unload at the high slope portion of the carriage displacement (the carriage velocity).

Table 11. Summary of peak timings of forces, moments, and rotations.

	Load	Peak $F_x$	Peak $F_z$	Peak $M_y$	Peak $R_y$
Model Name	Time	Time	Time	Time	Time
	[ms]	[ms]	[ms]	[ms]	[ms]
Pmin_Lmin	28	11.8	13.3	20.3	15
Pmin_Lmean	28	11.3	13.1	20.4	15
Pmin_Lmax	28	12.6	12.2	20.2	14
Pmean_Lmin	28	15	16.5	22	19
Pmean_Lmean	28	15	15.7	22.2	18
Pmean_Lmax	28	14.4	14.4	22.8	17
Pmax_Lmin	28	15.2	17.8	22.4	21
Pmax_Lmean	28	15	16.3	22.2	19
Pmax_Lmax	28	14.5	14.7	22.8	17
Pmin_Lmean_HighRate	14	8	6.6	15.7	10
Pmean_Lmin_HighRate	14	10.4	9.8	16.8	12
Pmean_Lmean_HighRate	14	10.2	9.5	16.9	12
Pmean_Lmax_HighRate	14	9.8	8.6	17	11
Pmax_Lmean_HighRate	14	10.2	9.8	17.1	13
Pmin_Lmean_LowRate	56	20.9	21	29	23
Pmean_Lmin_LowRate	56	25.5	27.4	32	29
Pmean_Lmean_LowRate	56	23.9	25.9	31.7	28
Pmean_Lmax_LowRate	56	22.2	23.3	32.6	26

Pmax_Lmean_LowRate	56	23.7	27.1	32.5	29
e					
Pmean_Lmean_Thin	28	15.8	15.7	23.1	17
Pmean_Lmean_Heavy	28	15.3	16.2	22.8	18
Pmean_Lmean_SISStiff	28	14.8	15.5	21.4	18
Pmean_Lmean_SILoos	28	15.5	15.6	22.8	19
e					
GHBM	14	11.7	14.5	20.8	16
GHBM_HighRate	28	7.9	7.6	15.9	11
GHBM_LowRate	56	18.2	22.3	28.2	24

Tissue with a lower shear modulus peaked earlier than those with a higher shear modulus and the same shear relaxation moduli. A lower shear modulus led to more tissue compression, and therefore the impact plate was closer to the ischium at the start of impact. However, the physical distance between the impact plate and the ischium by itself did not cause an earlier peak in the loads because the thin model case—which had identical material properties as the nominal model other than thinner tissue near the ischium—did not show significant change in timing of the forces, moments, or rotations relative to the nominal model. Even though the ischium was closer to the impact plate at the start of loading in the thin model, the displacement of the carriage was delayed relative to the nominal model (see Figure 50). The carriage in both models appeared to move slightly closer to the pelvis as the plate impacted the soft tissue before the bone became engaged, with this more noticeable in the thin model. This was due to the simultaneous events of the tissue being compressed and the constant forces springs continuing to force the pelvis toward the impact plate. As mentioned previously, the forces peaked once the carriage reached its highest velocity (highest slope in Figure 50), which in this case, led the peak forces to be a couple milliseconds after the nominal mode. While the tissue thickness in the thin model case decreased by about 33% compared to the nominal case, losing the thickness of tissue also decreased the weight of the model by 0.44 kg, which added another variable to the timing of events. The forces in the heavy model, which also shared the same material

properties as the nominal model but was 1 kg heavier, peaked later than the nominal model, although the increase was very small.

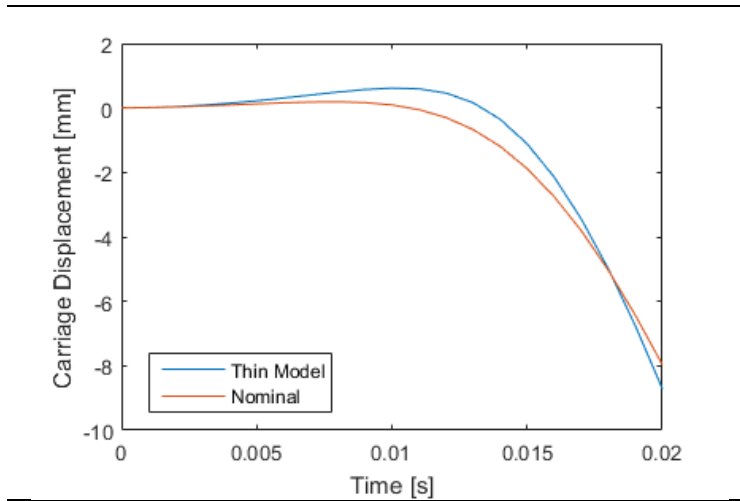


Figure 50. The nominal model starts moving with the impact direction before the thin model.

Shear relaxation moduli did not correlate well with peak  $F_x$  timing; however, as  $\sum G_i$  decreased, the peak time for  $F_z$  came later in all of the nine base cases.

The next event chronologically was the peak rotation of the pelvis about the SI joint,  $R_y$ . In the nominal loading input, the rotation peaked around 2–3 ms after the peak forces, but before the peak y-moment. Many of the trends of peak rotation are similar to those trends found in the forces. A lower shear modulus resulted in an earlier peak rotation than those with a higher shear modulus. In addition, a higher  $\sum G_i$  resulted in an earlier peak.

The last event was the peak of the y-moment. The trends in the peak timings followed that of the forces and rotations; however, they were less pronounced. For example, the difference in peak moments between the min and max shear modulus was only about 2 ms, while the forces and rotations changed about double that in the same comparison.

All these trends in material property differences held for both the lower and higher loading rates. Across all material different trends, the difference between the max and mean shear modulus or shear relaxation moduli were lower than the difference between the mean and minimum. This was because the minimum shear modulus was farther from the mean than the maximum shear modulus was.

The change in the SI joint properties did not significantly change the event timings. The stiff SI peaked slightly before the nominal model in terms of  $F_x$  and  $M_y$ , but  $F_z$  and  $R_y$  saw little to no change. The loose SI model had the opposite conclusion in terms of timing of  $F_x$  and  $M_y$ .

Relative to the nominal model, the  $F_x$  from the GHBMC model peaked significantly early relative to other trends—over 3 ms. While not as significant,  $F_z$ ,  $M_y$ , and  $R_y$  also all peaked before the nominal model. These trends were the same in the comparison between the respective high and low rate GHBMC models.

### 5.3.3 Forces and Moments

Significant and relevant plots and scores will be shown here; for full tabulation of corridor and CORA scores as well as plots of every case, please reference the appendix.

The lumbar forces and moments from the UBB experimental tests had characteristic patterns that were, to at least some extent, captured by the VIP models (see Figure 52). The force in the x-direction had a sinusoidal-like pattern, with a mean trough of -1550 N at 13 ms into the impact, followed by a mean peak of 550 N at 26 ms. Forces in the z-direction looked similar to a half-sine wave. The mean peak force was approximately -3500 N at 13 ms. The y-moment also had a sinusoidal-like pattern, with a lesser mean trough of about -75 Nm at 13 ms, and a higher mean peak of about 110 nm at 24 ms that dragged out for tens of milliseconds before returning back to zero. As seen in the corridors, the y-moment had relatively large corridors compared to the x- and z-forces. The trough and peak of  $F_x$  has the same timing as the trough and peak of  $M_y$ .

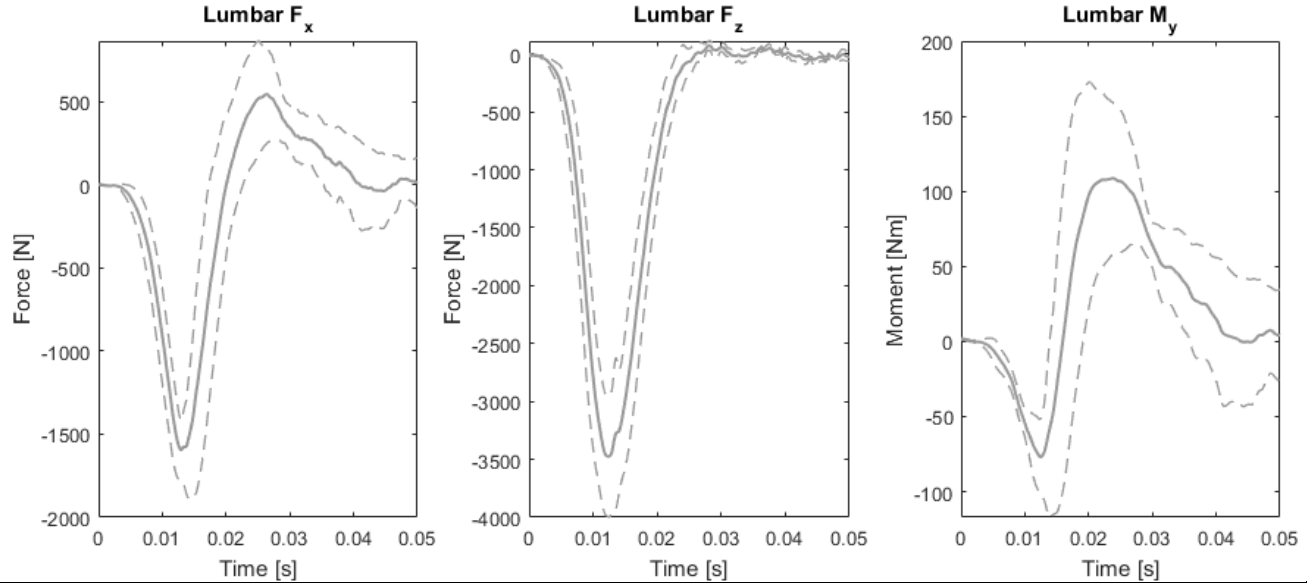


Figure 51. Mean (solid line) experimental data with standard deviation corridors (dashed lines).

Before making modifications to the tissue material properties and tissue geometry, among other changes made to match the UBB experiment tests, the stock GHBMC model was compared to the experimental data (see Figure 52). When compared to all the changes in the VIP model, the VIP model made significant improvements to the model. The VIP model nearly doubled  $F_x$  from -466 N to -877 and phase-shifted the peak by about 2 ms closer to the experimental data. It also increased  $F_z$  by nearly 1 kN from -1771 N to -2638 N with a 2 ms phase shift as well.  $M_y$  stayed about the same in magnitude and shape. Excluding  $M_y$  the CORA scores of the VIP model increased from the unmodified model, with  $F_z$  seeing the largest increase from 0.398 to 0.592.

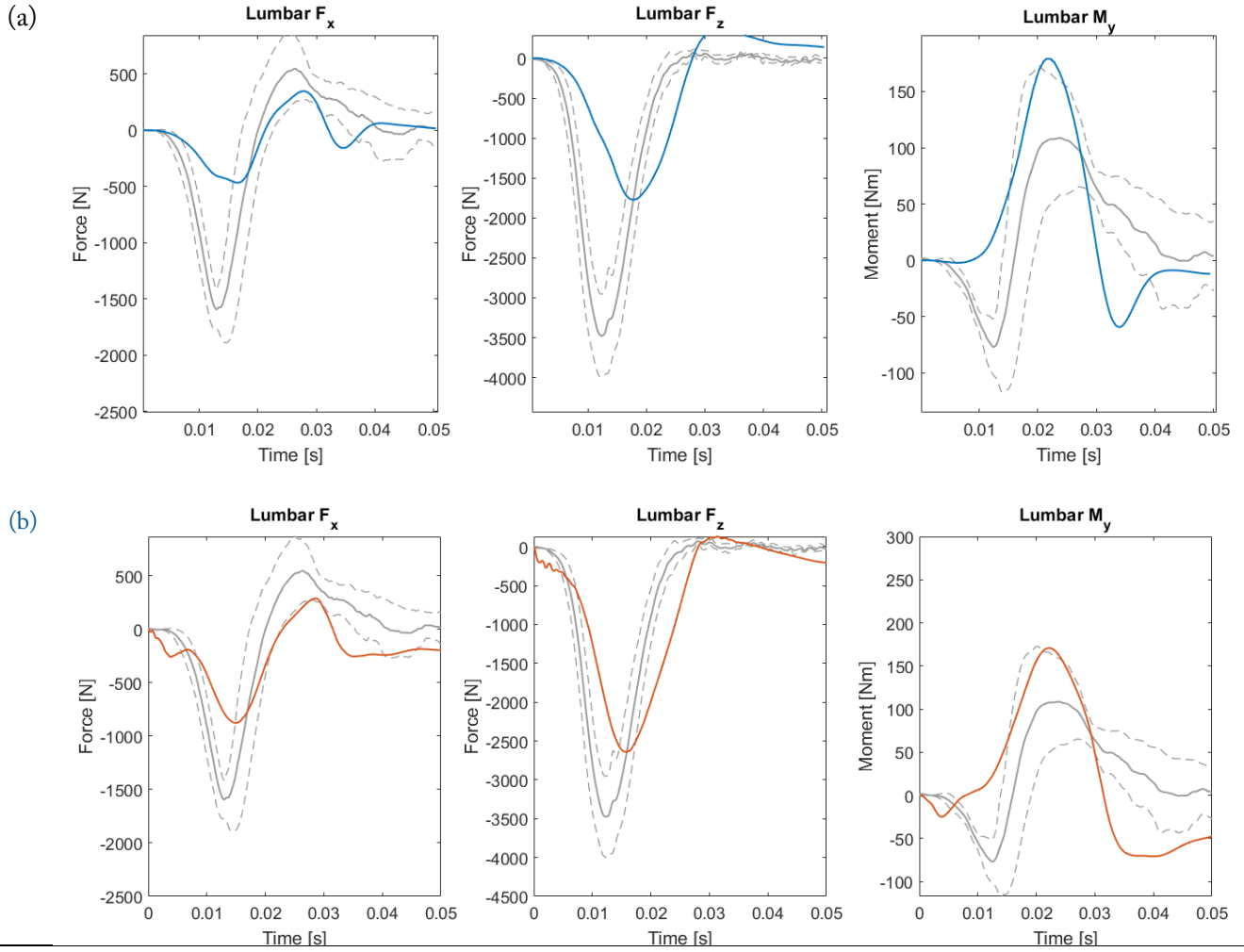


Figure 52. Comparison of GHBMC model before any changes to material properties and geometry (a) and the nominal VIP model (b).

In general, variations of the VIP model were able to simulate the shape of  $F_x$  and  $F_z$  but often missed the trough of  $M_y$ . The different maxima simulated in the nine base case simulations showed significant variation in lumbar forces and moments (see Figure 53).

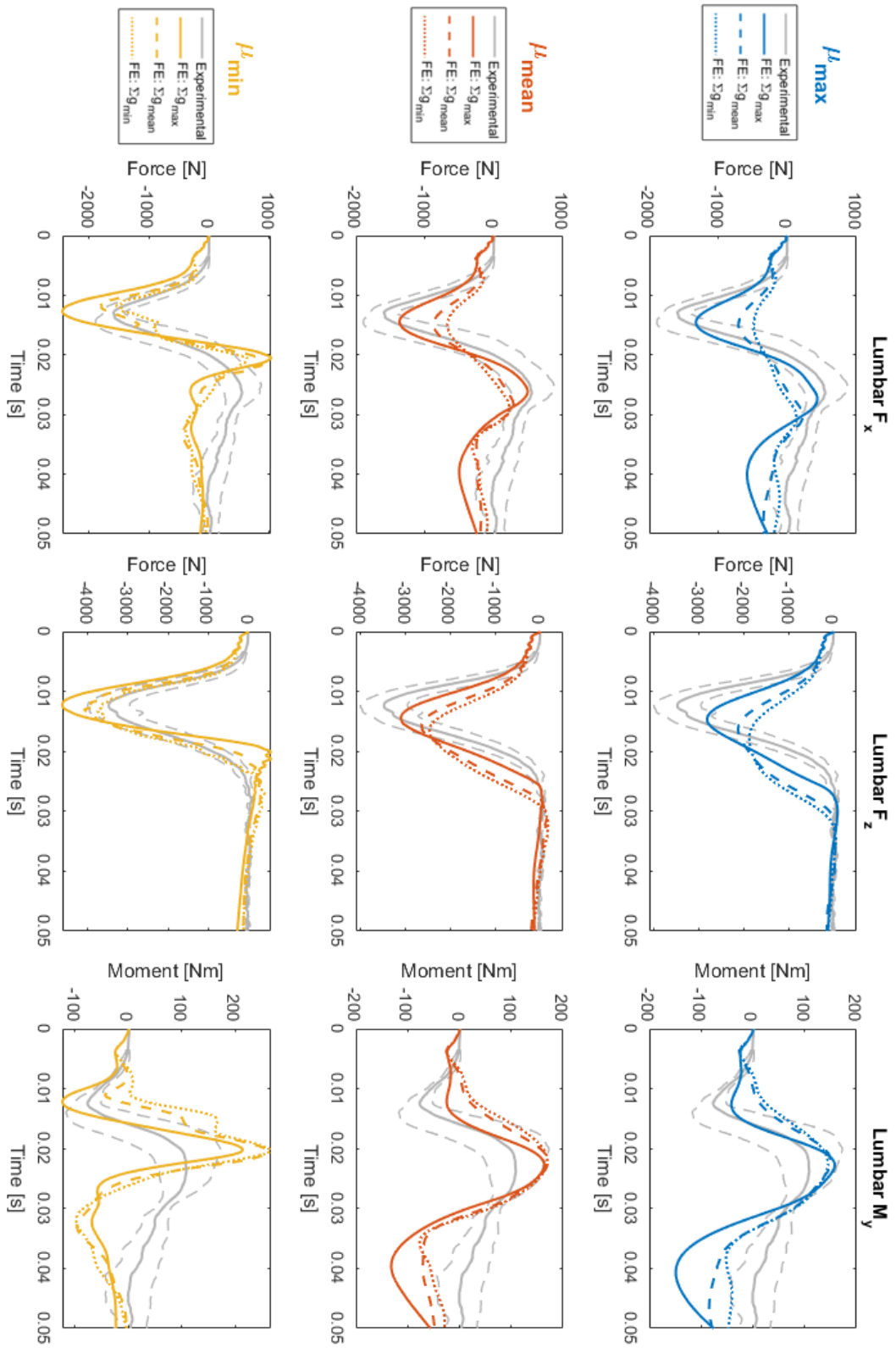


Figure 53. Lumbar force and moment data for the nine base simulations.



Models with a lower shear modulus always had a higher peak force in both the x- and z-directions, and tended to peak earlier, as mentioned previously. In addition, a higher sum shear relaxation moduli resulted in higher peak forces and also peaked earlier. According to the comparison metrics, the model with the minimum shear modulus and minimum sum shear relaxation moduli scored the best in both x- and z-direction forces. In the x-direction, 47.7% of its curve was in the corridor and scored a 0.744 aggregate CORA score, and 46.7% of the force in the z-direction was in the corridor with a 0.742 CORA score. Meanwhile, the nominal model was only 33.7% and 19.8% in the corridor for x- and z-directions, respectively, and scored 0.667 and 0.592 for CORA. This shows that the stiffness of the tissue plays a significant role in both load transmission and loading rate into the pelvis. Phasing was an issue for the maximum and mean shear modulus simulations, which all peaked several seconds after the experimental did. On the other hand, the minimum shear modulus simulations peaked and troughed too early for  $F_x$ , but matched  $F_z$  well, and therefore scored high on the phase component of CORA.

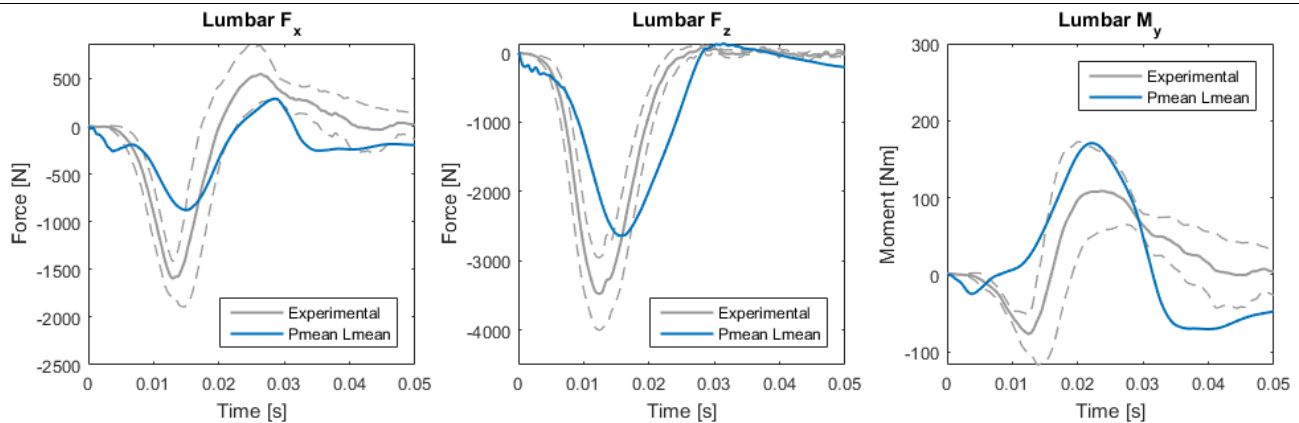


Figure 54. Of the nine base simulations, the nominal model did not compare the best to the experiment data.

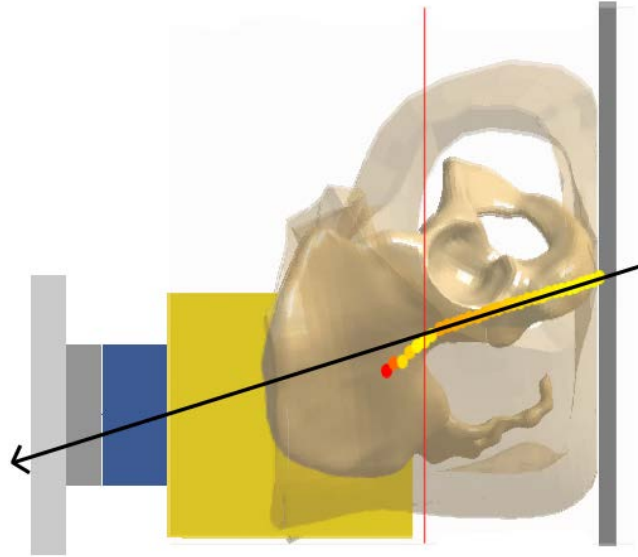
There was even more variability, however, in the y-moment. As mentioned, many variations did not quite capture the trough seen in the experimental data. In general, the higher the shear modulus and the lower the sum shear relaxation moduli, the less the y-moment captured the shape of the experimental data. While the simulations with the minimum shear modulus tended to match the trough the best, the peak was

sharper, and did not extend out farther like the other simulations. The simulation that spent the most time in the y-moment corridor was the Pmax\_Lmin model with 37.3%. It also scored the highest CORA with 0.642. The nominal model, meanwhile, was only 25.3% in the corridor with a CORA of 0.549. For  $M_y$ , the phase tended to be the worst scoring, with size scoring poorly to moderately and the slope scoring relatively high.

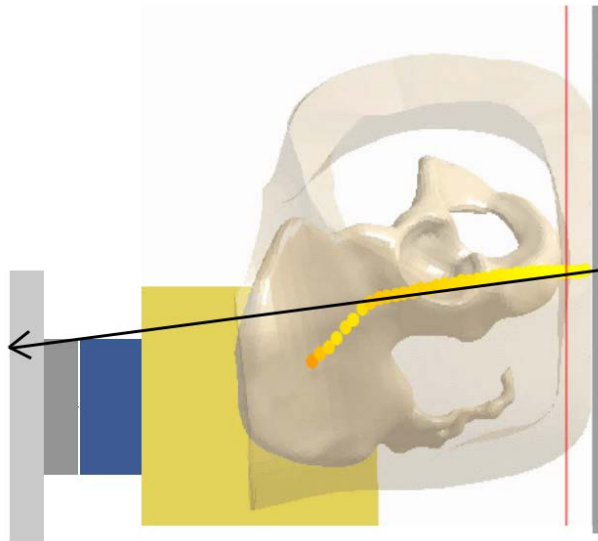
The reason many of the simulations were unable to recreate the trough of  $M_y$  is related to the load path through the tissue (see Figure 55). Recall that the vertical axis in these visualizations represents the x-axis location of the average force through each vertical cross section positioned along the horizontal axis. Comparing a simulation that was able to recreate the trough, Pmin\_Lmax, and one that was unable, Pmax\_Lmin, showed significant differences in the average load path through the pelvis. These visualizations were compared at 12 ms, which was the timing of the trough in  $M_y$ . Looking at the notional slope line in Figure 55a for Pmin\_Lmax, it has a much steeper slope than Pmax\_Lmin shown in Figure 52b. Since  $M_y$  is measured at the center of the lumbar load cell, it has a long moment arm from the application of force. As seen from the notional slopes, a large portion of the load for Pmin\_Lmax creates a moment arm below load cell center. The opposite is true for Pmax\_Lmin which has a flatter line that creates a positive moment arm. This assertion holds for all nine base cases in which the slope of the force path correlates with whether the simulation captures the trough of  $M_y$  and how well it captures it (see Figure 56. This phenomenon also occurs in the peak following the trough in the  $M_y$  trace for the Pmax\_Lmin simulation. Once the moment start going positive, the load path flattens out and starts to create a positive moment, matching the positive  $M_y$  portion of the trace. This analysis shows that the general forces and moments in the pelvis cannot be approximated by any static method. The tissue significantly affects not only the magnitude of force entering the pelvis, but also the direction of the loading through the pelvis over time.

---

(a)



(b)



---

Figure 55. Notional slopes of the force transmission through the pelvis for the Pmin\_Lmax (a) and Pmax\_Lmin (b) simulations at 12 ms. The Pmax\_Lmin had a much flatter slope leading to a positive moment arm about the lumbar load cell.

---

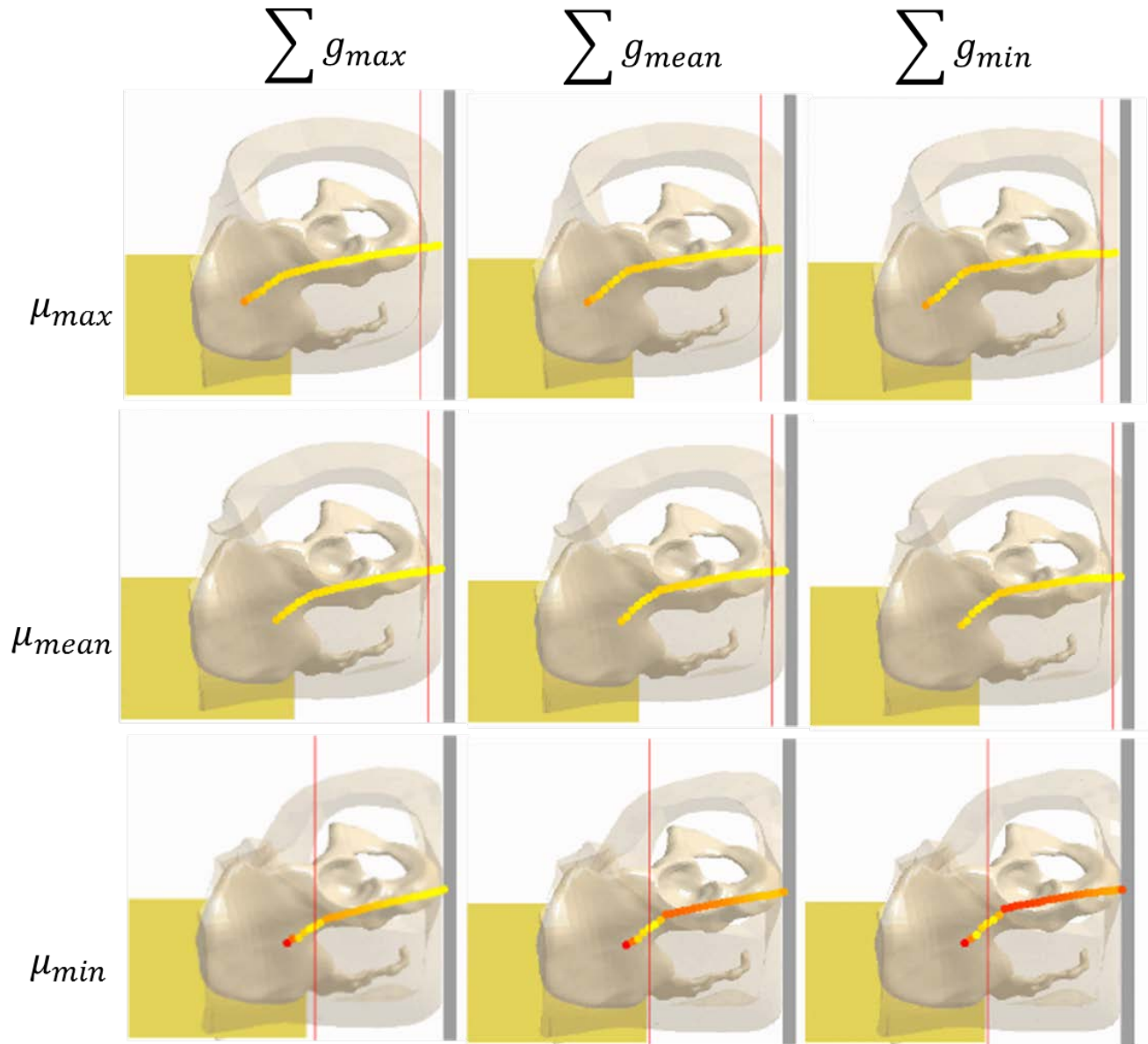


Figure 56. The slope of the load path is associated with how well the simulation captures the shape of the  $M_y$  trace.

In a more quantitative explanation, the ratio of peak  $F_x$  and  $F_z$  correlates with the shape of the  $M_y$  trace.  $F_z$  creates a positive moment about the center of rotation—the SI joint—because it is above the center of rotation as shown in Figure 57a. However,  $F_x$  is first negative which creates a negative moment, and then changes positive, which likewise creates a positive moment. The overall moment is the sum of the moments created by all the forces in the x-direction and z-direction. If the negative part of  $F_x$  creating the negative

moment is much smaller than the positive moment created by  $F_z$ , then the moment created by  $F_z$  will dwarf it and the moment will be positive. Therefore, a higher ratio of  $F_x$  to  $F_z$  will yield a higher  $M_y$ .

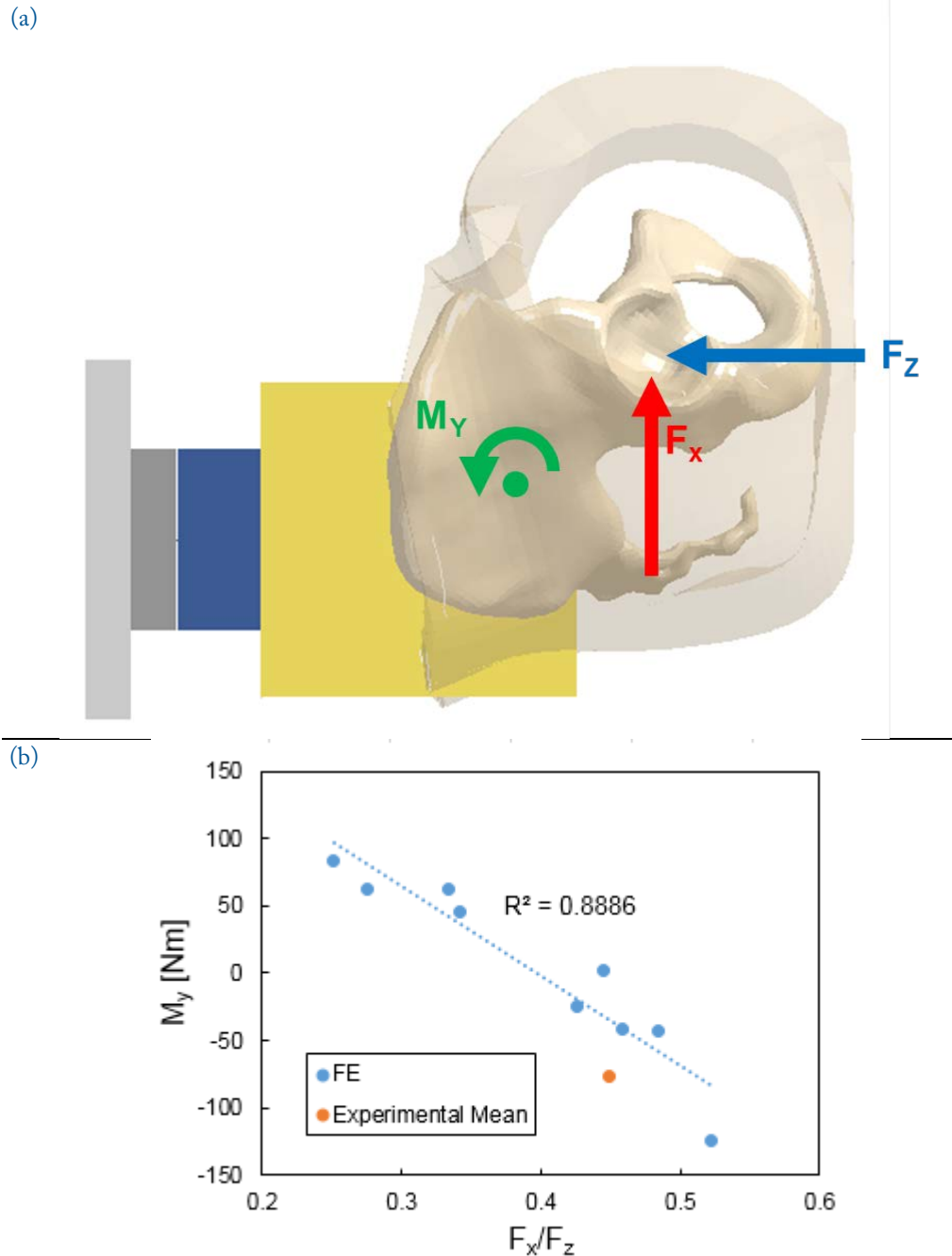


Figure 57. Forces in the x- and z- direction can create positive or negative y-moments depending on their direction and moment arm about the SI joint (a). A higher  $F_x / F_z$  ratio at peak loading leads to a more negative  $M_y$  (b).

This phenomenon was seen in the base FE simulations (see Figure 52b). There was a linear trend between the  $M_y$  and the  $F_x/F_z$  ratio that had an R2 value of 0.89. How close a simulation was to the experimental test in this comparison was likewise correlated with the slope of the line shown earlier in the load path images. A flatter slope meant that the  $F_x$  component was smaller relative to  $F_z$  and therefore completely missed the negative part of the  $M_y$  trace seen in the experimental data. A higher slope from the SI joint to the ischium showed the opposite and was able to better replicate this.

While it is not exactly clear why the difference in tissue material property changes the ratio of forces in the x- and z-directions, there also appears to be a trend in how much load is carried by the tissue. The stiffer tissue (higher shear modulus) carries more load and therefore changes where that point of average force is along the x-axis. Using the same example as before, Figure 59 shows the difference in load being carried by tissue versus bone in the Pmin\_Lmax (a) and Pmax\_Lmin (b) simulations. The soft tissue in the Pmin\_Lmax case is carrying an average of 18.1% of the total load 12 ms into the simulation, while 31.3% of the load is being carried by soft tissue in the Pmax\_Lmin case. While this trend was obvious in the difference in shear modulus, it did not seem to extend to models with the same shear modulus and different shear relaxation moduli. For example, the Pmean\_Pmin saw 25.3% of tissue carried by the soft tissue compared to 26.3% for the Pmean\_Pmax model.

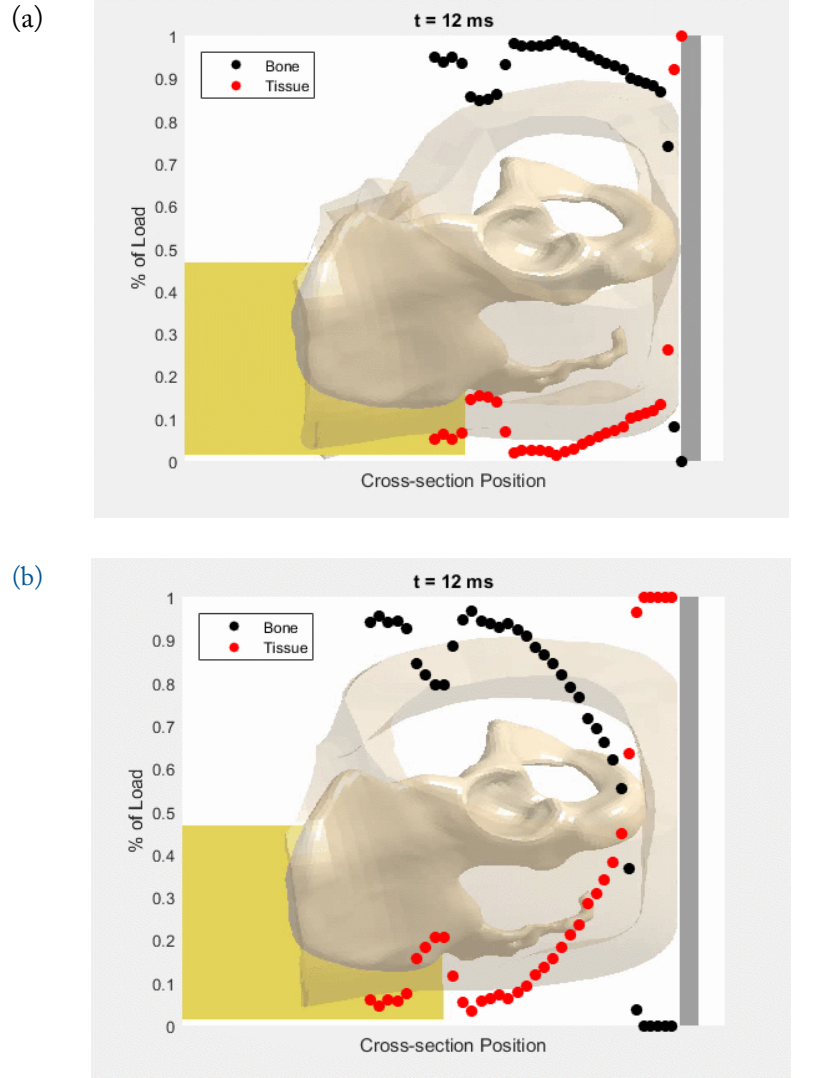


Figure 58. Comparison of load being carried by bone and tissue in Pmin\_Lmax (a) and Pmax\_Lmin (b).

The thin model overall improved the base model in both the x- and z-forces, but still failed to capture the y-moment (see Figure 59). The peak values and shape scored very high in the CORA scores for the x- and z-forces, but spent little time in the corridor due to being out of phase. Because of that, only 38% of the lumbar x-force was in the corridor, and 18% for the z-force, leading to 0.731 and 0.458 CORA scores, respectively. The thin model also completely missed the trough seen in the experimental y-moment and instead had a small peak in positive moment before ascending to the large peak moment, something that was not observed in the base simulations. Despite missing a lot of the shape seen in the experimental data,

32% was within the corridor. At peak loading, the soft tissue in the thin model carried only 19.4% of the total load, compared to 25.6% of the nominal model.

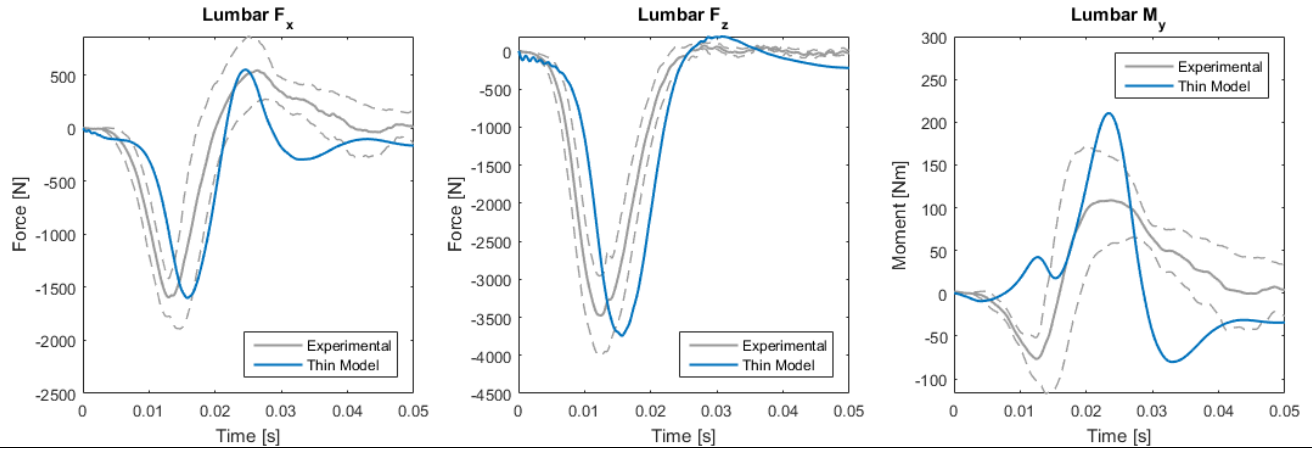


Figure 59. Force and moment results from the thin model.

Changing the material properties of the SI joint also showed to have an impact on the force and moment response (see Figure 60). Stiffening the SI joint resulted in a lower peak  $F_x$ , higher  $F_z$ , and higher  $M_y$ . The shape and phasing of the forces did not change much, but the y-moment did see significant change. The trough was barely seen, but was significantly more than the stiffer SI joint properties. This led the looser SI joint model to be in the corridor a little more than 10% more than the nominal model and be scored nearly 0.1 higher on its CORA score, mostly due to its better phasing and size.

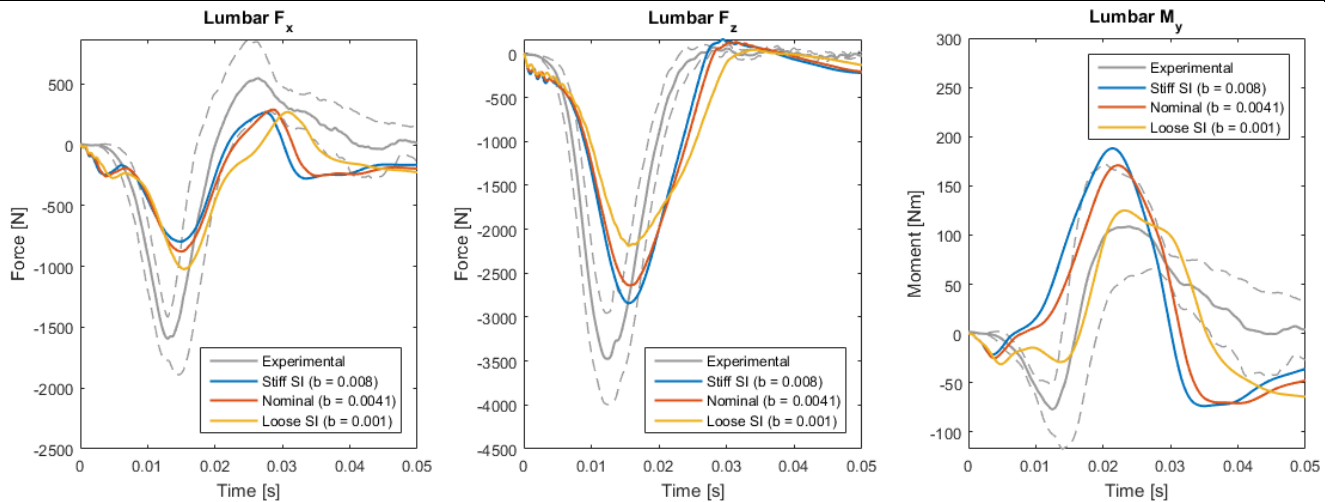


Figure 60. Force and moment results from the change in SI joint properties.



The GHBMC tissue simulation scored similarly or slightly better than the nominal case (see Figure 52). The lumbar  $F_x$  had a slightly higher peak than the nominal case, but also did not follow positive portion of the trace, adding a small hump not found in other simulations. The GHBMC simulation was in the corridor nearly 30% more than the nominal case and had a CORA score of 0.738, up from 0.667 in the nominal case. The size and shape was very similar to the nominal case for  $F_z$ , but also had a closer peak to the experimental data. The corridor and CORA scores were only slightly better than the nominal case. The nominal case, however, scored better for  $M_y$ , with the GHBMC about 10% less in the corridor, a CORA score of about 0.05 less than nominal and also did not capture the shape of the experimental curve by missing the trough and returned to zero much faster than experimentally. Overall less load was carried through the soft tissue in the GHBMC model. During peak loading, the soft tissue carried only 18.3% of the load, compared to 23.0% carried in the nominal model.

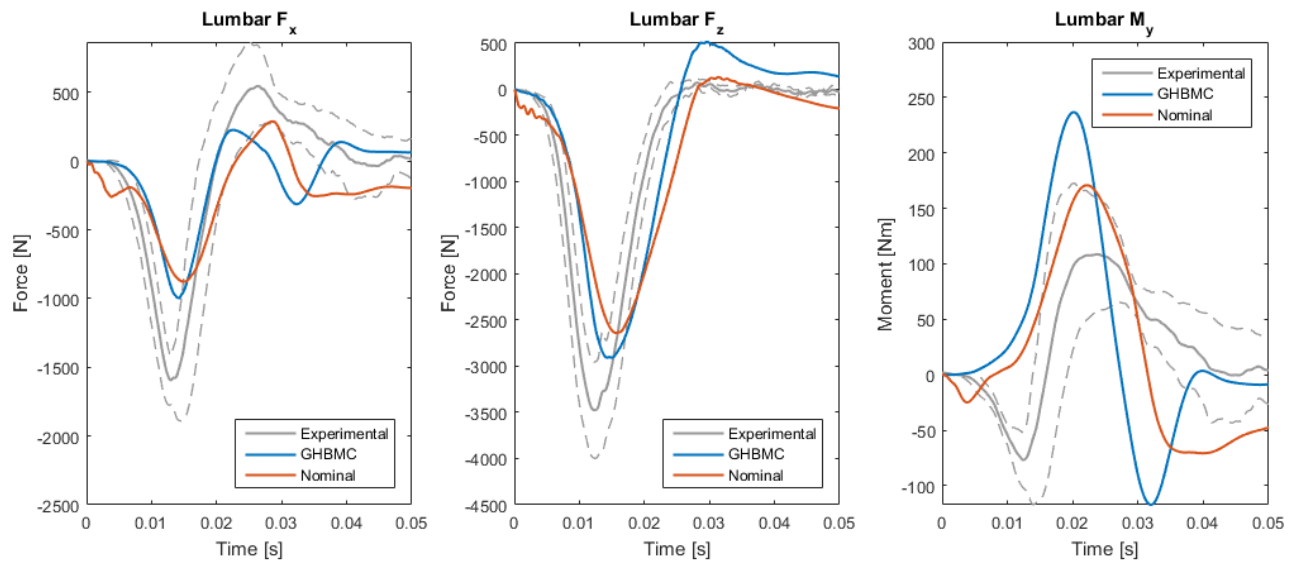


Figure 61. Summary of the GHBMC tissue forces and moments compared to the nominal case.

As expected, a higher rate led to higher forces and moments and vice versa (see Figure 52). Forces in the x-direction were over twice as high in the nominal as the low rate model and were also over twice as high in the high rate model as the nominal. A similar trend was seen in  $F_z$  and  $M_y$ . The higher and lower rate

models generally kept a similar overall shape as the nominal model, albeit with a different frequency. However, rate seemed to have no effect on capturing the trough of the y-moment.

The hypothesis of this thesis was that at higher rates, soft tissue stiffens up and carries more load than a relative lower rate. However, this was not seen in these different rate models. It was found that at peak loading, there was little difference in amount of load carried by bone and soft tissue between the models. In fact, the low rate model had the highest percentage carried by the soft tissue: 24.4% for the low rate, 23.0% for the nominal, and 22.6% for the high rate. Because the difference was so low, an even slower model was run that was ten times slower of an impact than nominal (280 ms load time) and found that 28% was carried by the tissue, continuing this trend.

However, it is important to note that the higher impact compresses the tissue more and therefore there is less physical tissue that can carry load. For example, 51.9% of the total load carried by the tissue is carried in the tissue in between the ischium and impact plate in the nominal impact simulation. While this is definitely one of the most important impact points in the model, the hypothesis of this thesis was that tissue carrying load could change the load path by changing the location of the average force. Since the soft tissue between the ischium and the impact plate will always take 100% of the load since it is all tissue, a closer look at the tissue outside of that area is needed. Excluding the tissue between the ischium and the impact plate, only 13.4% of the load was carried by soft tissue in the nominal model, compared to 13.5% in the high rate model and 14.6% in the low model.

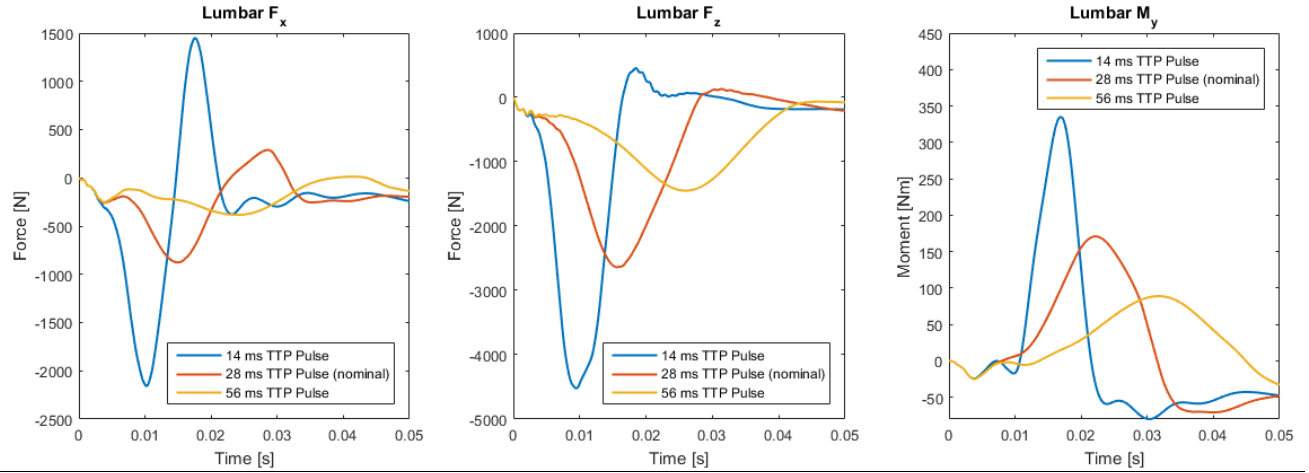
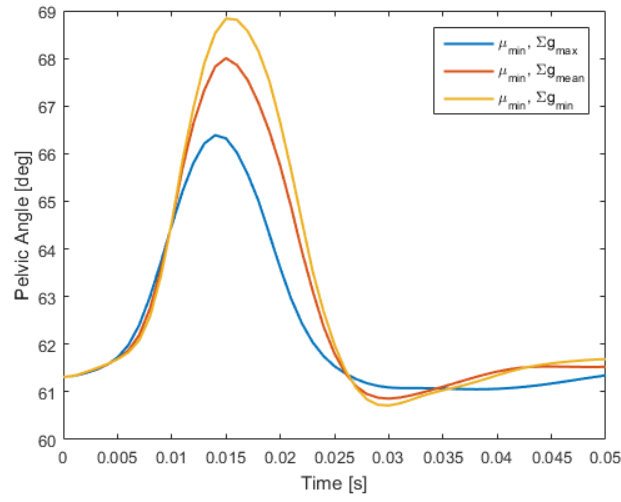


Figure 62. Comparison of forces for different loading rates of the Pmean\_Lmean model.

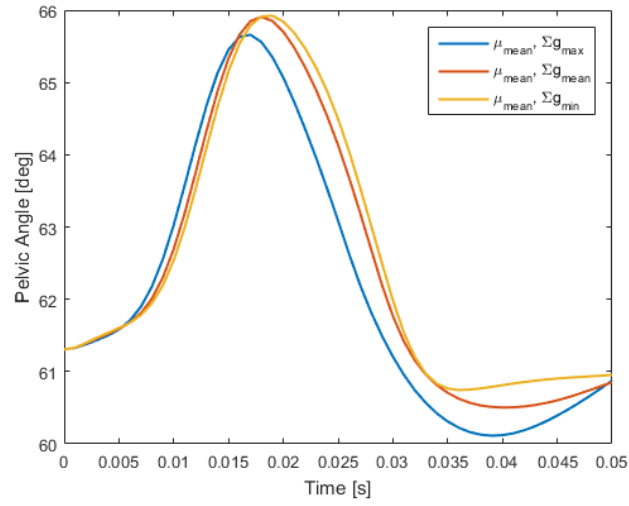
### 5.3.4 SI Joint Rotation

While the rotation about the SI joint was not measured in the experimental data, this data was still used here to compare various effects on the amount of rotation seen in the pelvis. The rotations for the nine base simulations can be found in Figure 63. The nominal model rotated to an angle of  $66.0^\circ$ , or a total of  $4.6^\circ$ . Decreasing  $\sum g_i$  barely changed the total rotation, and increasing  $\sum g_i$  only decreased the angle by half a degree. Changing  $\sum g_i$  also barely changed the rotation for models with the maximum shear modulus, but the minimum shear modulus saw a little more change with the  $\sum g_{min}$  model rotated  $7.5^\circ$  and  $\sum g_{max}$  rotated  $5.0^\circ$ .

(a)



(b)



(c)

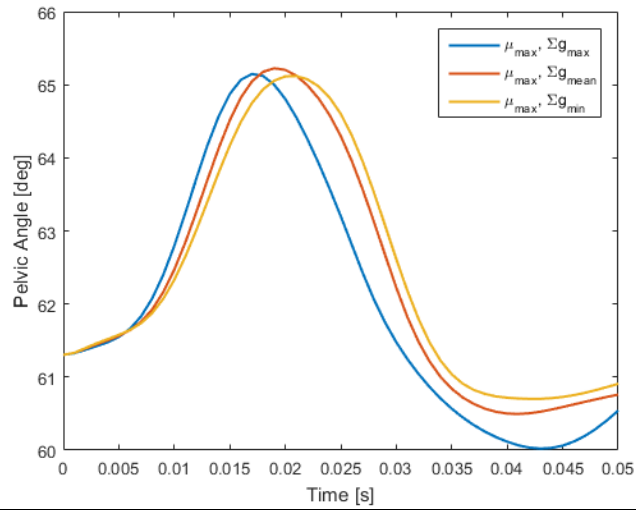


Figure 63. Rotations about the SI joint for the nine base simulations.

The thin model rotated  $5.4^{\circ}$ , about a degree more than the nominal model. The GHBMCM rotated about half a degree less than the nominal model. Surprisingly, a change in SI joint properties did not change the rotation as much as initially thought. The loose SI joint model only rotated  $0.6^{\circ}$  more than nominal, and the stiff SI joint model  $0.5^{\circ}$  less. The beams that represent the ligaments of the SI appear to have little effect on the overall rotation of the pelvis, as changing the stiffness of the beams by orders of magnitudes brought fractions of degrees of change in rotation.

The change in rotation does not appear to be correlated with change in ratio of forces in the x- and z- directions. Since the origin of the load path is mainly at the ischium and travels to the sacral ala, if the pelvis would have rotated significantly, it is possible that a difference in balance of forces would be seen, but with such small changes in SI rotation, no trends were observed to correlate the two.

### **5.3.5 Coccyx Loading**

Due to the geometry of the sacrum in the VIP model, the sacrum and coccyx were never directly loaded from the impact plate. As seen from the load path through the pelvis, the natural progression of loading passes primarily through the ischium toward the iliac wings and through the sacroiliac joint and into the sacral ala (see Figure 52). A question related to the thesis was whether the tissue stiffened up sufficiently to transfer load to other places other than just the ischium. With close proximity to the loading, the load share of the coccyx was investigated. The load of the coccyx and the sacrum inferior to the SI joint were compared to determine how much load was coming through the sacrum via the impact plate, rather than through the SI joints. The percent load of the coccyx was shown relative to the total amount of load carried by the bone. Each percent represents the coccyx's load in a specific vertical cross-section.

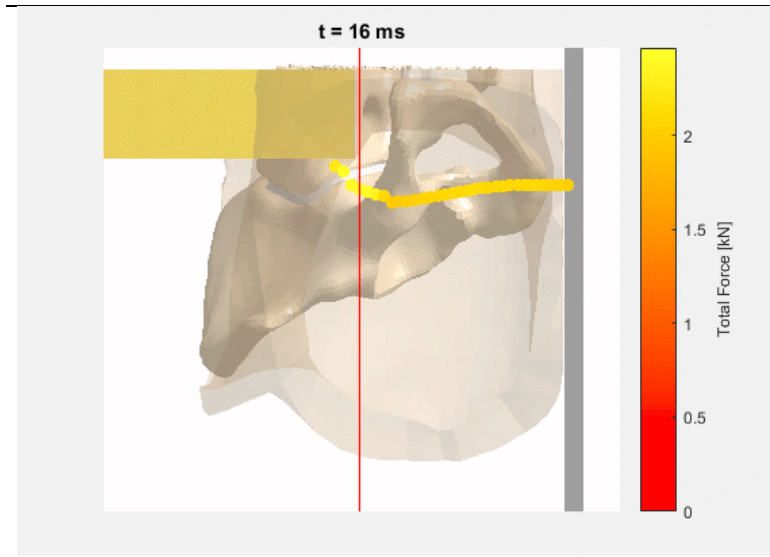


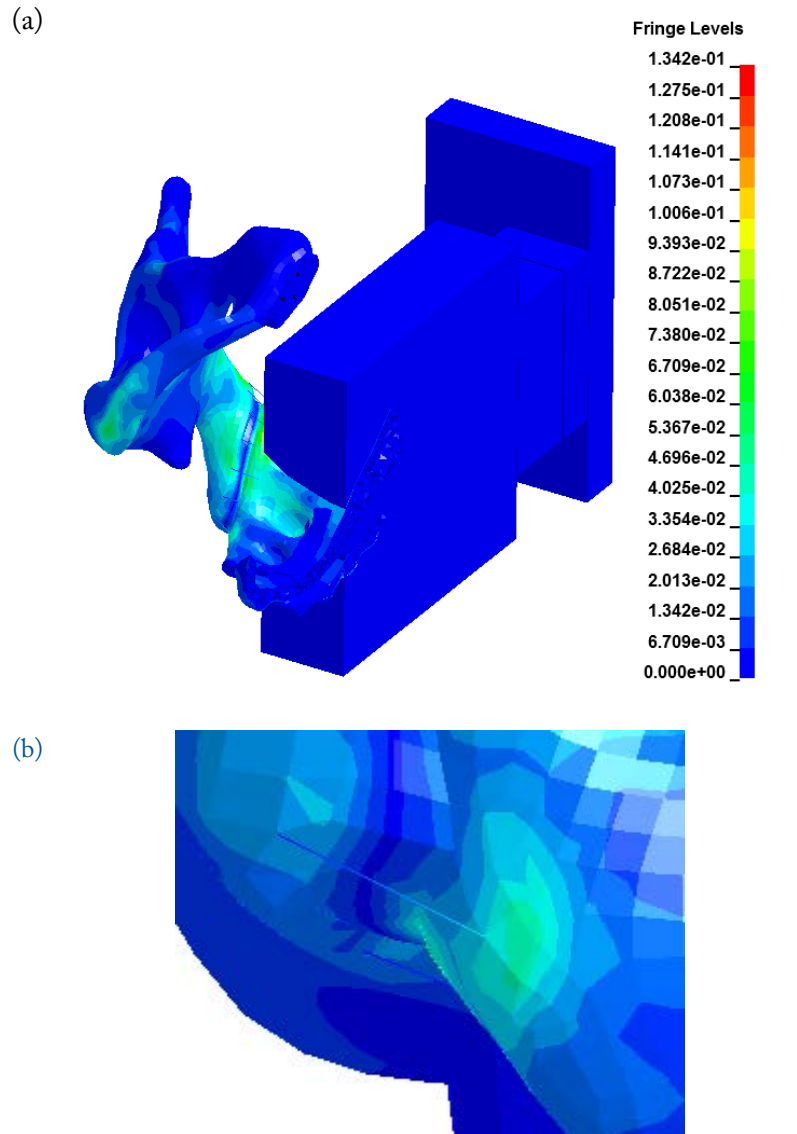
Figure 64. Typical load path seen from the anterior-posterior view in the nominal model.

In general, only small changes were seen between different tissue stiffness. The nominal model saw about 2% of total load through the bone coming through the coccyx and increased to about 5% just inferior to the SI joint. Changing the  $\sum g_i$  for the mean shear modulus did not significantly change the total load carried through the coccyx and sacrum. The models with the higher shear modulus saw about a 1% increase in load carried near the SI joint. The low shear modulus models had the highest spread of load carried by the coccyx ranging between 1% and 3% for the minimum  $\sum g_i$  and between 1% and 10% for the maximum  $\sum g_i$ .

However, it is important to note that on some models, the ligament beams surrounding the SI joint artificially increased the stress in the area immediately inferior to the SI joint (see Figure 65). This stress concentration was more apparent in some models than others. For example, some of the low shear modulus models had elements that had reached maximum strain and had been deleted to show a fracture had happened. This was more apparent in the higher impact conditions, but even in some of the nominal impact conditions, a few elements were affected and all were adjacent to where these beams inserted into the sacrum.

The models seen with a higher force carried by the coccyx were also the models that tended to fracture during impact, indicating that the models with these stress concentrations are over-indicating how much load is actually coming from the coccyx into the sacrum. A high percentage was also seen in the GHBMC model (1–10%), which had similar fracturing problems as the low shear modulus cases.

This indicates that the upper end of this carrying load is an over prediction and that in this case, the coccyx carries little load from impact. However, this is very dependent on geometry and posture. As mentioned in the development of the VIP model, cases were tested in a more reclined posture. This led to direct loading of the posterior side of the sacrum and coccyx and led to massive fracturing of the sacrum in precompression well before the impact of the plate. It was also seen in the pelves for the experimental UBB tests that there was significant variation in sacrum/coccyx length between specimens, and, depending on posture and length of the sacrum/coccyx, it is possible that in certain conditions a load path could occur during loading.



---

Figure 65. Von Mises stress of the pelvis (a) with a close-up view of the ligament beam creating a stress concentration on the bone (b).

---

## 5.4 Discussion

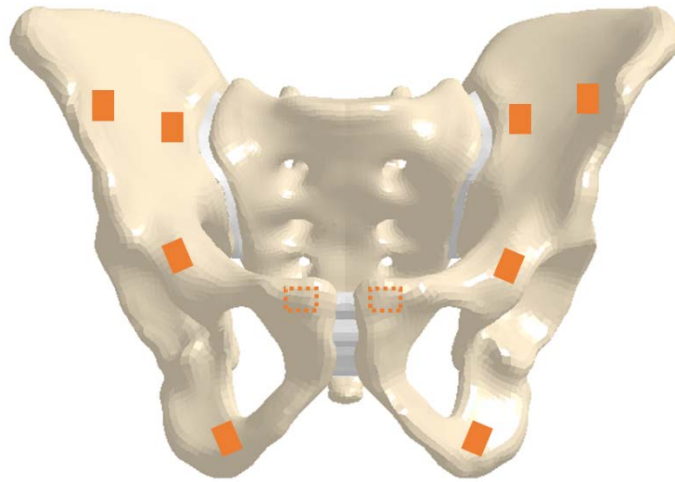
### 5.4.1 Fidelity of the VIP Model

There were many modifications made to the VIP model to make it as similar as possible to the pelvis in the UBB experimental tests. The tissue was reshaped to match mass and, to an extent, shape, the pelvic angle was updated, the sacrum was positioned accurately in the pot, organs were removed and back filled with extra mass representing the gel insert, and a more realistic friction component was added. Despite all



this, as seen from the results, the VIP model does not perfectly match the experimental data, and in fact, the original tissue model appears to simulate the experimental data better. However, there are many parts of the pelvis model that have shown to still be inaccurate and not validated. If these other parts were fixed and modelled more accurately, it is expected that the original tissue model—the stock GHBMC material model—would overestimate the force, as explained in the following section.

The perhaps most obvious is the shape of the tissue. Even though the thigh portions and superior portions of the tissue were trimmed, it still does not perfectly resemble the tissue distribution found experimentally. The base of the VIP model is the GHBMC model, which is a seated occupant model. Therefore, the tissue distribution in the VIP resembles that of a sitting posture, which can be very different than other postures (see Chapter 2.2). Even though the thigh portions were removed, the rest of the gluteal tissue is still in a state in which it is being pulled from the buttocks to underneath the ischium, as it would in a seated posture. On the contrary, the experimental pelvises were not prepared in such a way to preserve a seated posture. The pelvises were taken from supine PMHS, and some of the tissue was disturbed to accommodate instrumentation for the tests. For example, strain gauges were placed on the anterior facing side of the ischium, among other locations (see Figure 52). While the immediate tissue anterior to the ischium was avoided during the attachment of the strain gauges, the location is nonetheless in close proximity to the ischium and required scraping muscle attachment to accommodate the gauges. Other strain gauges and other instrumentation such as mounts for accelerometers on the pubic rami disturbed other areas of tissue on the pelvis. In addition, the removal of the femurs from the pelvis disturbed some of the tissue adjacent to the acetabulum, before the tissue was sutured back together to enclose the pelvis.



---

Figure 66. Locations of strain gauges on experimental UBB pelvis.  
Dotted lines indicate gauge locations obscured by view.

---

The combination of all these things makes the attachment of the tissue to the bone in the VIP model exaggerated. The inner layer of tissue elements in the VIP model is a layer of tetrahedral elements which shares nodes at the boundary between the cortical bone of the pelvis and the pelvis tissue. In reality, there should be more sagging tissue that is less connected to the bone in many places. This difference would change how load is distributed in the VIP model.

While no tissue measurements were taken while the experimental pelvis were in precompression prior to impact, pre-test CT scan measurements were analyzed to measure thickness of the unloaded tissue under the ischium perpendicular to where the impact plate would contact. The nominal VIP model had an unloaded ischium tissue thickness of 58 mm, compared to an average of 42 mm measured from the experiments. The thin model tissue thickness had been reduced to 40 mm to match the experiments, and made a substantial difference in terms of the response of  $F_x$  and  $F_z$ , although the response of  $M_y$  became worse in comparison. Even though the overall shape of the tissue is still not completely right, the thin nominal model showed that the thickness of the tissue makes a significant difference in the force response.

Other material models used in the VIP model were not validated for high rate impact. The GHBMC pelvis used material properties from work done by Anderson et al., which tested a 68-year-old female pelvis in quasi-static lateral loading through the acetabulum [76]. A subject specific model was created with geometry and cortical bone thicknesses from CT. Strain gauges were used to record strains in the bone while loaded. While using this model may be sufficient for use in automotive side impacts, these material properties are not appropriate for high-rate vertical loading.

In addition, the sacroiliac joint material properties were not realistic for this scenario. The SI joint in the VIP consisted of a rubber material model making up the cartilaginous joint, with beam elements representing the ligaments that support the SI joint. Even in the nominal loading rate, some element deletion due to exceeding strain thresholds occurred. This was most notable in the low shear modulus and GHBMC tissue case tests. There was no evidence in the UBB experimental tests that there was any injury or fracture at this low of an impact rate. While it was usually only a handful of elements exceeding the strain limit set in place, it shows that the model is not correctly tuned for higher impact tests (see Figure 67a).

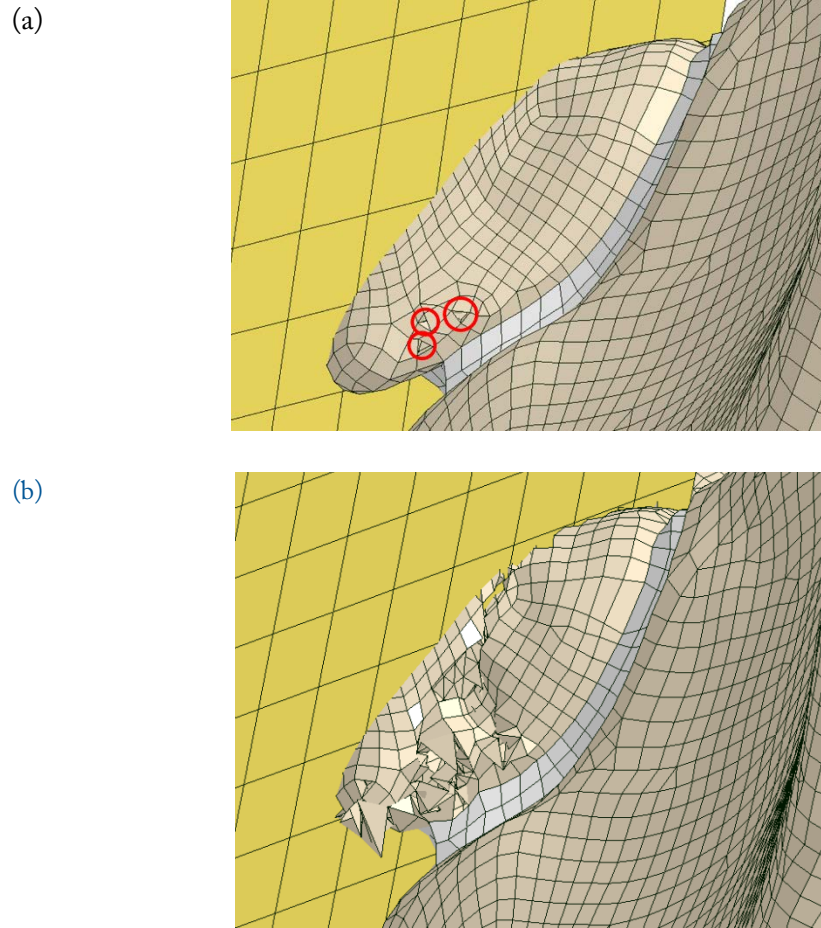


Figure 67. Element failures in the nominal (a) rate and higher rate (b) loading.

The higher rate loadings resulted in more catastrophic failure in the sacral ala (see Figure 67b). While these higher rate loading cases were exploratory in nature and not validated to experimental tests of this load rate, it is unlikely that this level of fracture would occur in this loading scenario. As explained in Chapter 2.6, additional tests were performed at higher velocities following the initial 2 m/s impact. Each subsequent test with a faster impact was followed by an additional 2 m/s impact that could determine if any gross injury had happened by comparing the data from the different 2 m/s impacts. While this method did not have any absolute certainty in identifying injuries, no observable injuries were reported from the 2 m/s impact or any impacts with similar loading as the high-rate loading performed on the VIP model. From these results, given the loading scenario, it is unlikely that a failure would have occurred. Therefore, the material properties for the SI joint and the bone in the sacral alae are not accurate for this impact rate.

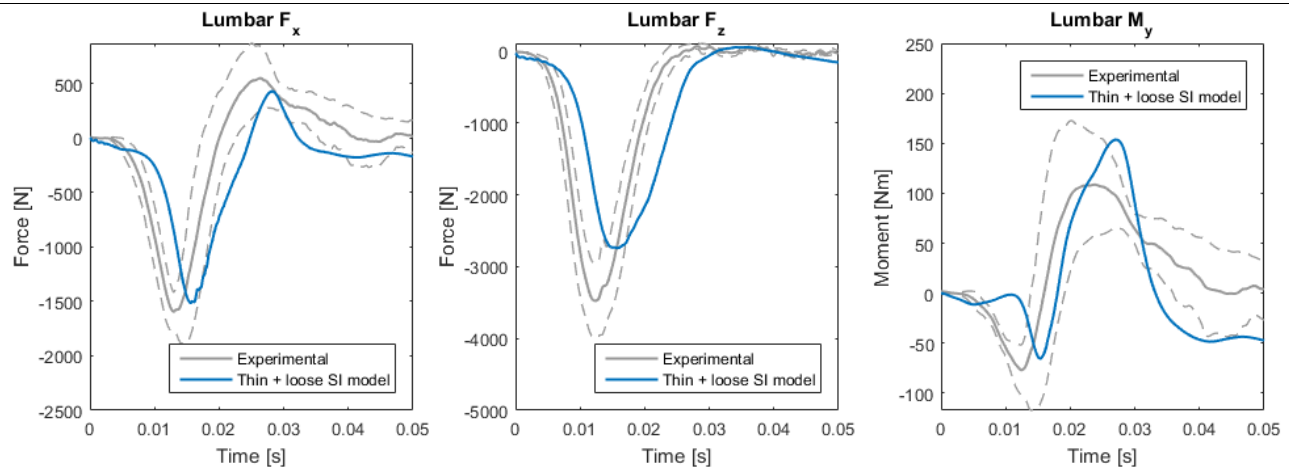


Figure 68. Model with both the thin tissue and a looser SI model shows an example of a combination of effects that could make the model more biofidelic.

In reality, it is a combination of many factors that will make this model more biofidelic. Figure 68 shows an example of mixing the thin model with a model with a modified SI joint to get a model that had the highest average CORA score between all three channels. While the original tissue model—the GHBMC tissue model—matched the experimental curves better than the tissue model created in this thesis, it would be expected that once all aspects of the pelvis model are changed to become more biofidelic the GHBMC model would be an over-prediction of the forces and the moments in the model, and that the tissue constitutive model created here would be a better predictor. This is easily seen if the GHBMC model is used to try to fit the tissue models; it grossly over-predicts the actual force by almost an order of magnitude (see Figure 69). Because the tissue only carries a portion of the load in the VIP model, the over-prediction of force in the GHBMC model is less pronounced. This was also apparent in the VIP model before the thigh portions were removed. In this case, however, it under predicted the experimental data and the new tissue model because the tissue was overall stiffer, and there was so much more tissue that it did not compress nearly as much, leading to lower forces.

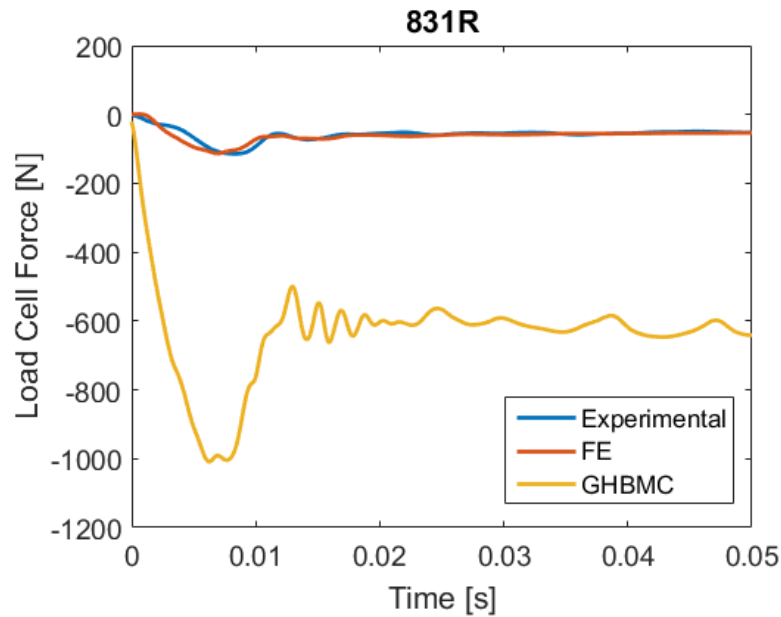


Figure 69. The GHBMC tissue material model grossly over-predicts the load cell force seen experimentally.

#### 5.4.2 Load Path

The hypothesis at the beginning of the thesis was that when subjected to a higher loading rate, tissue stiffens up more and carries more of the load relative to a lower loading rate. The comparison of the different impact rates in the nominal model showed a negligible amount of change in the amount of the total load that is carried by the soft tissue.

However, there are some caveats to this finding. First, the tissue material model created in this thesis was formulated to match the nominal impact loading found in the experimental UBB test data. While this material model is likely a decent approximation for impact rates higher than what was tested, without validation of higher rate testing, the fidelity of this model at higher impact rates is uncertain. As mentioned previously, some of the material properties of the VIP model are not suitable for high acceleration vertical impacts. This was apparent from the fracturing of the sacral ala before the maximum bone strain limit was

increased to prevent fracture. So while the tissue was not seen to carry any significantly different amount at different loading rates, it is uncertain how these factors affect this finding. It is also possible that the difference in impact rate between the models was not large enough and tissue may not be sensitive enough to see this difference.

Despite this inconclusive finding, other aspects of the tissue were found to have major effects on the load path and the loading response in general. Many of these aspects are intertwined and hard to pinpoint one thing directly causing another. It was shown that the ratio of forces in the x-direction to those of the z-direction had a significant effect on the shape and magnitude of the y-moment by changing the moment arms about the center of rotation at the SI joint. It is ultimately uncertain why a different stiffness causes a different ratio of forces, or if the other changes brought about by a difference in stiffness are what are causing the change in force ratios. Changing the stiffness of the tissue also changed how much the tissue is compressed, as well as how much load was being carried by the soft tissue. Changing the thickness of the nominal model to be about one-third thinner without changing any other material properties also changed the ratio of forces and how much load the soft tissue carried. The stiffness of the SI joint also had an effect. Stiffening the SI joint increased the force in the z-force and y-moment, but decreased the x-force. The opposite was seen in the looser SI joint and was able to better capture the shape and magnitude of the y-moment.

## **5.5 Conclusion**

In this chapter, the Vertical Impact Pelvis Model was created and was capable of recreating the lumbar load response of the pelvis. This original geometry from the pelvis GHBMC model was used and modified to match input and boundary conditions found from in the experimental UBB pelvis tests outlined in Chapter 2.6. The model was then subjected to different loading rates to see differences in the load path through the

pelvis. It was found that the amount of load carried by the soft tissue did not change with respect to the loading rates used. Following this finding, a sensitivity study was performed to find if other material parameters had an effect on the loading rate through the pelvis. From this, it was found that the stiffness of the tissue, the thickness of the tissue between the ischium and the impact plate, and the sacroiliac joint properties all had an effect on the load path through the tissue. The change of the load path was evident through the slope of the load passing through the pelvis from ischium to the iliac wing. The slope of the load was correlated with the lumbar moment response. The nominal model was unable to recreate the first negative moment peak, but it was seen that different load paths through the pelvis were capable of recreating this shape in the moment trace. Some of these properties also affected how much load was carried by the soft tissue in the pelvis.

So while the hypothesis to this research was found to not be correct for the loading rates testing in this research, other parameters were found to have a significant impact on the load path through the pelvis. The context of the hypothesis was that different loading rates would affect how much load was carried by the tissue, and that that amount could change how the load traveled through the pelvis. From prior research on how the pelvis is injured during high-rate vertical loading, it was found that a myriad of different injuries can occur, and were thought to be correlated to different loading rates and postures. The findings from this chapter are significant because they help understand different variables that affect this load path. Understanding how the load path travels through the load path in different scenarios is the first step to correlating injuries to different input and boundary conditions.



## 6 Conclusion

### 6.1 Summary

For UBBs and other blunt trauma, the mechanism of injuries to the pelvis are not always understood. Understanding the load path through the pelvis may make the mechanisms of injury more clear. However, finding the load path through the pelvis is not straightforward, as most physical sensors are unable to fully capture load as it is transmitted through the pelvis. Finite element models are useful tools in analyzing load path and injury mechanisms, but the analysis is only as good as the model. Current finite element models lack high rate material properties, and therefore lack the sensitivity to analyze vertical impact scenarios such as UBBs. To better understand the load path through the pelvis during high-rate, axial loading, experiments were performed and a series of finite element models were created.

First, a two-stage drop tower system was created that could consistently indent tissue at a constant velocity. Magnets and custom shaft collars were used as a mechanism to control total displacement and create an approximate step-hold displacement in it does not bounce off the specimen after the indenter reaches the prescribed displacement. A load cell was used to measure the force underneath the tissue specimen, and motion tracking was used to record the displacement of the indenter over time.

To create a constitutive model of the tissue tested in the drop tower apparatus, an inverse finite element method was used. Individual FE models were created for each tissue specimen tested using an Ogden model to capture higher rate properties and viscoelasticity in this tissue. The indentation was prescribed through the displacement over time of the indenter from the experiments. A single shear modulus and a trio of shear relaxation moduli were chosen to represent the constitutive model. An optimization routine was coupled with an IFE process, which recorded the force underneath the tissue, compared it to the respective experimental data, and systematically changed the material properties until the error between the FE load

cell force and experimental load cell was minimized. A nominal model was created by averaging the material constants found from the specimens tested.

Lastly, a finite element model of the pelvis—the Vertical Impact Pelvis model—was created to compare to a series of underbody blast experimental tests performed on PMHS pelvises. The VIP model was based on the GHBMC pelvis and was heavily modified with the updated tissue constitutive model and tissue geometry. To simulate the experimental testing, the sacrum was placed into a pot that attached to a load cell to measure the lumbar forces and moments. The pelvic angle and positioning in the pot were taken from measurements in the experimental tests. A series of tests was performed to examine the changes in the force response due to changes in the stiffness of the tissue, rate effects, thickness of tissue underneath the ischium, and sacroiliac joint properties. The loading rates explored were not found to change how much load was carried by the tissue. However, the stiffness of the tissue was found to change the load path through the pelvis through different ratios of forces in the x- and z-directions. The thinness of the tissue and the SI joint properties were also found to have significant effects on the force response of the tissue.

## **6.2 Contributions**

While static loading is sufficient for many engineering applications, dynamic loading is needed in the field of injury biomechanics to correctly model strain rate dependent materials. Many testing apparatuses used to test compression or tension of materials have certain rate limits and are often too slow to correctly compress materials at the desired strain-rate. This is often because these machines are designed to compress very stiff materials and must be designed to high stress loading. Because of the impact speeds required to reach high strain rates in the tissue for this thesis, a custom compression device had to be designed. Because tissue is much less dense than many other materials, such a device is not needed to withstand high amounts of stress.

The design of the indentation device outlined in this thesis was easily implemented into an existing drop tower setup initially designed for different purposes. The simplicity of this design would allow this method of indentation of soft tissue at high rate to be adapted to other drop tower apparatuses, which are common in biomechanics labs. In addition, this design also allowed for an approximate step-hold compression, which is a sought after technique for biologic tissue because it allows for calculations of tissue relaxation. The simplicity of this design also makes this a relatively inexpensive method to test compression of soft tissues at controlled displacements and constant impact velocities. All parts for this design were either made using a standard lathe and three-axis machining mill, or were commercially available as off the shelf parts.

Prior to the constitutive model created for the gluteal tissue, there was no high-rate compression data available in the literature. Many studies have modeled gluteal tissue for applications anywhere from bed sores to automotive ergonomics. However, these tests were all done at quasi-static rates. In addition, many high rate material models have been created for specific muscles, fats, or skins, but not as a composite sample of soft tissue, much less a composite sample of gluteal tissue.

Finite element modeling is an increasingly common method used in injury biomechanics. The tissue in this thesis was modeled using an Ogden rubber model, a common constitutive model found in most FE software packages. This model can therefore be easily implemented in other FE models for similar uses. In addition, eleven specimens were tested, allowing for analysis of variability of stiffness. This tissue model is not constrained for usage in underbody blast simulations; it can also be used in any high-impact loading to the pelvis, including ejection seat testing, helicopter crashes, and high-rate automobile crashes, among others.

Most available pelvis FE models are used for automotive applications, with others for fields such as comfort, deep tissue injury, and other clinical applications. None of these models have updated material properties for vertical impacts for UBB events. The VIP model created here is the start of a validated model that can

be used for pelvis component testing replicating UBB events. This model was updated with high-rate gluteal soft tissue material properties, and updated tissue geometry and boundary conditions were implemented to replicate a series of existing experimental pelvis UBB tests.

The VIP model significantly increased the fidelity of the model compared to the stock GHBMC pelvis model with no tissue material properties or tissue geometry changes. The VIP model nearly doubled the lumbar response in  $F_x$ , and nearly increased  $F_z$  by 1 kN, increasing the CORA scores of both. The phasing of both also improved, with the peaks shifting about 2 ms closer to the average experimental model. In its current form, the VIP is a significant improvement over the GHBMC stock pelvis model in terms of matching lumbar reaction forces in the UBB pelvis tests.

The improvements to the VIP model enabled a better understanding of the load path through the pelvis. First, the model showed that in the rates tested in this research, the load rate does not significantly affect the load path through the pelvis or how much load is carried by the tissue. Second, through a sensitivity analysis, many factors of this model were identified as influencers on the overall force response of the pelvis during vertical impacts. A set of tools were designed to be able to calculate and visualize the position of average load through the pelvis over time through a series of cross-sections bisecting the VIP model. This concept was used to be able to show the load path through the pelvis in both the lateral and anterior-posterior view in real time. In addition, these tools were applied to calculating how much load was being carried by bone versus soft tissue, as well as how much load was being transferred through the coccyx during impact.

From these analysis, it was found that the stiffness of tissue and the thickness of tissue changed the ratio of forces in the x-direction to those of the z-direction which altered the load path through the pelvis. This ratio had a direct impact on the moment seen on the pelvis. This ratio was visually seen as in the analysis

as taking a different path through the pelvis. For example, between the ischium and the iliac wing, stiffer tissue tended to take a more anterior path through the pelvis, while a less stiff tissue tended to take a path that was more posterior in a more direct path to the SI joint and sacrum.

From injurious datasets of the pelvis in UBB vertical loading, a wide range of injuries have been found. More anterior injuries such as ischial tuberosity and pubic rami fractures were seen, as well as more posterior injuries such as fractures to the SI joint and sacral ala. While the dataset may be able to correlate input and boundary conditions to different injuries, the mechanism of injury may still not be understood. The VIP model and the analysis performed in this research provide a framework to continue researching the mechanisms of injury. While physical testing provides the injury data to certain input conditions, it is difficult to capture load path, stresses, and strains continuously. Finite element modeling is more suited for this.

While the VIP model is currently not capable of predicting injury, it has been shown that it is capable of capturing the load response during non-injurious vertical loading scenarios. In addition, the research performed here found that there were some inadequate material properties of the model. Most notable was the sacroiliac joint and the surrounding bone, which tended to fracture in certain conditions, when fracture was not expected based on the results of the experimental tests. This analysis provided the insight needed for future work to improve this model. With appropriate changes to the model suggested in this research, the VIP model can be improved to accurately predict injuries found experimentally. With this ability, countermeasures can easily be tested in the VIP model to accurately determine whether they can prevent injury. In the end, the VIP model is a tool that has the ability to protect soldiers in the battlefield.

### 6.3 Limitations and Future Work

While the drop tower apparatus was sufficient for use in this thesis, there were some improvements that would likely need to occur if used outside the bounds of this thesis. Most notable was the impact velocity. The average velocity used for compression of the gluteal tissue samples was 3 m/s, although the drop tower was capable of much faster impacts, upwards of 10 m/s. However, even at 3 m/s, significant high-frequency content was transferred to the load cell requiring filtering. While an effective filter was able to clean the signal without significantly changing the key components of the signal, and increase in velocity would only increase this high-frequency ringing seen.

This was due to poor isolation of the load cell on the drop tower. The load cell was connected to the same sheet of thick aluminum that both the arresters for the indenter and the drop weight were connected to. This aluminum sheet was connected to aluminum risers that raise the bed of the drop tower for ease of use. While this was effective for ease of use, it did not absorb vibration well, and the load cell picked up this vibration in the signal. With some forethought, a similar design could be made that isolated the load cell from the aluminum plate in order to avoid vibration from the rig. If that was done, higher rate impacts could be performed without compromising the load cell signal.

In addition, the tissue samples used to create the tissue constitutive model tended to be skewed both in age and sex. The eleven specimens came from eight different male donors with an average age of 69 years old, with the youngest donor being 59 years old. For underbody blast research, the typical target demographic is young adult males, and while all specimens used were male, they were much older. For a more accurate material model, more tissue should be tested including a younger population. Testing should also be performed to see if tissues from different sexes have significantly different material properties.

The average BMI was 29.5 with a good spread of normal BMI and overweight BMI. Because of this, a high deviation of fat and muscle thicknesses were found in the samples used. While samples were attempted to be harvested from the same place on each specimen, there was some variation in the tissue. In the sample set used, no significant correlations between thicknesses of different tissues and other measures such as weight or age were found. In the end, the constitutive model used was calculated as the mean of these specimens. Different regions on the pelvis have different ratios of fat and muscle, and caution should be used when applying this material model to other tissue regions with different thicknesses of fat and muscle. The material model also assumed the tissue to be homogenous, which obviously has error in that assumption. Assuming homogeneity was an easy way to avoid the complicated boundaries between the different layers of the tissue, but if the model is used incorrectly, it could provide inaccurate results. To ultimately make a more powerful material model, additional specimens should be tested to have a larger sample set. With a larger sample size, it may be possible to scale material properties of the model based on ratios of fat and muscle to make the model more specimen specific and anatomically specific. While the current tissue is adequate for the load configuration used in this study, doing this would make a more universal high-rate gluteal tissue material model.

As alluded to, not every aspect of the VIP model is validated and complete. While the model was useful in a sensitivity study on finding which variables affected the force response and load path, some of those variables are not adequate for high impact vertical loading. The bone strain properties and sacroiliac material properties need to be validated and updated so that the model includes realistic rotation about the SI joint without fracturing the sacral ala. Also, since the thickness of the tissue was found to make significant differences in the forces and moment at the lumbar load cell, the tissue needs to either be remeshed or morphed based on each specific specimen. The current tissue is split into an inner portion of tetrahedral elements with an outside layer of hexahedral elements. While the geometry of the pelvic is complicated, an

attempt to mesh the entire tissue layer out of hexahedral elements would lead to a more accurate stiffness of the tissue, especially considering the large amounts of deformation in a high-rate impact. An investigation should also be done to what the effects are of varying pelvic bone geometry. If these differences lead to significant differences in the loading of the pelvis, morphing of the bone to be specimen specific should also be done.

FE models are great tools to measure stresses and strains through an object with complex geometry, something that is difficult from an analytical or experimental approach. But the FE model needs to be validated in order to have confidence in any analysis. Making these changes to the VIP model will help validate the model to the experimental UBB tests performed. However, the input conditions for these tests were purposefully designed to be non-injurious in order to analyze the loads on the pelvis without using censored data. The end goal for this research into UBBs is to understand how the pelvis is injured during these events in order to make effective countermeasures. Additional tests have been performed on component pelvises in similar impact conditions but have been designed to find the limit between injury and non-injury. Once the VIP model has been validated to the previous data set, it can start to be adapted for use in these additional tests to update fracture properties of the bones and other parts of the pelvis to match injuries from those tests. With a fully validated model to both injurious and non-injuries tests, the model can be used as a method to test countermeasures, such as energy absorbing seats and vehicles, to analyze their effectiveness in preventing injury to soldiers in warzones.



## 7 References

- [1] “DCAS - Conflict Casualties” [Online]. Available: <https://www.dmdc.osd.mil/dcas/pages/casualties.xhtml>. [Accessed: 20-Dec-2016].
- [2] Fischer, H., “A Guide to U.S. Military Casualty Statistics: Operation Freedom’s Sentinel, Operation Inherent Resolve, Operation New Dawn, Operation Iraqi Freedom, and Operation Enduring Freedom,” p. 10.
- [3] Ramasamy, A., Masouros, S. D., Newell, N., Hill, A. M., Proud, W. G., Brown, K. A., Bull, A. M. J., and Clasper, J. C., 2011, “In-Vehicle Extremity Injuries from Improvised Explosive Devices: Current and Future Foci,” *Philos. Trans. R. Soc. Lond. B Biol. Sci.*, 366(1562), pp. 160–170.
- [4] Bird, S. M., and Fairweather, C. B., 2007, “Military Fatality Rates (by Cause) in Afghanistan and Iraq: A Measure of Hostilities,” *Int. J. Epidemiol.*, 36(4), pp. 841–846.
- [5] Covey, D. C., 2006, “Combat Orthopaedics: A View from the Trenches,” *J. Am. Acad. Orthop. Surg.*, 14(10), pp. S10–S17.
- [6] Belmont, P. J., Schoenfeld, A. J., and Goodman, G., 2010, “Epidemiology of Combat Wounds in Operation Iraqi Freedom and Operation Enduring Freedom: Orthopaedic Burden of Disease,” *J Surg Orthop Adv*, 19(1), pp. 2–7.
- [7] Vasquez, K., Logsdon, K., Shivers, B., and Chancey, C., 2011, “Medical Injury Data.”
- [8] Salzar, R. S., Genovese, D., Bass, C. R., Bolton, J. R., Guillemot, H., Damon, A. M., and Crandall, J. R., 2009, “Load Path Distribution within the Pelvic Structure under Lateral Loading,” *Int. J. Crashworthiness*, 14(1), pp. 99–110.
- [9] Kulkarni, K. B., Ramalingam, J., and Thyagarajan, R., 2014, “Assessment of the Accuracy of Certain Reduced Order Models Used in the Prediction of Occupant Injury during Under-Body Blast Events,” *SAE Int. J. Transp. Saf.*, 2(2), pp. 307–319.
- [10] NATO, “Test Methodology for Protection of Vehicle Occupants against Anti-Vehicular Landmine Effects.”
- [11] [www.dtsweb.com](http://www.dtsweb.com), DTS - WIAMAN Blast Image w Manikin PR.Jpg.
- [12] Perry, B. J., Gabler, L., Bailey, A., Henderson, K., Brozoski, F., and Salzar, R. S., 2014, “Lower Leg Characterization and Injury Mitigation.”
- [13] Henderson, K., Bailey, A. M., Christopher, J., Brozoski, F., and Salzar, R. S., 2013, “Biomechanical Response of the Lower Leg under High Rate Loading,” *IRCOBI Conference*.
- [14] Bir, Barbir, Dosquet, Wilhelm, Horst, van der, and Wolfe, 2014, “Validation of Lower Limb Surrogates as Injury Assessment Tools in Floor Impacts Due to Anti-Vehicular Land Mines,” *Mil. Med.*

- [15] McKay, B. J., and Bir, C. A., 2009, "Lower Extremity Injury Criteria for Evaluating Military Vehicle Occupant Injury in Underbelly Blast Events," *Stapp Car Crash J.*, 53, pp. 229–49.
- [16] Quenneville, C. E., Fraser, G. S., and Dunning, C. E., 2009, "Development of an Apparatus to Produce Fractures From Short-Duration High-Impulse Loading With an Application in the Lower Leg," *J. Biomech. Eng.*, 132(1), pp. 014502-014502–4.
- [17] Horst, M. J. van der, Simms, C. K., Maasdam, R. van, and Leerdam, P. J. C., 2005, "Occupant Lower Leg Injury Assessment in Landmine Detonations under a Vehicle," *IUTAM Symposium on Impact Biomechanics: From Fundamental Insights to Applications*, Springer, Dordrecht, pp. 41–49.
- [18] Bailey, A. M., Perry, B. J., and Salzar, R. S., 2017, "Response and Injury of the Human Leg for Axial Impact Durations Applicable to Automotive Intrusion and Underbody Blast Environments," *Int. J. Crashworthiness*, 0(0), pp. 1–9.
- [19] Bailey, A., Christopher, J., Henderson, K., Brozoski, F., and Salzar, R. S., 2013, "Comparison of Hybrid-III and PMHS Response to Simulated Underbody Blast Loading Conditions," *Proceedings of IRCOBI Conference*, pp. 158–171.
- [20] Wang, J., Bird, R., Swinton, B., and Krstic, A., 2001, "Protection of Lower Limbs against Floor Impact in Army Vehicles Experiencing Landmine Explosion," *J. Battlef. Technol.*, 4(3).
- [21] Gabler, L. F., Panzer, M. B., and Salzar, R. S., 2014, "High-Rate Mechanical Properties of Human Heel Pad for Simulation of a Blast Loading Condition," *IRC-14-87 IRCOBI Conference 2014*.
- [22] Bailey, A. M., Christopher, J. J., Brozoski, F., and Salzar, R. S., 2014, "Post Mortem Human Surrogate Injury Response of the Pelvis and Lower Extremities to Simulated Underbody Blast," *Ann. Biomed. Eng.*, 43(8), pp. 1907–1917.
- [23] Danelson, K. A., Kemper, A. R., Mason, M. J., Tegtmeier, M., Swiatkowski, S. A., Bolte IV, J. H., and Hardy, W. N., 2015, "Comparison of ATD to PMHS Response in the Under-Body Blast Environment," *Stapp Car Crash J.*, 59, pp. 445–520.
- [24] Yoganandan, N., Moore, J., Arun, M. W. J., and Pintar, F. A., 2014, "Dynamic Responses of Intact Post Mortem Human Surrogates from Inferior-to-Superior Loading at the Pelvis," *Stapp Car Crash J. Ann Arbor*, 58, pp. 123–143.
- [25] Bouquet, R., Ramet, M., Bermond, F., and Cesari, D., 1994, "Thoracic and Pelvis Human Response to Impact," *Proc. 14th ESV*, pp. 100–109.
- [26] Salzar, R. S., Bass, C. R. D., Kent, R., Millington, S., Davis, M., Lucas, S., Rudd, R., Folk, B., Donnellan, L., Murakami, D., and Kobayashi, S., 2006, "Development of Injury Criteria for Pelvic Fracture in Frontal Crashes," *Traffic Inj. Prev.*, 7(3), pp. 299–305.

- [27] Untaroiu, C. D., Shin, J., Yue, N., Kim, Y.-H., Kim, J.-E., and Eberhardt, A. W., 2012, "A Finite Element Model of the Pelvis and Lower Limb for Automotive Impact Applications," *FEA Inf. Eng. J.*
- [28] Bouquet, R., Ramet, M., Bermond, F., Caire, Y., Talantikite, Y., Robin, S., and Voiglio, E., 1998, "Pelvis Human Response to Lateral Impact," *Proceedings of the 16th International Technical Conference on the Enhanced Safety of Vehicles*, Windsor, ON, Canada, pp. 1665–1686.
- [29] Cesari, D., and Ramet, M., 1982, *Pelvic Tolerance and Protection Criteria in Side Impact*, SAE Technical Paper.
- [30] Cesari, D., Ramet, M., and Clair, P.-Y., 1980, *Evaluation of Pelvic Fracture Tolerance in Side Impact*, SAE Technical Paper.
- [31] Matsui, Y., Kajzer, J., Wittek, A., Ishikawa, H., Schroeder, G., and Bosch, U., 2003, "Injury Pattern and Tolerance of Human Pelvis Under Lateral Loading Simulating Car-Pedestrian Impact."
- [32] Ramet, M., and Cesari, D., 1979, *Experimental Study of Pelvis Tolerance in Lateral Impact*, International Research Council on Biokinetics of Impacts.
- [33] Plummer, J. W., Bidez, M. W., and Alonso, J., 1996, "Parametric Finite Element Studies of the Human Pelvis: The Influence of Load Magnitude and Duration on Pelvic Tolerance During Side Impact."
- [34] Song, E., Trosseille, X., and Guillemot, H., 2006, "Side Impact: Influence of Impact Conditions and Bone Mechanical Properties on Pelvic Response Using a Fracturable Pelvis Model," *Stapp Car Crash J. Ann Arbor*, 50, pp. 75–95.
- [35] Salzar, R. S., Bolton, J. R., Crandall, J. R., Paskoff, G. R., and Shender, B. S., 2009, "Ejection Injury to the Spine in Small Aviators: Sled Tests of Manikins vs. Post Mortem Specimens," *Aviat. Space Environ. Med.*, 80(7), pp. 621–628.
- [36] Encyclopaedia Britannica, Inc., "Pelvic Girdle," *Encycl. Br.* [Online]. Available: <https://www.britannica.com/science/pelvic-girdle/media/449463/197299>. [Accessed: 18-Feb-2019].
- [37] O'Hara, B., "Pelvis," *Wikipedia* [Online]. Available: <https://en.wikipedia.org/wiki/Pelvis>. [Accessed: 18-Feb-2019].
- [38] Blemker, S. S., and Delp, S. L., 2005, "Three-Dimensional Representation of Complex Muscle Architectures and Geometries," *Ann. Biomed. Eng.*, 33(5), pp. 661–673.
- [39] Donald Neuman, "The Osteokinematics of the Right Hip Joint.," *Clin. Gate* [Online]. Available: <https://clinicalgate.com/hip-5/>. [Accessed: 18-Feb-2019].

- [40] Drummond, D. S., Narechania, R. G., Rosenthal, A. N., Breed, A. L., Lange, T. A., and Drummond, D. K., 1982, "A Study of Pressure Distributions Measured during Balanced and Unbalanced Sitting," *J Bone Jt. Surg Am*, 64(7), pp. 1034–1039.
- [41] Chow, W. W., and Odell, E. I., 1978, "Deformations and Stresses in Soft Body Tissues of a Sitting Person," *J. Biomech. Eng.*, 100(2), pp. 79–87.
- [42] Wagnac, É. L., Aubin, C. É., and Dansereau, J., 2008, "A New Method to Generate a Patient-Specific Finite Element Model of the Human Buttocks," *IEEE Trans. Biomed. Eng.*, 55(2), pp. 774–783.
- [43] Linder-Ganz, E., Shabshin, N., Itzhak, Y., and Gefen, A., 2007, "Assessment of Mechanical Conditions in Sub-Dermal Tissues during Sitting: A Combined Experimental-MRI and Finite Element Approach," *J. Biomech.*, 40(7), pp. 1443–1454.
- [44] Gefen, A., Gefen, N., Linder-Ganz, E., and Margulies, S. S., 2005, "In Vivo Muscle Stiffening Under Bone Compression Promotes Deep Pressure Sores," *J. Biomech. Eng.*, 127(3), p. 512.
- [45] Makhssous, M., Lin, F., Cichowski, A., Cheng, I., Fasanati, C., Grant, T., and Hendrix, R. W., 2011, "Use of MRI Images to Measure Tissue Thickness over the Ischial Tuberosity at Different Hip Flexion," *Clin. Anat.*, 24(5), pp. 638–645.
- [46] Sonenblum, S. E., Sprigle, S. H., Cathcart, J. M., and Winder, R. J., 2013, "3-Dimensional Buttocks Response to Sitting: A Case Report," *J. Tissue Viability*, 22(1), pp. 12–18.
- [47] Sonenblum, S. E., Sprigle, S. H., Cathcart, J. M., and Winder, R. J., 2015, "3D Anatomy and Deformation of the Seated Buttocks," *J. Tissue Viability*, 24(2), pp. 51–61.
- [48] Shabshin, N., Ougortsin, V., Zoizner, G., and Gefen, A., 2010, "Evaluation of the Effect of Trunk Tilt on Compressive Soft Tissue Deformations under the Ischial Tuberosities Using Weight-Bearing MRI," *Clin. Biomech.*, 25(5), pp. 402–408.
- [49] Al-Dirini, R. M. A., Reed, M. P., and Thewlis, D., 2015, "Deformation of the Gluteal Soft Tissues during Sitting," *Clin. Biomech.*, 30(7), pp. 662–668.
- [50] Sopher, R., Nixon, J., Gorecki, C., and Gefen, A., 2010, "Exposure to Internal Muscle Tissue Loads under the Ischial Tuberosities during Sitting Is Elevated at Abnormally High or Low Body Mass Indices," *J. Biomech.*, 43(2), pp. 280–286.
- [51] Luboz, V., Petrizelli, M., Bucki, M., Diot, B., Vuillerme, N., and Payan, Y., 2014, "Biomechanical Modeling to Prevent Ischial Pressure Ulcers," *J. Biomech.*, 47(10), pp. 2231–2236.
- [52] Linder-Ganz, E., Shabshin, N., Itzhak, Y., Yizhar, Z., Siev-Ner, I., and Gefen, A., 2008, "Strains and Stresses in Sub-Dermal Tissues of the Buttocks Are Greater in Paraplegics than in Healthy during Sitting," *J. Biomech.*, 41(3), pp. 567–580.

- [53] Dunk, N. M., and Callaghan, J. P., 2005, "Gender-Based Differences in Postural Responses to Seated Exposures," *Clin. Biomech.*, 20(10), pp. 1101–1110.
- [54] Olesen, C. G., Zee, M. de, and Rasmussen, J., 2010, "Missing Links in Pressure Ulcer Research—An Interdisciplinary Overview," *J. Appl. Physiol.*, 108(6), pp. 1458–1464.
- [55] Ramasamy, A., Evans, S., Kendrew, J. M., and Cooper, J., 2012, "The Open Blast Pelvis," *J Bone Jt. Surg Br*, 94-B(6), pp. 829–835.
- [56] Bailey, J. R., Stinner, D. J., Blackbourne, L. H., Hsu, J. R., and Mazurek, M. T., 2011, "Combat-Related Pelvis Fractures in Nonsurvivors:," *J. Trauma Inj. Infect. Crit. Care*, 71(supplement), pp. S58–S61.
- [57] Tile, M., 1996, "Acute Pelvic Fractures: I. Causation and Classification," *JAAOS - J. Am. Acad. Orthop. Surg.*, 4(3), p. 143.
- [58] Alton, T. B., and Gee, A. O., 2014, "Classifications in Brief: Young and Burgess Classification of Pelvic Ring Injuries," *Clin Orthop Relat Res*, 472(8), pp. 2338–2342.
- [59] Calder, P. C., Harvey, D. J., Pond, C. M., and Newsholme, E. A., 1992, "Site-Specific Differences in the Fatty Acid Composition of Human Adipose Tissue," *Lipids*, 27(9), pp. 716–720.
- [60] Malcom, G. T., Bhattacharyya, A. K., Velez-Duran, M., Guzman, M. A., Oalman, M. C., and Strong, J. P., 1989, "Fatty Acid Composition of Adipose Tissue in Humans: Differences between Subcutaneous Sites," *Am. J. Clin. Nutr.*, 50(2), pp. 288–291.
- [61] Mamalakis, G., Kafatos, A., Manios, Y., Kalogeropoulos, N., and Andrikopoulos, N., 2002, "Abdominal vs Buttock Adipose Fat: Relationships with Children's Serum Lipid Levels," *Eur. J. Clin. Nutr.*, 56(11), pp. 1081–1086.
- [62] Hayes, W. C., and Mockros, L. F., 1971, "Viscoelastic Properties of Human Articular Cartilage.," *J. Appl. Physiol.*, 31(4), pp. 562–568.
- [63] Fung, Y., 1993, *Biomechanics: Mechanical Properties of Living Tissues*, Springer Science & Business Media.
- [64] Gefen, A., and Haberman, E., 2007, "Viscoelastic Properties of Ovine Adipose Tissue Covering the Gluteus Muscles," *J. Biomech. Eng.*, 129(6), pp. 924–930.
- [65] Palevski, A., Gleich, I., Portnoy, S., Linder-Ganz, E., and Gefen, A., 2006, "Stress Relaxation of Porcine Gluteus Muscle Subjected to Sudden Transverse Deformation as Related to Pressure Sore Modeling," *J. Biomech. Eng.*, 128(5), pp. 782–787.
- [66] Then, C., Menger, J., Benderoth, G., Alizadeh, M., Vogl, T. J., Hübner, F., and Silber, G., 2007, "A Method for a Mechanical Characterisation of Human Gluteal Tissue," *Technol. Health Care*, 15(6), pp. 385–398.

- [67] Todd, B. A., and Thacker, J. G., 1994, "Three-Dimensional Computer Model of the Human Buttocks, in Vivo.," *J. Rehabil. Res. Dev.*, 31(2), p. 111.
- [68] Wang, J., Brienza, D. M., Ying-wei, Y., Karg, P., and Xue, Q., 2000, "A Compound Sensor for Biomechanical Analyses of Buttock Soft Tissue in Vivo," *J. Rehabil. Res. Dev.*, 37(4), p. 433.
- [69] Houten, E. E. W. V., Doyley, M. M., Kennedy, F. E., Weaver, J. B., and Paulsen, K. D., 2003, "Initial in Vivo Experience with Steady-State Subzone-Based MR Elastography of the Human Breast," *J. Magn. Reson. Imaging*, 17(1), pp. 72–85.
- [70] Samani, A., and Plewes, D., 2004, "A Method to Measure the Hyperelastic Parameters of Ex Vivo Breast Tissue Samples," *Phys. Med. Biol.*, 49(18), p. 4395.
- [71] Erdemir, A., Viveiros, M. L., Ulbrecht, J. S., and Cavanagh, P. R., 2006, "An Inverse Finite-Element Model of Heel-Pad Indentation," *J. Biomech.*, 39(7), pp. 1279–1286.
- [72] Dabnichki, P. A., Crocombe, A. D., and Hughes, S. C., 1994, "Deformation and Stress Analysis of Supported Buttock Contact," *Proc. Inst. Mech. Eng. [H]*, 208(1), pp. 9–17.
- [73] Brosh, T., and Arcan, M., 2000, "Modeling the Body/Chair Interaction – an Integrative Experimental–Numerical Approach," *Clin. Biomech.*, 15(3), pp. 217–219.
- [74] Oomens, C. W. J., Bressers, O. F. J. T., Bosboom, E. M. H., Bouten, C. V. C., and Bader, D. L., 2003, "Can Loaded Interface Characteristics Influence Strain Distributions in Muscle Adjacent to Bony Prominences?," *Comput. Methods Biomech. Biomed. Engin.*, 6(3), pp. 171–180.
- [75] Linder-Ganz, E., Yarnitzky, G., Yizhar, Z., Siev-Ner, I., and Gefen, A., 2009, "Real-Time Finite Element Monitoring of Sub-Dermal Tissue Stresses in Individuals with Spinal Cord Injury: Toward Prevention of Pressure Ulcers," *Ann. Biomed. Eng.*, 37(2), p. 387.
- [76] Anderson, A. E., Peters, C. L., Tuttle, B. D., and Weiss, J. A., 2005, "Subject-Specific Finite Element Model of the Pelvis: Development, Validation and Sensitivity Studies," *J. Biomech. Eng.*, 127(3), pp. 364–373.
- [77] Grujicic, M., Pandurangan, B., Arakere, G., Bell, W. C., He, T., and Xie, X., 2009, "Seat-Cushion and Soft-Tissue Material Modeling and a Finite Element Investigation of the Seating Comfort for Passenger-Vehicle Occupants," *Mater. Des.*, 30(10), pp. 4273–4285.
- [78] Besnault, B., Lavaste, F., Guillemot, H., Robin, S., and Le Coz, J.-Y., 1998, "A Parametric Finite Element Model of the Human Pelvis."
- [79] Dawson, J. M., Khmelniker, B. V., and McAndrew, M. P., 1999, "Analysis of the Structural Behavior of the Pelvis during Lateral Impact Using the Finite Element Method," *Accid. Anal. Prev.*, 31(1–2), pp. 109–119.



- [80] Ko, C., Konosu, A., Sakamoto, J., and Yukita, Y., 2006, A Study on Development of a Human Pelvis FE Model by Applying In-Vivo CT Information of the Human Coxal Bone, SAE Technical Paper.
- [81] Huang, Y., King, A. I., and Cavanaugh, J. M., 1994, "Finite Element Modeling of Gross Motion of Human Cadavers in Side Impact," SAE Trans., 103, pp. 1604–1622.
- [82] Lizee, E., Robin, S., Song, E., Bertholon, N., Le Coz, J.-Y., Besnault, B., and Lavaste, F., 1998, Development of a 3D Finite Element Model of the Human Body, SAE Technical Paper.
- [83] Ruan, J. S., El-Jawahri, R., Barbat, S., and Prasad, P., 2005, "Biomechanical Analysis of Human Abdominal Impact Responses and Injuries through Finite Element Simulations of a Full Human Body Model," Stapp Car Crash J., 49, pp. 343–366.
- [84] Spitzer, V., Ackerman, M. J., Scherzinger, A. L., and Whitlock, D., 1996, "The Visible Human Male: A Technical Report," J. Am. Med. Inform. Assoc. JAMIA, 3(2), pp. 118–130.
- [85] "ESI Group" [Online]. Available: <https://www.esi-group.com/jp>. [Accessed: 12-Oct-2018].
- [86] Konosu, A., 2003, "Development of a Biofidelic Human Pelvic FE-Model with Several Modifications onto a Commercial Use Model for Lateral Loading Conditions."
- [87] "GHBMC" [Online]. Available: <http://www.ghbmc.com/>. [Accessed: 12-Oct-2018].
- [88] "PIPER" [Online]. Available: <http://piper-project.org/>. [Accessed: 12-Oct-2018].
- [89] Robin, S., 2001, "Humos: Human Model for Safety - a Joint Effort towards the Development of Refined Human-like Car Occupant Models," Proc. Int. Tech. Conf. Enhanc. Saf. Veh., 2001, pp. 9 p.-9 p.
- [90] Vezin, P., and Verriest, J., 2005, "Development of a Set of Numerical Human Models for Safety," Int. Tech. Conf. Enhanc. Saf. Veh., 2005.
- [91] "THUMS" [Online]. Available: <https://www.tytlabs.co.jp/>. [Accessed: 12-Oct-2018].
- [92] "Automotive Safety - Wayne State University" [Online]. Available: <https://automotivesafety.wayne.edu/models>. [Accessed: 12-Oct-2018].
- [93] Dakin, G. J., Arbelaez, R. A., Molz, I., Fred J., Alonso, J. E., Mann, K. A., and Eberhardt, A. W., 2000, "Elastic and Viscoelastic Properties of the Human Pubic Symphysis Joint: Effects of Lateral Impact Loading," J. Biomech. Eng., 123(3), pp. 218–226.
- [94] Beason, D. P., Dakin, G. J., Lopez, R. R., Alonso, J. E., Bandak, F. A., and Eberhardt, A. W., 2003, "Bone Mineral Density Correlates with Fracture Load in Experimental Side Impacts of the Pelvis," J. Biomech., 36(2), pp. 219–227.
- [95] Perry, B. J., Henderson, K. K., Spratley, E. M., Zhang, J., Merkle, A. C., and Salzar, R. S., 2016, "Effects of Seated Soldier Posture on Pelvic Force Transmissibility," Washington, D.C.

- [96] Roache, P. J., 1994, "Perspective: A Method for Uniform Reporting of Grid Refinement Studies," *J. Fluids Eng.*, 116(3), pp. 405–413.
- [97] Richardson, L. F., 1911, "IX. The Approximate Arithmetical Solution by Finite Differences of Physical Problems Involving Differential Equations, with an Application to the Stresses in a Masonry Dam," *Phil Trans R Soc Lond A*, 210(459–470), pp. 307–357.
- [98] Schwer, L. E., 2008, "Is Your Mesh Refined Enough? Estimating Discretization Error Using GCI," 7th -DYNA Anwenderforum, 1(1), p. 50.
- [99] Ogden, R. W., 1972, "Large Deformation Isotropic Elasticity – on the Correlation of Theory and Experiment for Incompressible Rubberlike Solids," *Proc R Soc Lond A*, 326(1567), pp. 565–584.
- [100]Gehre, C., Gades, H., and Wernicke, P., 2009, "Objective Rating of Signals Using Test and Simulation Responses."
- [101]Society of Automotive Engineers, Inc., SIGN CONVENTION FOR VEHICLE CRASH TESTING, J1733.



## 8 Permissions

Figure 6: Reprinted from *J. Biomech.*, 40(7), pp. 1443–1454, Linder-Ganz, E., Shabshin, N., Itzhak, Y., and Gefen, A., “Assessment of Mechanical Conditions in Sub-Dermal Tissues during Sitting: A Combined Experimental-MRI and Finite Element Approach,” 2007, with permission from Elsevier.

Figure 7a: Reprinted from *JAAOS - J. Am. Acad. Orthop. Surg.*, 4(3), p. 143, Tile, M., “Acute Pelvic Fractures: I. Causation and Classification,” 1996, with permission from Wolters Kluwer Health, Inc.

Figure 7b: Reprinted from *Clin. Orthop. Relat. Res.*, 472(8), pp. 2338–2342, Alton, T. B., and Gee, A. O., “Classifications in Brief: Young and Burgess Classification of Pelvic Ring Injuries,” 2014, with permission from Wolters Kluwer Health, Inc.

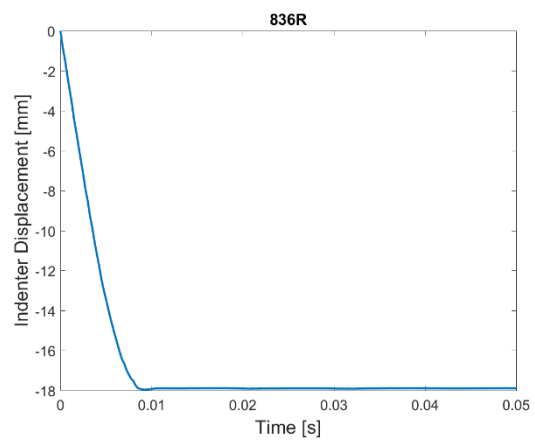
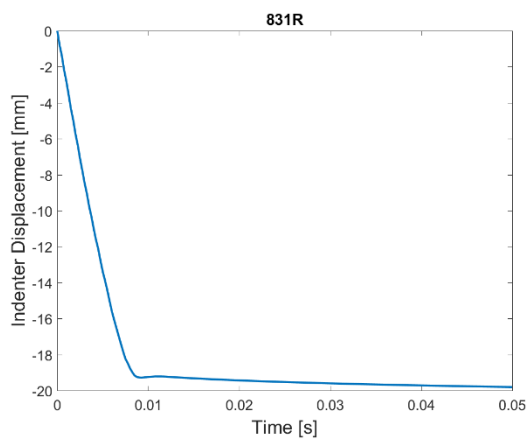
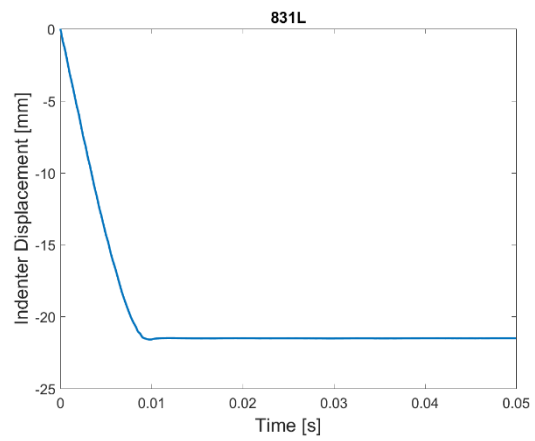
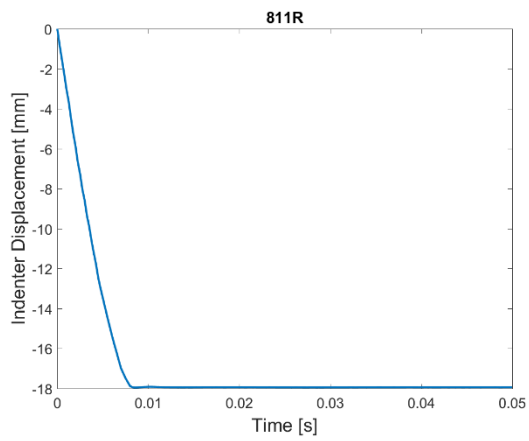
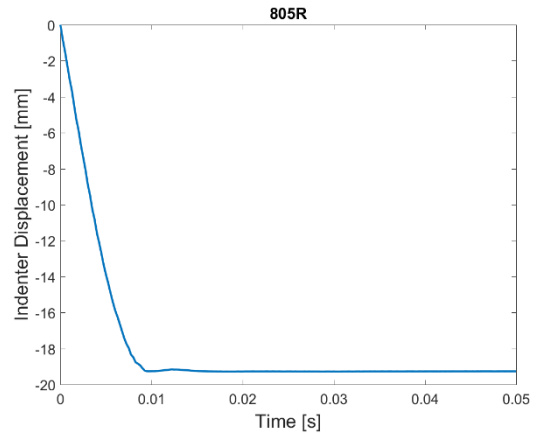
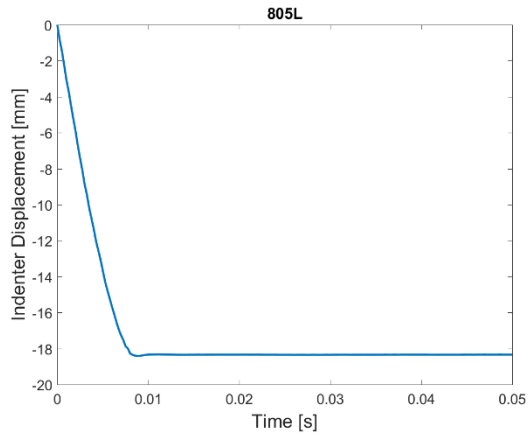
Figure 8: Reprinted from *Technol. Health Care*, 15(6), pp. 385–398, Then, C., Menger, J., Benderoth, G., Alizadeh, M., Vogl, T. J., Hübner, F., and Silber, G., “A Method for a Mechanical Characterisation of Human Gluteal Tissue,” 2007, with permission from IOS Press. The publication is available at IOS Press through <https://content.iospress.com/articles/technology-and-health-care/thc00473>.

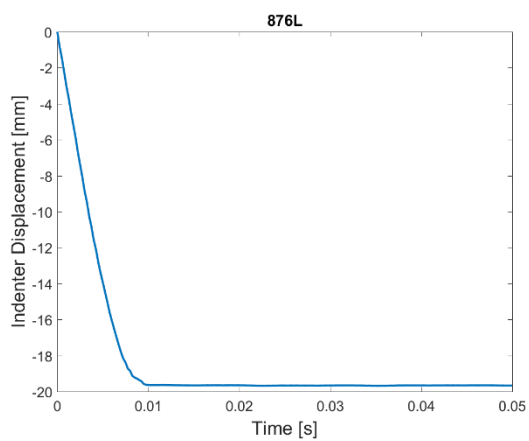
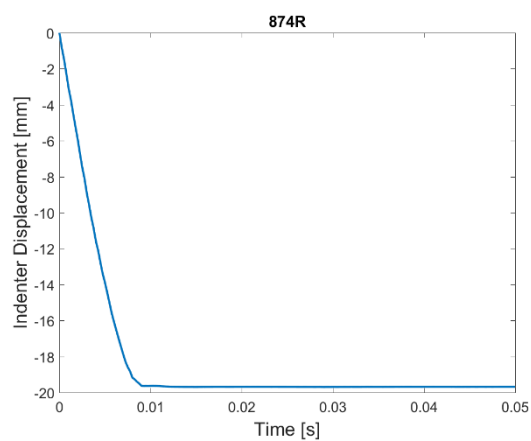
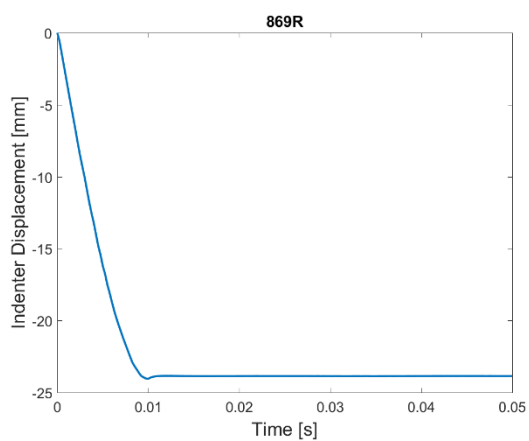
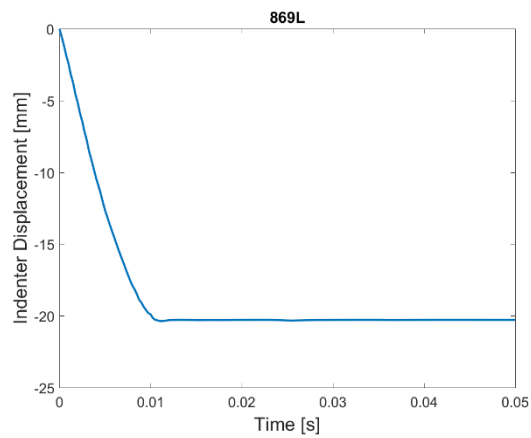
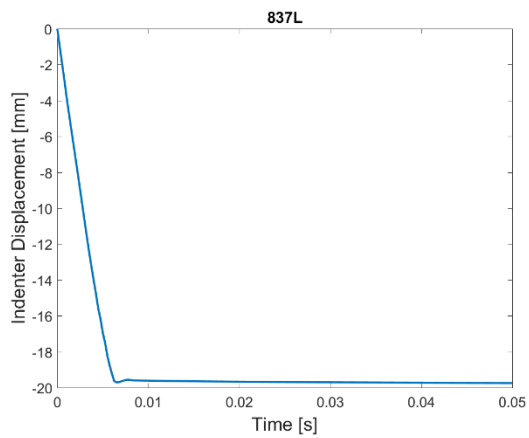
Figure 9: Reprinted from *Mater. Des.*, 30(10), pp. 4273–4285, Grujicic, M., Pandurangan, B., Arakere, G., Bell, W. C., He, T., and Xie, X., “Seat-Cushion and Soft-Tissue Material Modeling and a Finite Element Investigation of the Seating Comfort for Passenger-Vehicle Occupants,” 2009, with permission from Elsevier.

Figure 1: Reprinted from *Int. J. Crashworthiness*, 14(1), pp. 99–110, Salzar, R. S., Genovese, D., Bass, C. R., Bolton, J. R., Guillemot, H., Damon, A. M., and Crandall, J. R., “Load Path Distribution within the Pelvic Structure under Lateral Loading,” 2009, with permission from Taylor & Francis.

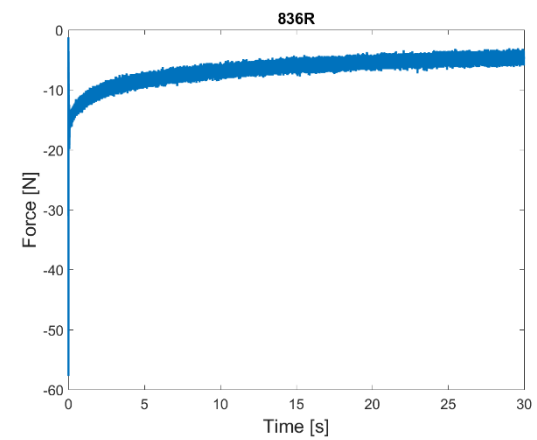
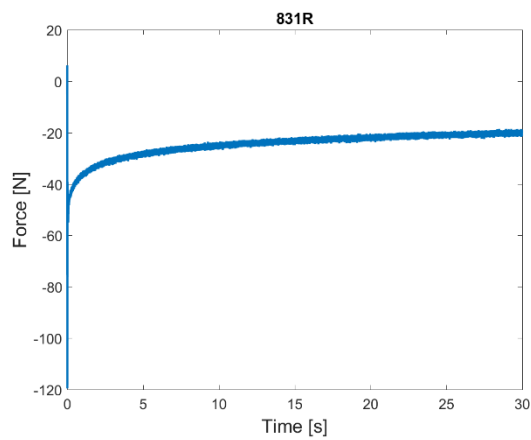
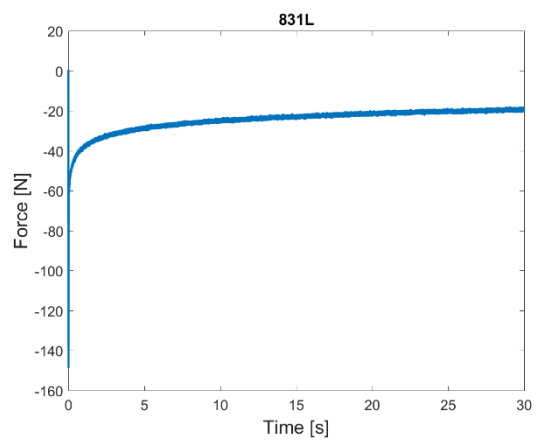
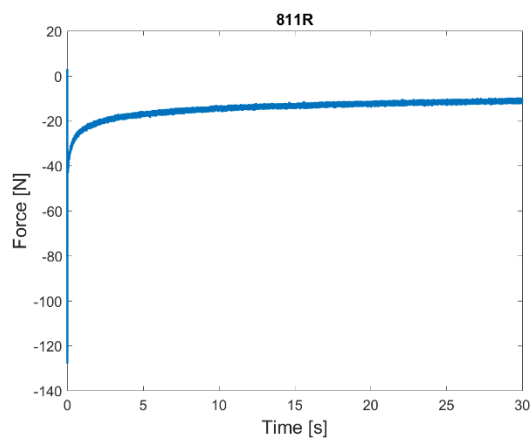
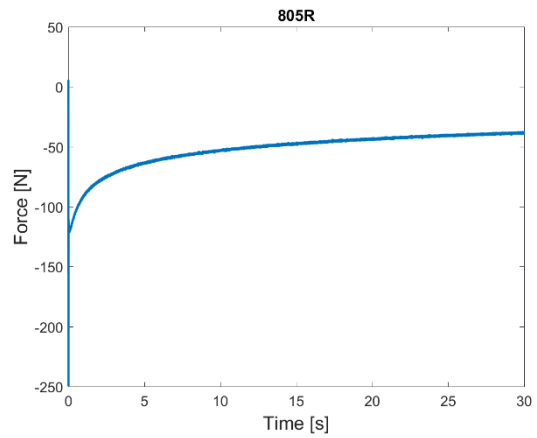
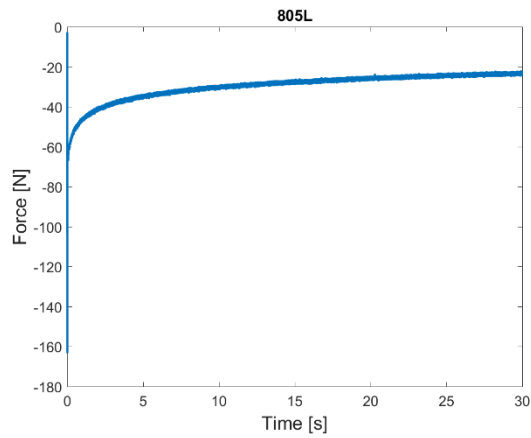
## 9 Appendix

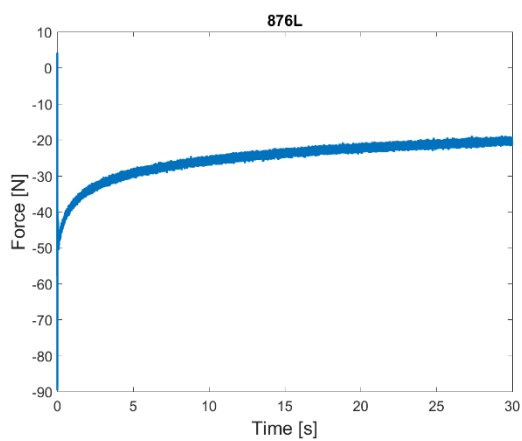
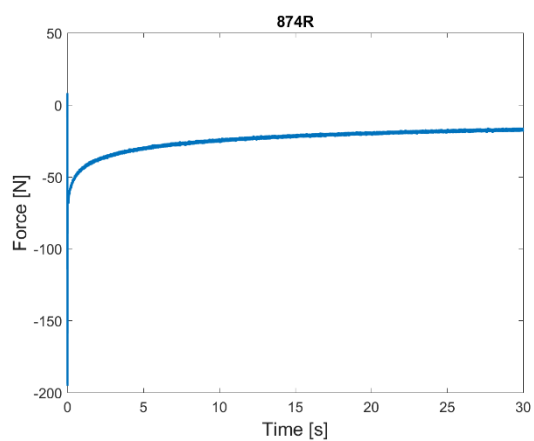
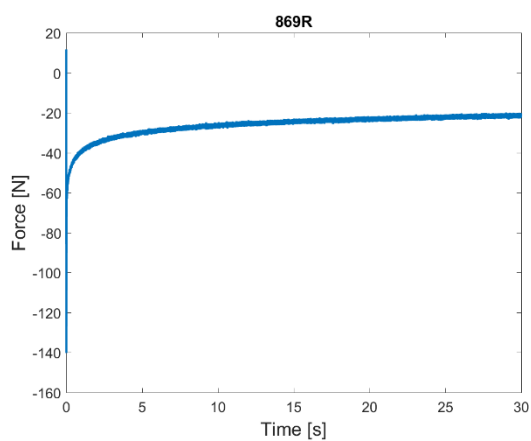
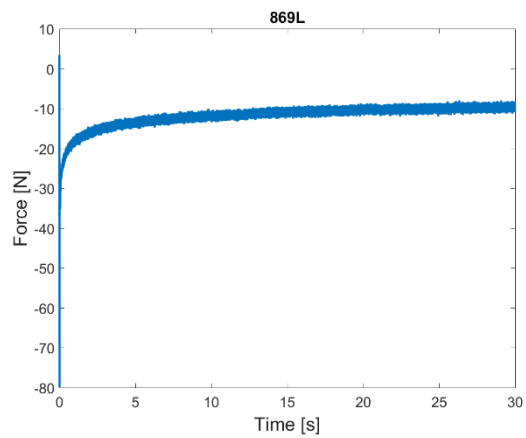
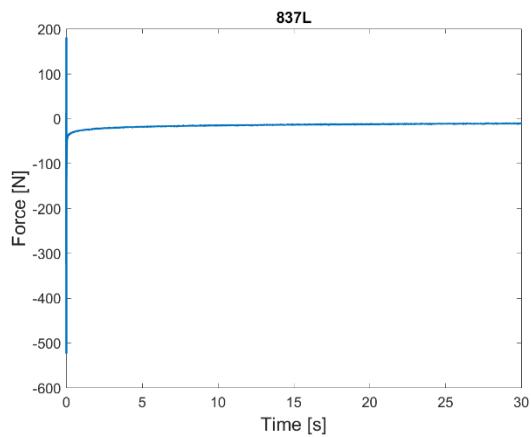
### 9.1 Experimental Input Displacement



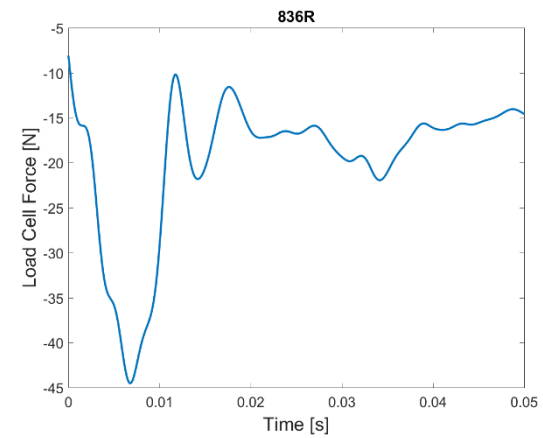
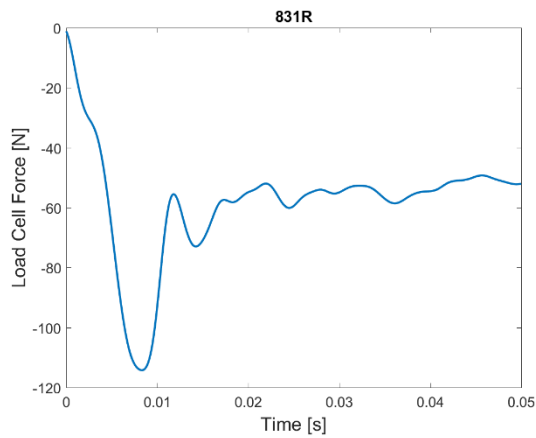
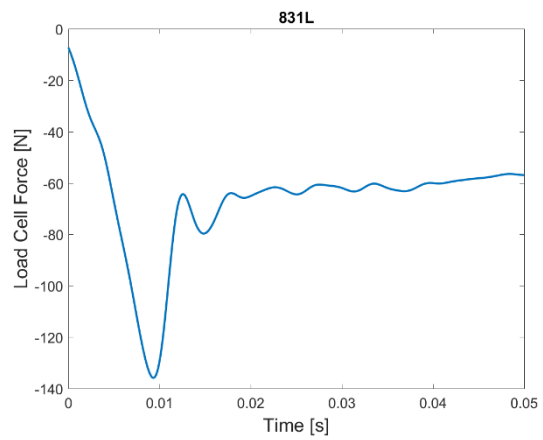
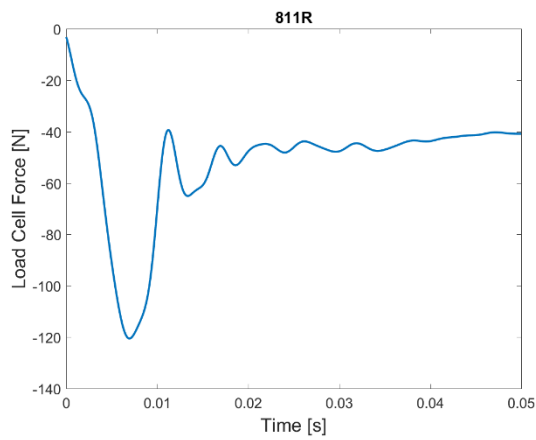
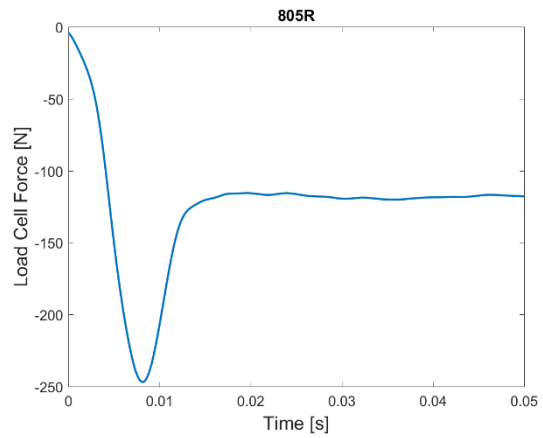
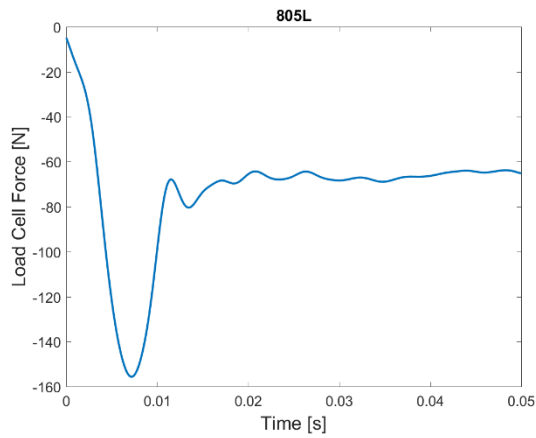


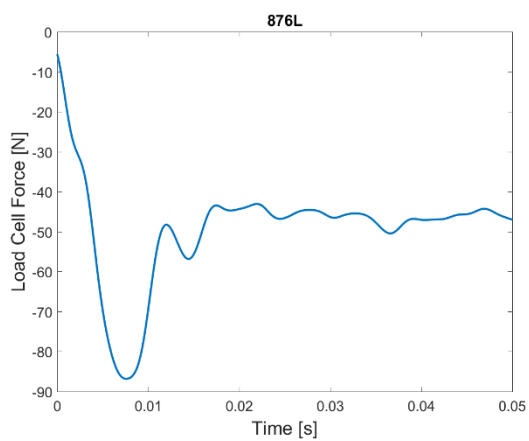
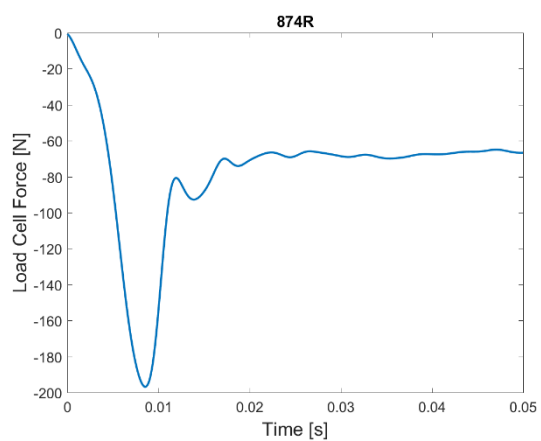
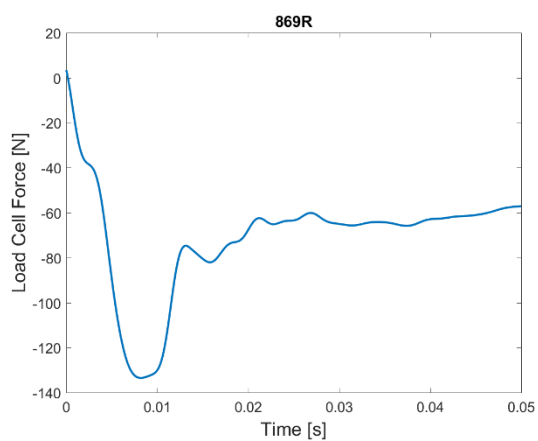
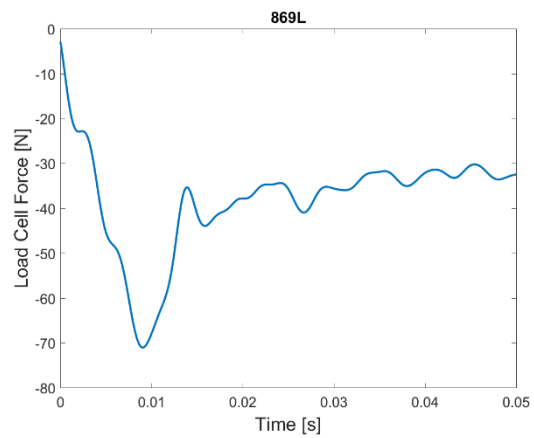
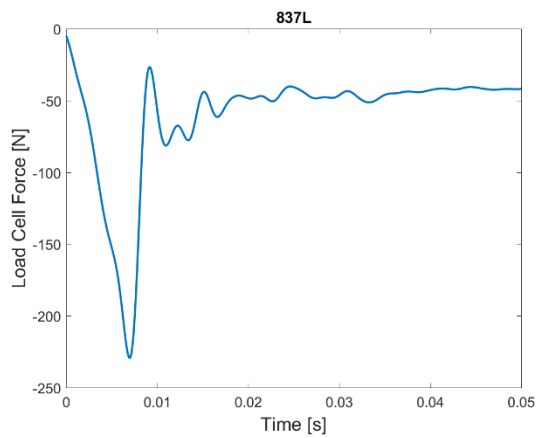
## 9.2 Experimental Load Cell Data (30 s, raw)



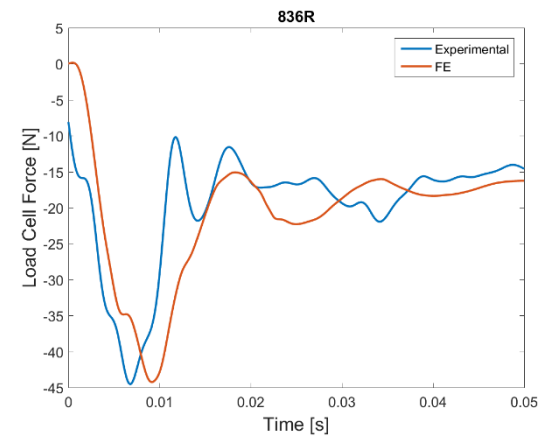
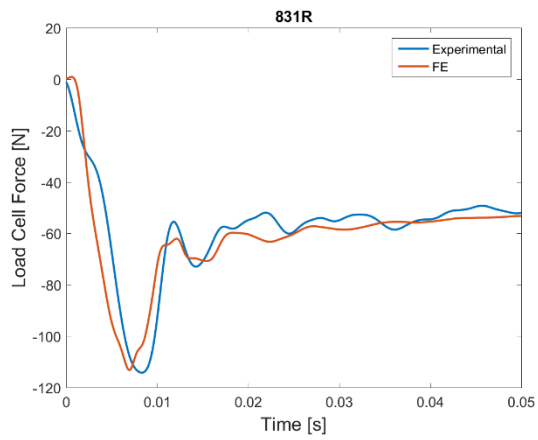
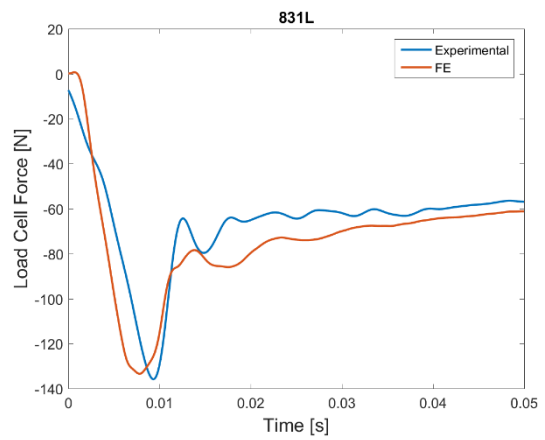
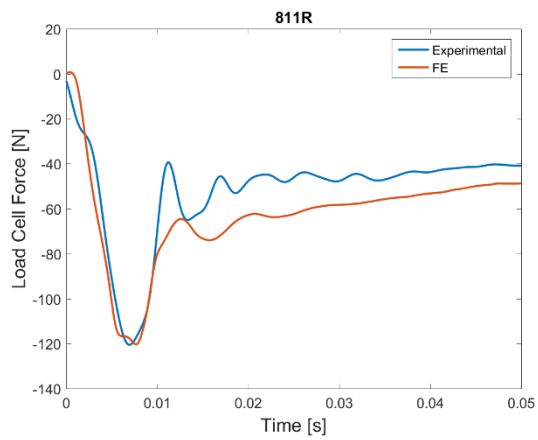
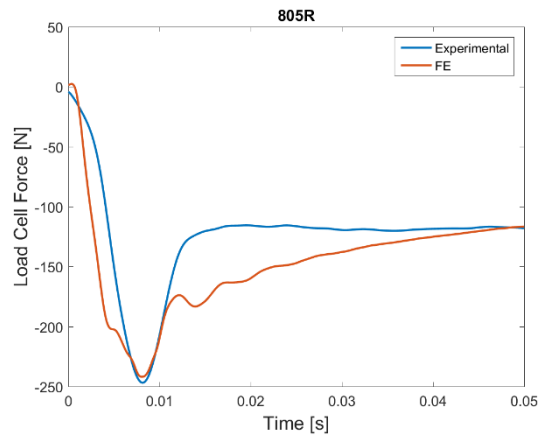
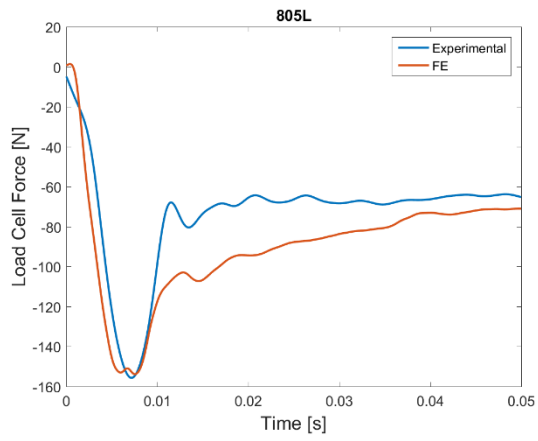


### 9.3 Experimental Load Cell Data (50 ms, filtered)

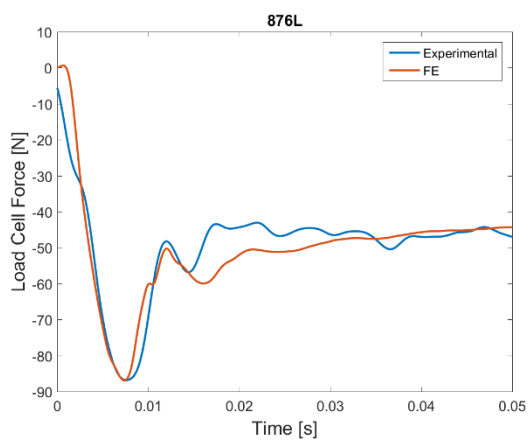
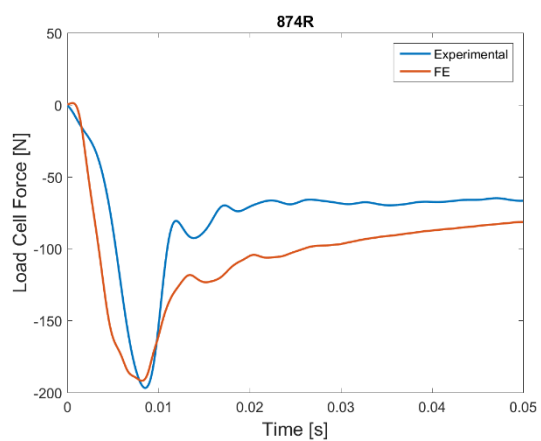
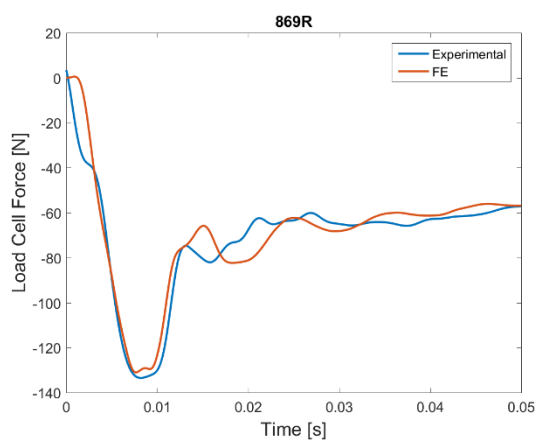
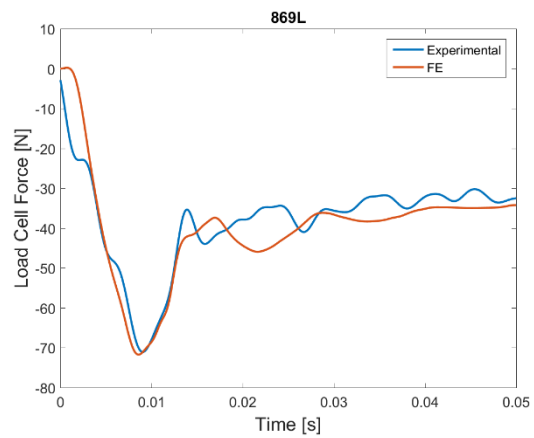
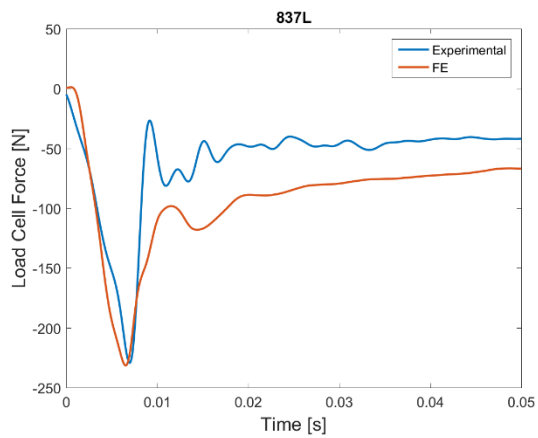




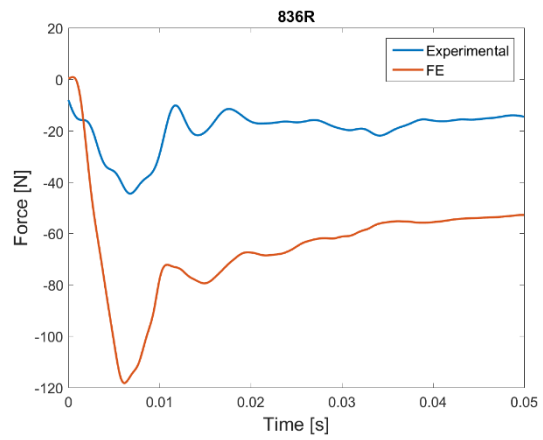
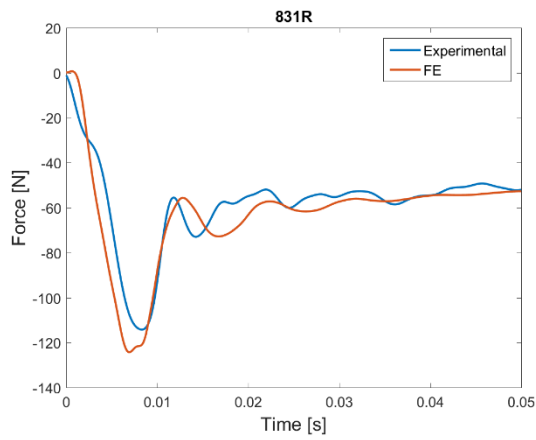
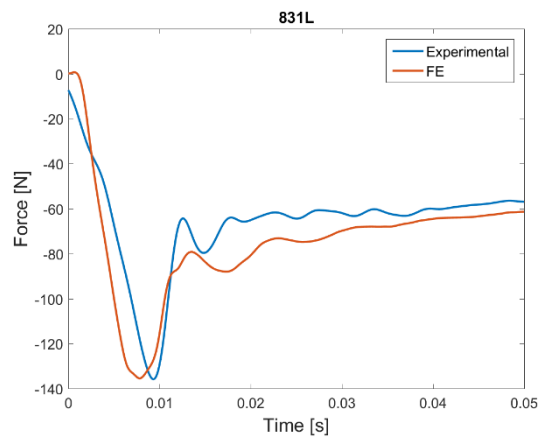
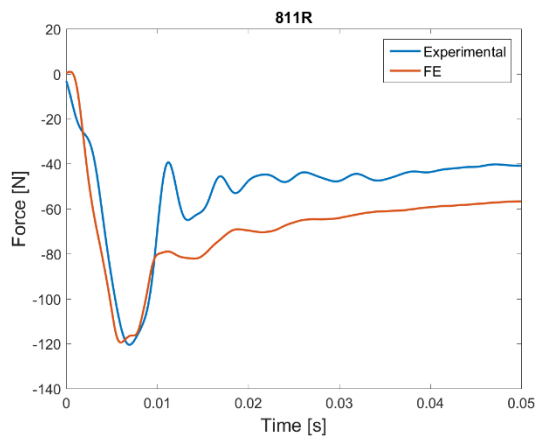
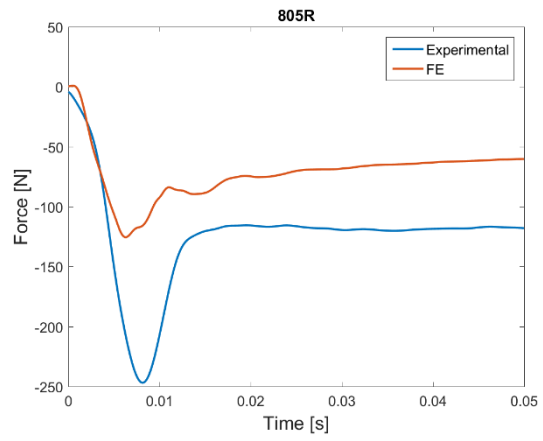
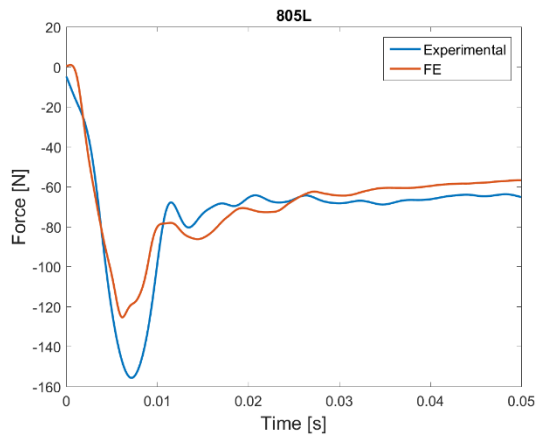
## 9.4 iFE Results

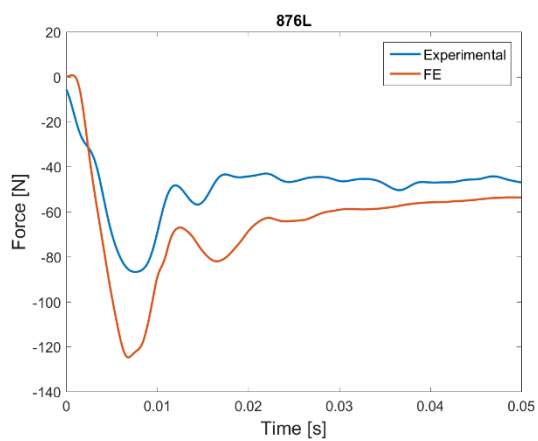
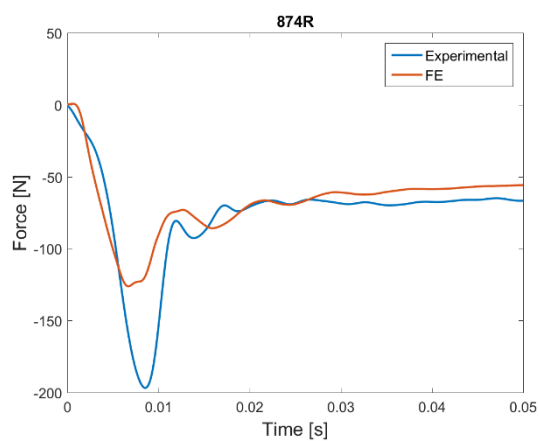
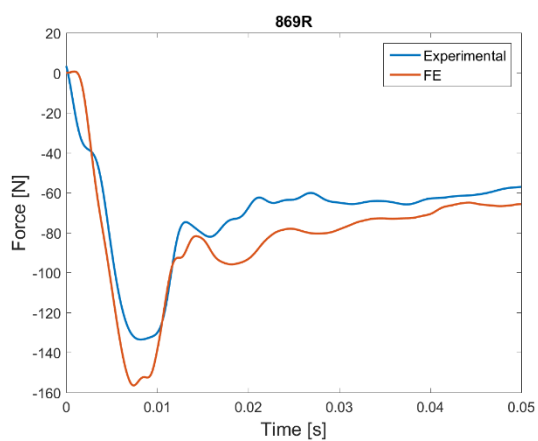
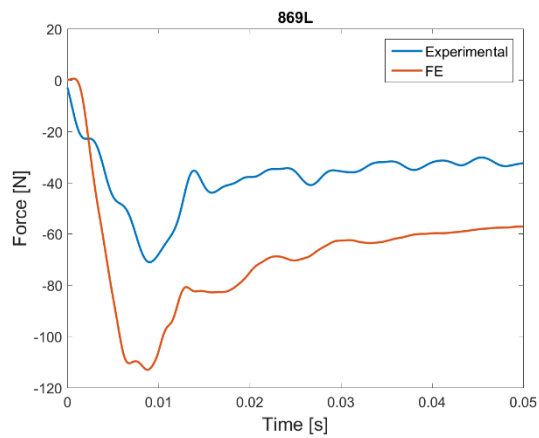
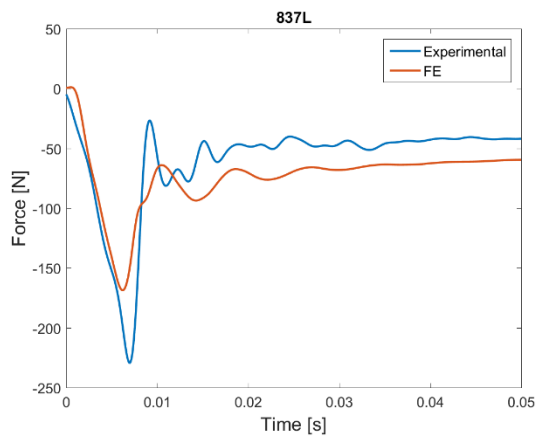






## 9.5 Average iFE Model Comparison





## 9.6 VIP Model Force and Moment Corridor and CORA Ratings

Model Name	% in		$F_x$					Total
	Corridor	Corridor	Phase	Size	Slope	Correlation		
Pmin_Lmin	47.5	0.587	0.937	0.857	0.912	0.902	0.744	
Pmin_Lmean	45.3	0.554	0.916	0.778	0.919	0.871	0.712	
Pmin_Lmax	25.3	0.389	0.916	0.436	0.931	0.761	0.575	
Pmean_Lmin	31.7	0.562	0.863	0.287	0.894	0.681	0.622	
Pmean_Lmean	33.7	0.583	0.905	0.423	0.923	0.750	0.667	
Pmean_Lmax	40.3	0.477	0.989	0.960	0.920	0.956	0.717	
Pmax_Lmin	28.7	0.490	0.789	0.180	0.867	0.612	0.551	
Pmax_Lmean	25.9	0.519	0.863	0.337	0.890	0.697	0.608	
Pmax_Lmax	42.7	0.481	0.968	0.951	0.907	0.942	0.712	
Pmean_Lmean_Thin	38.1	0.554	0.821	0.970	0.933	0.908	0.731	
Pmean_Lmean_Thin_SI	35.7	0.582	0.736	0.843	0.963	0.848	0.715	
Pmean_Lmean_Heavy	32.3	0.571	0.863	0.459	0.923	0.748	0.659	
Pmean_Lmean_SIS stiff	40.5	0.569	0.947	0.376	0.910	0.744	0.656	
Pmean_Lmean_SILoose	33.5	0.574	0.842	0.467	0.935	0.748	0.661	
GHBMC	62.7	0.714	0.998	0.350	0.936	0.762	0.738	

Model Name	% in		$F_z$					Total
	Corridor	Corridor	Phase	Size	Slope	Correlation		
Pmin_Lmin	46.7	0.553	1.000	0.798	0.997	0.932	0.742	
Pmin_Lmean	27.1	0.441	1.000	0.743	0.995	0.913	0.677	
Pmin_Lmax	13.6	0.250	0.947	0.614	0.987	0.849	0.549	
Pmean_Lmin	26.3	0.336	0.641	0.706	0.984	0.777	0.556	
Pmean_Lmean	19.8	0.361	0.726	0.759	0.987	0.824	0.592	
Pmean_Lmax	33.7	0.452	0.894	0.920	0.994	0.936	0.694	
Pmax_Lmin	30.9	0.415	0.494	0.526	0.963	0.661	0.538	
Pmax_Lmean	32.3	0.419	0.620	0.612	0.971	0.734	0.577	
Pmax_Lmax	28.9	0.436	0.852	0.839	0.989	0.893	0.665	

Pmean_Lmean_Thin	18.0	0.281	0.778	0.868	0.998	0.881	0.581
Pmean_Lmean_Thin_SI	31.9	0.440	0.683	0.787	0.994	0.822	0.631
Pmean_Lmean_Heavy	27.5	0.366	0.694	0.912	0.985	0.864	0.615
Pmean_Lmean_SIS stiff	17.2	0.298	0.757	0.826	0.991	0.858	0.578
Pmean_Lmean_SILoose	29.7	0.410	0.694	0.673	0.982	0.783	0.597
GHBMC	20.4	0.274	0.810	0.858	0.990	0.886	0.580

	Model Name	% in		$M_y$				Total
		Corridor	Corridor	Phase	Size	Slope	Correlation	
	Pmin_Lmin	22.0	0.320	0.156	0.329	0.857	0.447	0.384
	Pmin_Lmean	27.3	0.379	0.156	0.391	0.870	0.472	0.426
	Pmin_Lmax	35.1	0.481	0.188	0.563	0.840	0.530	0.506
	Pmean_Lmin	30.3	0.523	0.589	0.448	0.890	0.642	0.582
	Pmean_Lmean	25.3	0.431	0.652	0.478	0.873	0.667	0.549
	Pmean_Lmax	31.5	0.373	0.000	0.389	0.926	0.438	0.406
	Pmax_Lmin	37.3	0.556	0.673	0.609	0.905	0.729	0.642
	Pmax_Lmean	35.5	0.434	0.736	0.545	0.870	0.717	0.576
	Pmax_Lmax	37.3	0.436	0.000	0.339	0.928	0.423	0.429
	Pmean_Lmean_Thin	31.9	0.454	0.000	0.518	0.867	0.462	0.458
	Pmean_Lmean_Thin_SI	32.3	0.549	0.863	0.755	0.890	0.836	0.692
	Pmean_Lmean_Heavy	16.6	0.388	0.683	0.426	0.875	0.662	0.525
	Pmean_Lmean_SISStiff	13.4	0.402	0.504	0.406	0.881	0.597	0.500
	Pmean_Lmean_SILoose	33.9	0.454	0.894	0.598	0.877	0.790	0.622
	GHBMC	36.1	0.472	0.730	0.336	0.851	0.539	0.505

## 9.7 VIP Model Force and Moment Plots

